UNIVERSITA' DEGLI STUDI DI ROMA
"LA SAPIENZA"

FACOLTA' DI SCIENZE MATEMATICHE
FISICHE E NATURALI

Ph.D. Thesis in Chemical Sciences

INORGANIC NANOSTRUCTURED MATERIALS FOR TECHNOLOGICAL APPLICATIONS

Supervisor

Prof. Daniele Gozzi

Candidate

Alessandro Latini

ACADEMIC YEAR
2004-2005

INDEX

Page

Page

1. Introduction

1.1 General overview

In the field of materials science, the topic concerning nanostructured materials is today of great interest; these materials have unique physical and chemical properties, often very different from those of their bulk counterparts, thus opening new perspectives for the modern technology. Nanomaterials are materials the dimensions of which are in the range from 0.1 nm to 100 nm. The production and processing of structures and particles at the nanometer scale allows for the manipulation of the matter at atomic scale. The purpose is to obtain of extremely small devices or structures with tailored properties. Nanotechnology is based on the production and utilization of functional materials, devices and systems with novel functions and properties that are based either on their geometrical size and/or material-specific peculiarities of the nanostructures. The nanometric scale manipulation and control in materials science has been achieved only in recent years, but the methods of production of some nanoscale materials is known by centuries. One famous example is the pigment known as Purple of Cassius (named after Andreas Cassius, a dutch chemist who published in 1685 the recipe for making this pigment), which is a suspension of nanoparticles of gold made by reduction by tin of a solution of gold in aqua regia. Gold is a good example to show the great changes that occur in the physico-chemical properties moving from the macro- to the nano-scale. As the name suggests, the Purple of Cassius is a red pigment whereas bulk gold is yellow: the electronic properties have been changed. The melting point of gold at nanometric scale is substantially lower than that of bulk gold [1] (fig. 1) ; nanometric gold is an active catalyst in the selective oxidation of CO in presence of H_2 even at –70 °C [2], while bulk gold is substantially inactive.

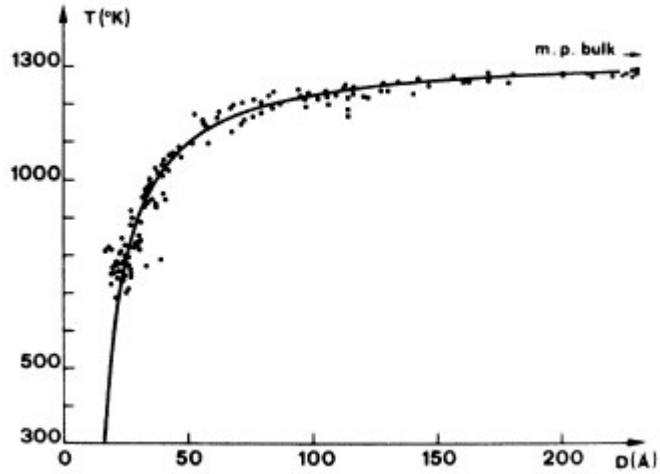

Fig. 1

1.2 Aim of this work

This work can be divided into two major topics: i. the simultaneous production of carbon nanotubes (CNTs) and hydrogen by catalytic decomposition of methane and ii. the growth and characterization of ceramic cathodoluminescent thin films prepared by electron beam physical vapour deposition. These topics, apparently not correlated, have one very important common point: both the carbon nanotubes and cathodoluminescent thin films are materials of great increasing interest for the optoelectronics and, in particular, in the development and realization of the field emission displays (FED). They will be discussed in par. 1.5.

1.3 Catalytic decomposition of methane as a source of H_2 and CNTs

In recent years the interest about hydrogen as an eco-compatible fuel has grown dramatically, largely because of the greenhouse effect caused by fossil fuels. Today's common large scale production processes have anyway high costs and produce high quantities of CO_2, thus not resolving the problem of greenhouse gases emissions in the atmosphere.

The most common reactions are:

1. methane steam reforming at 1100 °C:

$$CH_4\ (g) + H_2O\ (g) = CO\ (g) + 3H_2(g)\ \Delta G^0_{1373K} = -121.5\ kJ/mol$$

followed by the catalytic water gas shift at 400 °C on cobalt or iron catalysts:

$$CO\ (s) + H_2O\ (g) = CO_2\ (g) + H_2(g)\ \Delta G^0_{673K} = -14.0\ kJ/mol$$

2. methane dry cracking:

$$CH_4\ (g) + \tfrac{1}{2}O_2\ (g) = CO\ (g) + 2\ H_2\ (g)\ \Delta G^0_{1273K} = -273.5\ kJ/mol$$

3. coke shift at 1000 °C:

$$C\ (s) + H_2O\ (g) = CO\ (g) + H_2(g)\ \Delta G^0_{1273K} = -46.9\ kJ/mol$$

All these processes, with the exception of water gas shift, require always high temperatures, pressures and all produce large amounts of CO_2 (through the methane steam reforming, the most diffuse process, 50 Mt/year of H_2 are produced, that implies the production of 275 Mt/year of CO_2). So, from an environment protection point of view, for an hydrogen based economy the reactions above cannot be considered, though some researchers propose the sequestration of CO_2 in appropriate geological sites [3]. Another consideration should be done: the massive use of hydrogen as fuel implies also a diffuse utilization of fuel cells for an efficient production of electricity. The most common used fuel cells are those based on polymeric electrolyte membrane (PEM-FC), whose anode catalyst (Pt or Pt/Ru) is easily of poisonable by CO, the concentration of which must be kept below 10 ppm. This implies a further step of purification in the whole production of H_2 by the methods previously described. In a long term perspective, the development of water

photodissociation catalysts, electrocatalysts to lower hydrogen discharge overvoltage in water electrolysis, and water splitting by thermochemical cycles seem the most promising processes, though, until now they seem far to be applicable. In a medium term perspective, catalytic decomposition of hydrocarbons to carbon and hydrogen seems more realistic. Having a look to the standard free energies of formation of the three lightest saturated hydrocarbons at 25 °C and to the inversion temperatures of their standard free energies of formation (tab. 1), we can see that they may be decomposed at relatively moderate temperatures.

	CH_4	C_2H_6	C_3H_8
ΔG^0_f (298K) kJ/mol	-50.5	-32.0	-23.5
T inv ΔG^0_f °C	546	197	110

Tab. 1

Until now these reactions did not gain an adequate consideration for producing H_2. The reason is quite evident: all these reactions require to be catalysed and the carbon poisoning of the catalyst surfaces is a well known problem in heterogeneous catalysis. In fact, coke rapidly covers the active sites, thus deactivating the catalysts, unless carbon is continuously removed from the surface of the catalyst. This is what happens when hydrocarbons are decomposed forming CNTs and H_2: carbon formed at the catalytic site diffuses towards the growing CNT thus leaving the active site. This aspect will be considered in detail in Chapter 3.

1.4 Carbon nanotubes: an overview

Since the publication of the paper of Sumio Iijima [4] of NEC Corporation, the interest on carbon nanotubes has dramatically grown up. Iijima is now claimed as the discoverer of CNTs, but I prefer to say that he was the first to clarify the structure of this form of carbon and to adopt the term "nanotube". But this form of carbon is known since the mid of the XX^{th} century. The first report of CNTs, entitled as "An unusual form of carbon" was reported by Davis ad co-workers [5] of the British Ceramic Research Association in 1953, by studying the disintegration of furnace bricks operated by the formation of carbon during the high temperature interaction with CO. They found that carbon was formed by the reaction:

$$2\ CO\ (g) = CO_2\ (g) + C\ (s)$$

catalysed by the iron impurities in the bricks. (The iron-catalysed disproportionation of CO is today commonly used for CNTs synthesis [6]). They called these structures “vermicules”. Anyway, the work of Iijima was really important to understand better this particular and technologically promising form of carbon. CNTs can be roughly divided into two types: single walled (SWCNT) and multi-walled (MWCNT). Many synthetic paths have been developed for their production: arc discharge or laser assisted vaporization of graphite [4][7], and many catalytic processes differing in the catalyst type or in the carbon precursor or in both ones [8][9]. Frequently the catalyst contains Fe, Co, or Ni, supported or not, alone or in combination with other metals. Rather surprisingly, the use of precious metal-based catalysts is not common. Now, let’s have a detailed look to CNTs structure. A SWCNT can be seen as a rolled graphene sheet:

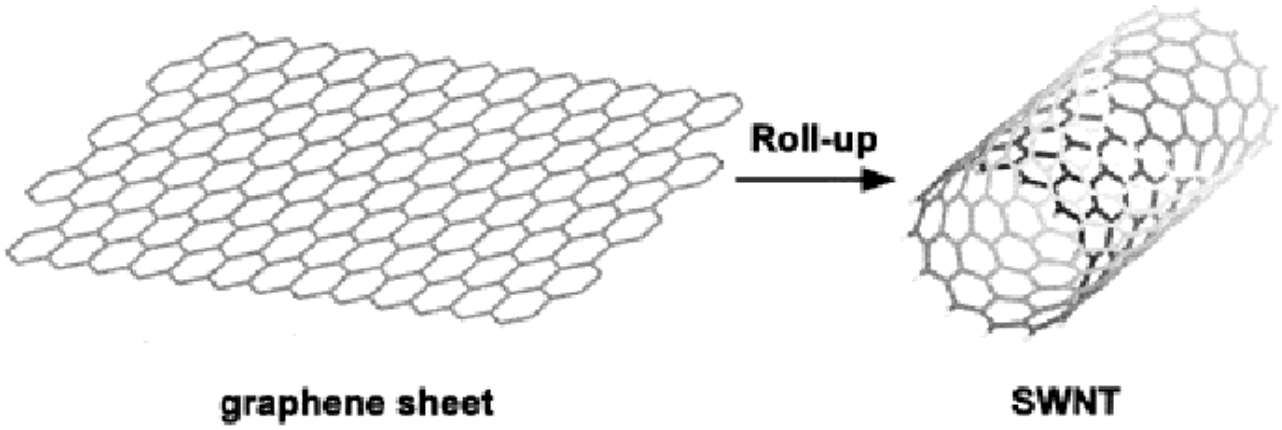

Fig. 2

while MWCNT can be represented as an array of coaxial SWCNTs:

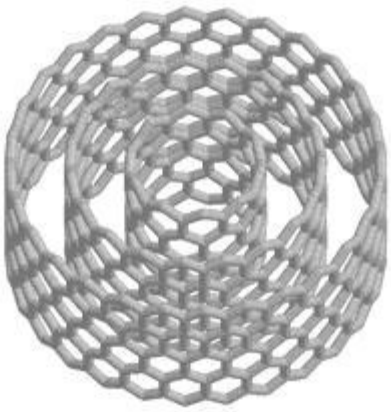

Fig. 3

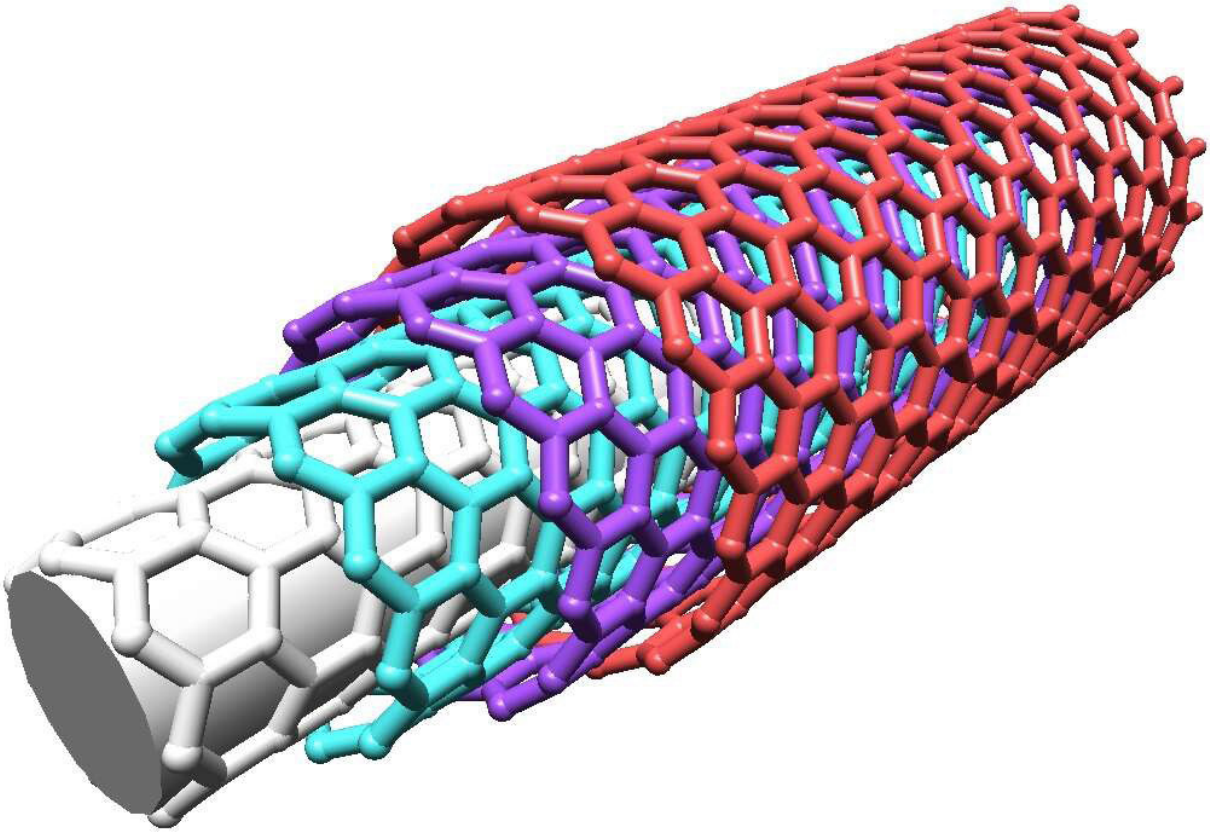

Fig. 4

Because they have one or more rolled graphene sheets, obviously CNTs have carbon atoms bonded via sp^2 σ bonds, with a delocalised π bond. Each rolled graphene sheet may be closed at one or both ends with a fullerene cap.

A SWCNT is described [10] by its diameter d_t and its chiral angle θ ($0 \leq |\theta| < 30°$). $\boldsymbol{C_h}$ is the chiral vector defined by two integers m and n and the basis vectors of the graphene sheet:

$$\boldsymbol{C_h} = n\mathrm{a}_1 + m\mathrm{a}_2 \equiv (m, n) \qquad (1.4.1)$$

θ is the angle between $\boldsymbol{C_h}$ and the zig-zag direction (n, 0). The numbers (m, n) determinate d_t and θ by the relations:

$$d_t = \frac{1}{\pi} a\sqrt{n^2 + m^2 + mn} \qquad (1.4.2)$$

$$\sin\theta = \frac{\sqrt{3}m}{2\sqrt{n^2 + m^2 + mn}} \qquad (1.4.3)$$

If the SWCNT is rolled in the $\boldsymbol{C_h}$ direction**,** we have a (*m*, *n*) SWCNT. When *m*=*n*, we have a "armchair" SWCNT, whereas when *m*=0, the SWCNT is called "zig-zag". In the other cases. i.e. $n \neq m$ and $m \neq 0$, the SWCNT is chiral.

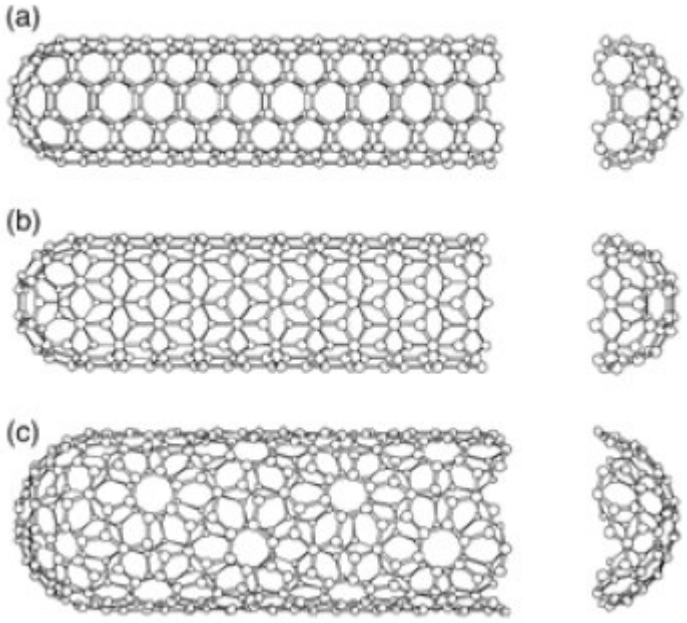

Fig. 5

The translation vector $\boldsymbol{T}$ is defined as:

$$T = t_1 a_1 + t_2 a_2 \qquad (1.4.4)$$

where:

$$t_1 = \frac{2m+n}{d_r};\ t_2 = -\frac{2n+m}{d_r} \qquad (1.4.5)$$

with d_r the biggest common divider of $(2m+n, 2n+m)$.

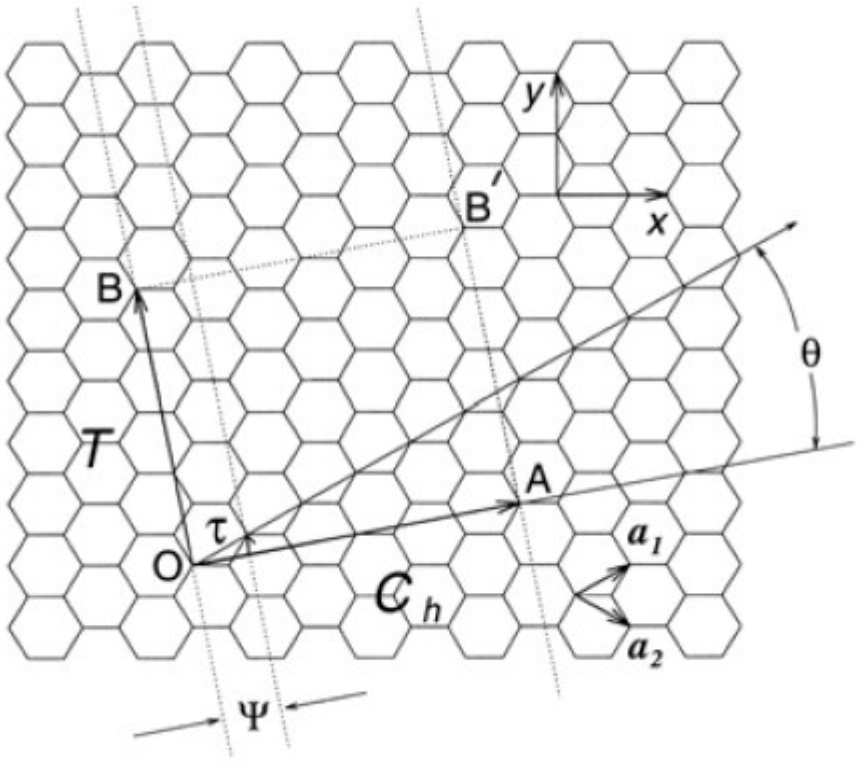

Fig. 6

The unit cell of a SWCNT that can be translated in only one direction is defined by the rectangle formed by the vectors $\boldsymbol{T}$ and $\boldsymbol{C_h}$. The structure of a chiral SWCNT affects its electrical conductivity. A chiral SWCNT shows metallic conductivity only if $(n\text{-}m)/3$ is integer: otherwise, it behaves as a semiconductor. Tab. 2 contains a list of geometric parameters of SWCNT. Considering now MWCNTs, every wall can be treated as a SWCNT. A MWCNT cannot have the AB stacking of graphite because of the different radius of curvature of each wall. Anyway, the walls show some degree of correlation: TEM analysis [11] show an interlayer distance of 3.4 Å, a value between common graphite (3.354 Å) and turbostratic graphite (3.44 Å). So, MWCNTs can be considered as partly turbostratic.

1.5 Applications of CNTs

Up to now, there are not market scale applications of CNTs, but these are potentially enormous. Many studies are carried out to employ these materials in electronic devices, especially for their potential in future nanoelectronic devices. CNT-based field effect transistors have been already built [12], but as written in the last paragraph, CNTs can be metallic or semiconducting: for applications in integrated electronics, it is of primary importance to obtain only one type of CNTs, but usually the synthesis gives a mix of the two types. But recently Krupke and co-workers [13] have developed a method of separation of metallic and semiconducting CNTs. One of the most promising application of CNTs is their use as efficient nanometric field emitters [14]. This is useful for the realization of miniaturized X-rays sources [15] and for FEDs [16][17], either by directly growing CNTs on the anode or by using the more economic screen printing technique [18]. Some SEM images of CNT-based field emitters for FEDs are given in figg. 7-9.

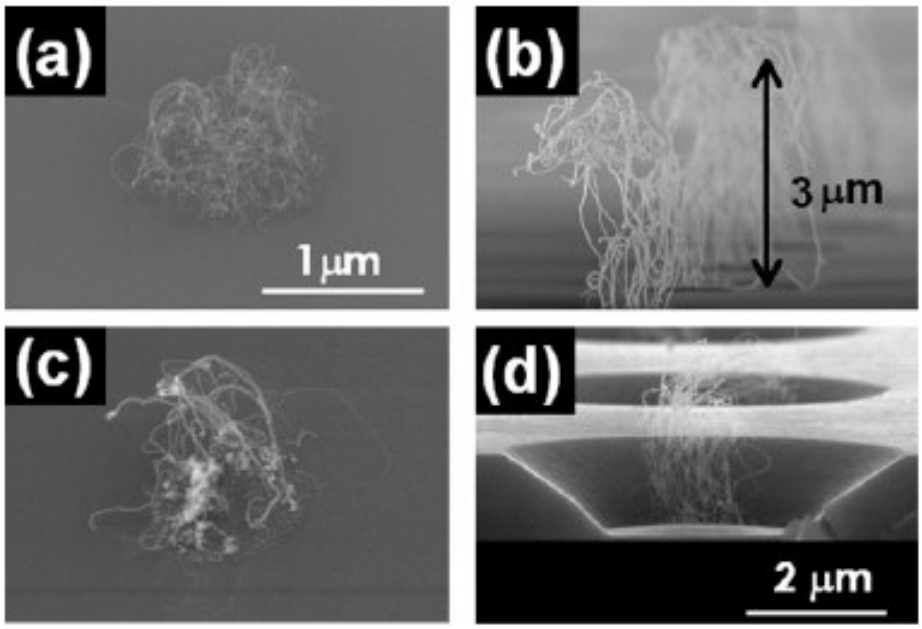

Fig. 7

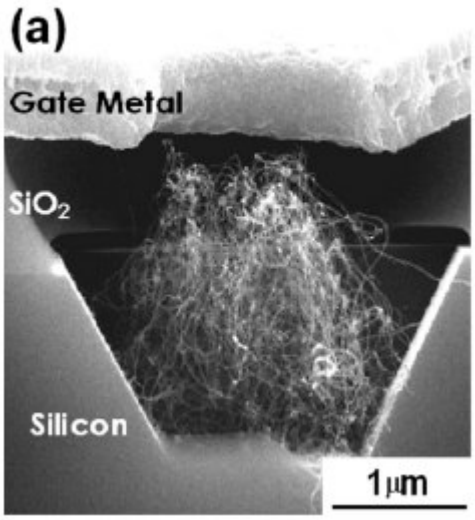

Fig. 8

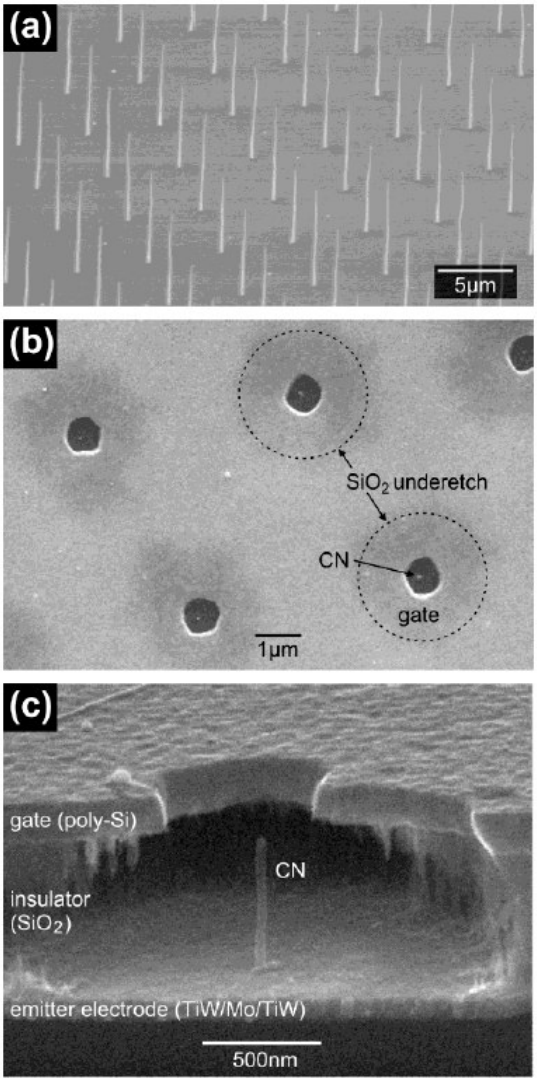

Fig. 9

Interesting results were obtained by Lopez Manchado in the utilization of CNT in polymer-based composites [19] and by Cantalini [20] for the use of CNT in gas-sensing applications. CNTs

supported catalysts [21][22] and electrocatalysts for fuel cells [23] also seem promising. Cai and co-workers are studying MWCNTs as solid phase extraction adsorbent [24].An extensive research activity with good results is the one dedicated to the realization of CNT-tips for AFM (fig. 10) and STM (fig. 11) microscopes[25][26].

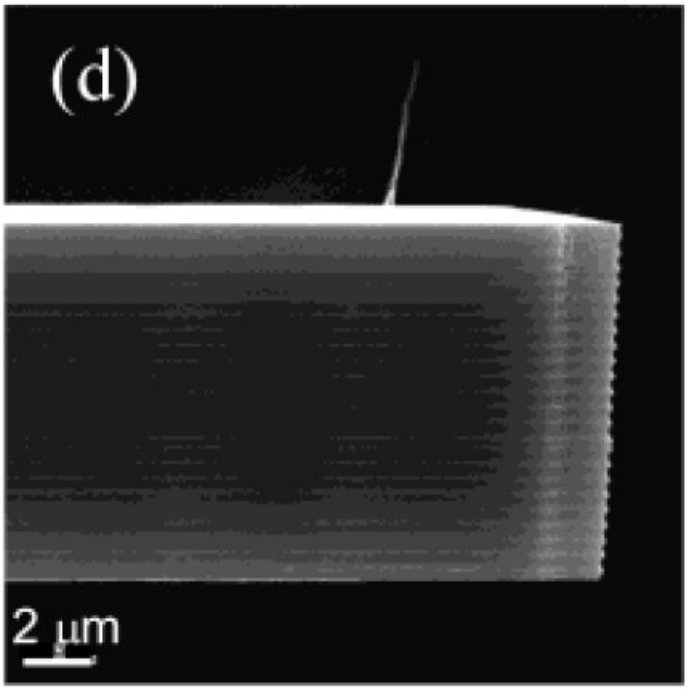

Fig. 10

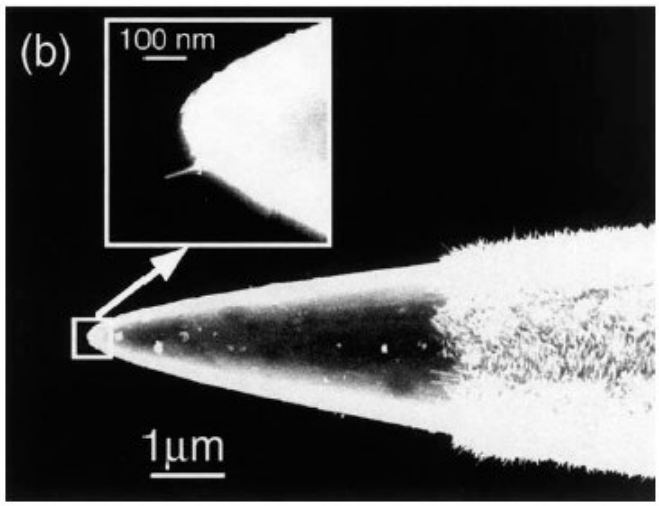

Fig. 11

The interest for the use of CNTs as an efficient and reversible hydrogen storage medium exploded in 1997 after the publication of the paper of Dillon [27] and especially after that of Chambers[28], who claimed an H_2 adsorption capacity in MWCNTs of over 67 wt.% (the required capacity by the U.S. Department of Energy for automotive applications is 6.5 wt.%). This interest has disappeared after the fact that nobody has been able to reproduce these results [29]. Nowadays only functionalised CNTs are studied for this purpose [30][31].

1.6 Field Emission Displays: an overview [32]

FEDs are vacuum fluorescent displays using field emitters as cathodes. Field emission is the phenomenon that occur when a surface of a metal or a semiconductor is subjected to an electric field as high as ~10^9 V/m: electrons are emitted as result of the tunnelling effect, and this happens also at room temperature. Field emission cathodes have been studied since 50 years to obtain cold and high brightness electron sources and now these sources are widely used in electron microscopes, high brightness X-ray sources, etc. The same techniques utilized for the semiconductor fabrication processes have been adopted for the miniaturization of the emitters for field emission cathodes, as those needed for FEDs. FED technology is one of the most promising for the next generation displays. They are based on the cathodoluminescence as the CRT displays, but FEDs combine the compact structure of LCDs and plasma displays with the expected result of an image quality equal or better than CRTs. But FEDs' manufacture requires to overcome some technologically important problems. The first problem regards the realization of an array of efficient microscopic field emitters. Older methods make use of anisotropic etching and thermal oxidation of Si substrates or microtip deposition on glass substrates by sputtering or evaporation coupled with etching processes. These techniques lead to many problems, such as short device lifetime and complicated fabrication processes. Recent progresses seem to be achieved by the use of CNT-based emitters obtained either by direct growth on the substrates [16, 17] or by more simple screen printing techniques followed by appropriate treatments to improve the emission efficiency [18]. CNT-based FED emitters have been shown in the previous paragraph; In figg. 12-16 a conventional FED emitter, FED structure (2 figs.), conventional FED prototypes and a CNT-based FED prototype, respectively, are shown.

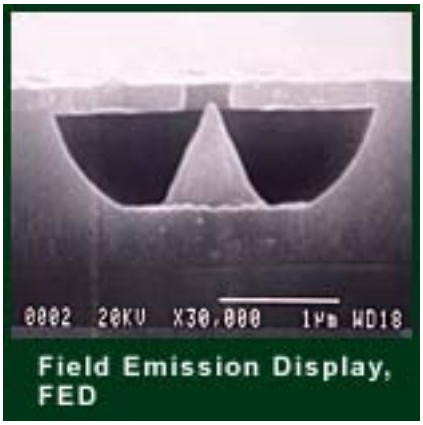

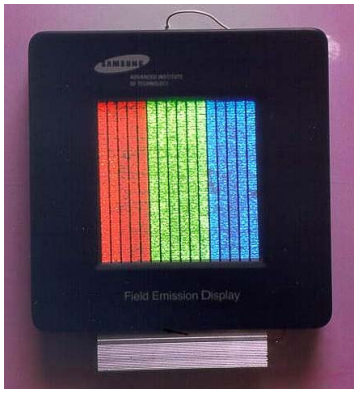

Figg. 12-16

FED anodes are usually made of indium-tin oxide (ITO) conductive glass plates coated with phosphors. The anode must be kept at a certain distance (~1 mm) from the cathode and the separation may be realized by glass spacers; the unit must be evacuated to a pressure $<10^{-7}$ mbar and sealed. Obviously, even weak degassing processes may result in a high increase in the pressure inside the device, considering the small volume. By applying a voltage of 100 to several kV between the anode and the cathode, electrons are field emitted and bombard the phosphors producing luminescence. Color selectivity in full-color FEDs can be achieved by the dot control on the anode.

1.7 Phosphors for FEDs

Though they work on the same principle, phosphors used in CRT displays do not seem to be suitable for FEDs. Common RGB phosphors for CRTs are Y_2O_2S: Eu^{3+} (red), ZnS: Ag^{+} (blue) and ZnS: Cu^{2+} (green), undergo to a rapid degradation under the high electron density excitation present in FEDs, creating a dead layer on the anode and contaminating the cathode [32]. Another problem arises from the common phosphor deposition techniques, which make use of aqueous slurries and organic binders such as polyvinyl alcohol, possible sources of outgassing [33]. The simplest way to overcome these problems is the use of ceramic phosphor thin films. Thin films show better adhesion and reduced outgassing in comparison to powdered phosphors; ceramic materials show high thermodynamic stability, refractoriness, very low vapour pressure, low thermal expansion coefficient, thus avoiding decomposition on the anode and contamination of the cathode. Rare earth doped oxide-based phosphors are extensively studied for this purpose because they have all the characteristics required, particularly yttrium oxide, zirconium oxide and gadolinium oxide [34][35][33]. In tab. 3 a comparison of thermochemical properties between these oxides and zinc sulphide are given.

Formula	ΔG^0_f(298K)/kJmol^{-1} O_2-S	Vapour pressure at 298K/Pa
Y_2O_3	-1210.9	-
Gd_2O_3	-1168.4	-
ZrO_2	-1042.5	10^{-121}
ZnS	-196.0	10^{-53}

Tab. 3

Obviously, there are other problems to consider. For example, the luminance of a thin film phosphor cannot be compared with the powdered counterpart because of the small quantity of material in a thin film: so it is necessary also to have an intrinsically highly efficient phosphor. In the next paragraph we will have a look to some concepts of the spectroscopy and luminescence of rare earth ions in order to learn how to optimise the host-dopant couples in the development of an efficient phosphor.

1.8 Spectroscopy and luminescence of rare earth ions [32]

The rare earth elements is the group of elements that goes from La to Lu (some classifications include also Sc and Y in this group). Along this group there is the progressive filling of the 4*f* orbitals. La^{3+} and Lu^{3+} have, respectively, empty and completely filled 4*f* orbitals, thus they do not have electronic levels leading to luminescent transitions in the visible region or near it. On the contrary, the ions from Ce^{3+} to Yb^{3+} have each one characteristic energy levels that can give a variety of luminescent processes in or near the visible region. Many of these ions can partially substitute non luminescent ions such as Y^{3+}, La^{3+}, Gd^{3+} (which does not have transitions in the visible region) or Lu^{3+} in various crystals giving phosphors. 4*f* orbitals have the angular number *l* equal to 3, thus (2*l*+1)=7 orbitals. Each orbital, according to Pauli's exclusion principle, can accommodate a maximum of 2 electrons, and, moving across the lanthanide series, the 4*f* orbitals are obviously filled in order to obtain the highest multiplicity in the ground state, i.e. the highest value of the total spin number *S*. The total angular number *J* is given by the relations:

$J=L-S$ when the number of the electrons in 4*f* orbitals is less than 7;

$J=L+S$ when the number of the electrons in 4*f* orbitals is larger than 7.

Each electronic state is denoted by the symbol $^{2S+1}L_J$; *L* is represented by the letters *S, P, D, F, G, H, I,* …, which stand, respectively, for the values 0, 1, 2, 3, 4, 5, 6,…. The spin-orbit interactions are quite low for the ground states and the levels near them, but become appreciable for excited states having neighbouring states with similar *J* values. The mixing of states due to spin orbit interaction does not affect the energy levels, but it does affect the optical transition probabilities.

The 4*f* levels are obviously characteristic for each lanthanide ion. Being *4f* orbitals very internal, they are effectively shielded by 5*s* and 5*p* electrons and so the energy levels arising by 4*f* electrons are little affected by the crystal field around the ion. Dieke studied extensively the energy levels of rare earth ions; his results are summarized in a diagram known as Dieke diagram (fig. 17), that refers to rare earth ions in $LaCl_3$ crystals; anyway, considering the small effect of the crystal field on the energy levels arising from 4*f* electrons, this diagram can be applied practically to any host containing rare earth ions with shifts at most of some cm^{-1}. Each level in the Dieke diagram is split into a certain number of sublevels due to the Stark effect caused by the crystal field. The maximum number of sublevels is $2J+1$ when J is integer, and $J+1/2$ when J is half-integer. The crystal field symmetry around the luminescent ion determinates the number of sublevels. Having a look to Dieke diagram, one can see that the light emitting levels are indicated by semicircles, while the width of level lines indicates the splitting range, and the emitting levels are separated from the nearest lower level at least by 2000 cm^{-1}. This because the excited states may relax by two competitive paths, one radiative and one non-radiative (phononic). The phonon emission rate is given by the formula:

$$w \propto e^{-\left(\frac{k\Delta E}{h\nu_{\max}}\right)} \qquad (1.8.1)$$

where w is the rate of phonon emission, k a constant, ΔE is the energy gap between the excited state and the nearest lower state and hv_{max} the maximum phonon energy of the host. So an increase in ΔE, as well as a decrease in hv_{max} are important to improve the luminous efficiency. The 4*f*-4*f* transitions originate mostly from electric dipole or magnetic dipole interactions. The electric dipole transitions are parity forbidden for the free ions and become partly allowed when the ions are in a crystal site without an inversion centre, while magnetic dipole transitions are parity allowed. For electric dipole transitions, the selection rule is $|\Delta J|\leq 6$; for magnetic dipole transitions, the rule is $\Delta J=0, \pm 1$ (but the transition $0\rightarrow 0$ is not allowed). Electric dipole transitions probabilities are treated by using the classic Judd-Oleft theory [36][37]. By integrating the experimental absorption coefficient $k(\lambda)=ln(I/I_0)/a$ (where I is the intensity of the transmitted light, I_0 the intensity of the incident light and a the sample thickness), we can obtain the line strength S which is equal to:

$$S = \int k(\lambda) d\lambda = \frac{8\pi^3 e^2 \lambda \rho}{3ch(2J+1)} \cdot \frac{1}{n} \cdot \frac{(n^2+2)^2}{9} \cdot s \qquad (1.8.2)$$

ρ is the density of the rare earth ion and n the refractive index. S contains the parameters Ω_2, Ω_4 and Ω_6 that give the light emission probability. They can be determined by a least square fit of s:

$$s = \sum_{t=2,4,6} \Omega_t \left| \langle (S,L)J \| U^t \| (S'L')J' \rangle \right|^2 \qquad (1.8.3)$$

where $\langle (S,L)J \| U^t \| (S',L')J' \rangle$ are reduced matrix elements characteristic of each ion: these values are available as a table. Ω_2, Ω_4 and Ω_6 are host-specific. The emission probability A and the line strength S' are respectively given by:

$$A = \frac{64\pi^4 e^2}{3h(2J'+1)\lambda^3} \cdot n \cdot \frac{\left(n^2+2\right)^2}{9} \cdot s' \qquad (1.8.4)$$

$$S' = \Omega_2 \left[U^{(2)}\right]^2 + \Omega_4 \left[U^{(4)}\right]^2 + \Omega_6 \left[U^{(6)}\right]^2 \qquad (1.8.5)$$

Due to their forbidden nature, 4*f*-4*f* transition have quite long lifetimes, in the range of ms, though when the transition has $\Delta S=0$ his lifetime is in the range of tens of μs. The concentration of luminescent ion in the host material is very critical for luminescence efficiency, and this is due to energy transfer processes. The energy stored in an excited ion can be transferred to another ion of the same species if they are sufficiently near, thus leading to a resonant energy transfer; so this mechanism and luminescence can become competitive. This competition becomes important when similar ions are separated by a distance of several Å, and when energy transfer becomes important concentration quenching appears. During the energy transfer process, the energy may be trapped at defects or impurity sites, thus enhancing non-radiative relaxation. Optimum concentrations vary depending on the ion and the hosts. On the other hand, energy transfer processes between different ions may be used to enhance luminescence. For example, the strong UV emission of Gd^{3+}, due to

the transition $^6P_{7/2} \rightarrow {}^8S$ (~315 nm), can be used to sensitise other ions. To obtain RGB phosphors, the choices are:

Eu^{3+} for red;

Tb^{3+} or Er^{3+} for green;

Tm^{3+} for blue.

In the red zone of the visible spectrum, Eu^{3+} has two transitions: around 600 nm, the magnetic dipole transition $^5D_0 \rightarrow {}^7F_1$ (site symmetry insensitive) and around 620 nm the electric dipole transition $^5D_0 \rightarrow {}^7F_2$ (site symmetry sensitive); the last transition becomes very intense when the Eu^{3+} ion is in a crystal site which lacks an inversion centre. Eu^{3+} luminescent transitions from the $^5D_0$ site are very efficient because the large energy gap with the nearest lower state (see Dieke diagram); for this same reason, the best choice for green is Tb^{3+} because his $^5D_4$ emitting state is more than $1.4 \cdot 10^4$ cm^{-1} separated from the nearest lower state. His emission in the green region (~550 nm), due to the transition $^5D_4 \rightarrow {}^7F_5$, is always the strongest among his luminous transitions, independently from the host. For the blue, the emission of Tm^{3+} ($^1G_4 \rightarrow {}^3H_6$, ~450 nm) is not as intense as for Eu^{3+} and Tb^{3+}, and this for two main reasons: the separation between the $^1G_4$ state and its nearest lower state is not as large as for Eu^{3+} and Tb^{3+}, and there is a competitive and highly efficient infrared luminescence.

1.9 Logical development of the work

1.9.1. Methane decomposition to H_2 and CNTs

The logical steps for this topic were:

-thermodynamic analysis of CH_4 decomposition;

-synthesis and characterization of the catalyst;

-development of the reactor;

-characterization of the carbonaceous residues and of the catalyst after the activity tests;

-hypotheses of reaction mechanism by the analysis of the experimental data;

-experimental verification of the mechanistic hypothesis;

-catalytic activity tests under the same CH_4 flow at different temperatures;

-development of a mechanistic model and its phenomenological and physical development.

1.9.2. Cathodoluminescent thin film growth

In this case, the logical steps were:

-choice of the rare earth luminescent ions by considering their spectroscopic properties (see 1.8);

-choice of the oxide hosts by examining their structural, thermodynamic and phononic properties;

-development and optimisation of the film deposition technique;

-deposition of films with different host to dopant ratio;

-structural, morphological and spectroscopic characterization of the samples obtain in order to establish the best candidates for FED application.

2. Experimental

2.1 CNTs growth, characterization and H_2 production

2.1.1 Reactor, growth conditions and H_2 production

The reactor used for the catalytic activity tests (fig. 18) consists of a ½" stainless steel tube (AISI 316) connected to a gas inlet system by Swagelok© tubing and closed at the bottom end by a stainless steel frit (VICI Jour) with a porosity of 2 µm. A. The catalytic tests were performed by depositing a powder layer of the catalyst over the frit. The reactor was placed in a vertical quartz tube furnace heated by a molybdenum coil (protected by Ar/H_2 flow), that can reach 1000 °C.

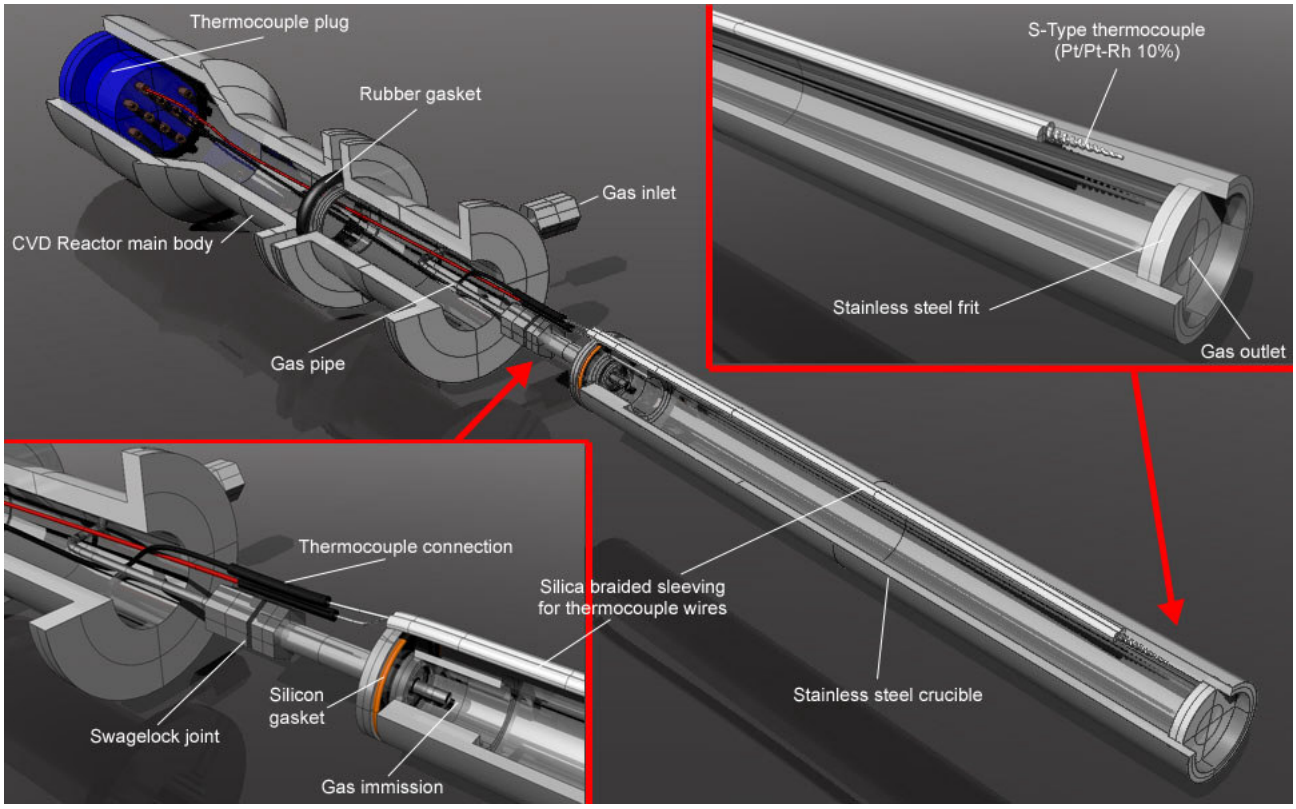

Fig. 18

The temperature of the reactor is monitored by a Type-S thermocouple (Pt/Pt-Rh 10 %). The flow of gas is controlled by two electronic mass flow controllers (one at the gas inlet; the other at the gas outlet is set full open just operating as a flow-rate meter). The furnace is sealed by Viton gaskets. All the experiments were performed by firstly heating the catalyst in a stream of Ar (purity…), then Ar was substituted by CH_4 (purity of 96.5%, with 3.5% H_2 as impurity), at a flow-rate of 5 sccm (sccm: cm^3min^{-1} @ STP). The temperature range explored was from 475 and 625 °C with steps of 25 °C. The composition, and then the H_2 content, of the outlet gas is monitored by a Balzers© quadrupole mass spectrometer (QMS) model QMG 421 connected to the outlet gas line with a stainless steel capillary (1 m long, 150 µm inner diameter) and a dosing valve (Balzers© UDV 040). The pressure difference between the gas line and the inlet chamber of the QMS is fixed by

differential pumping in order to operate the gas mixture injection in viscous regime. Thus ensures the absence of mass selection. A schematic draw of the system is given in fig. 19.

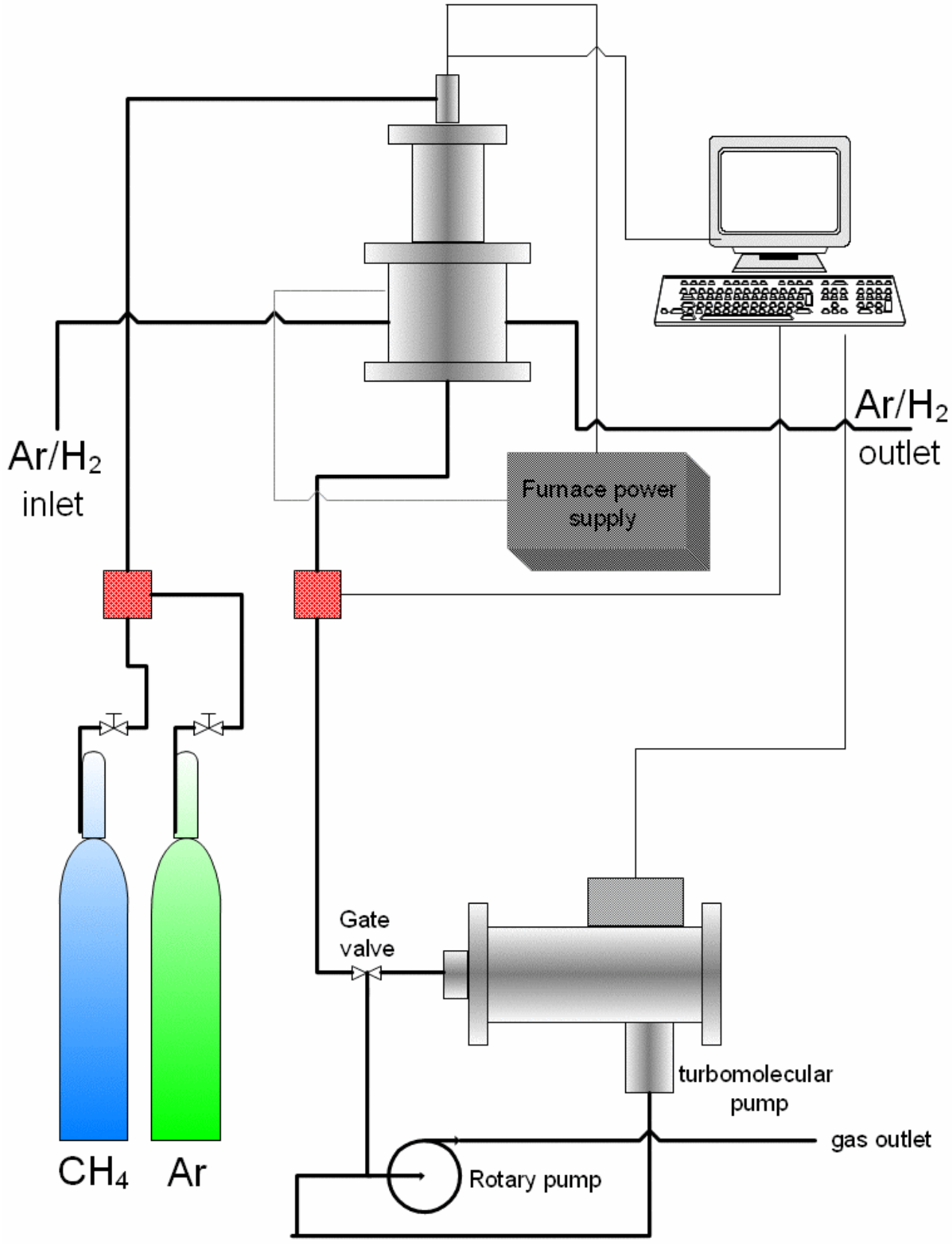

Fig. 19

The QMS is equipped with a quantitative analysis software that, after a proper calibration of the instrument, allows the real time concentration determination of the gaseous species present in the flowing mixture (MCD mode, i.e. Multiple Concentration Determination). After being sure of the absence of other gaseous species during the catalytic tests, the calibrations were made using a calibrated gas mixture containing Ar, CH_4 and H_2 in the respectively ratio 1:1:1. The concentration of these three gases was systematically monitored. After each experiment, the solid residue was removed from the reactor and, if the catalyst had to be removed, it was treated by hot 1:1 HCl under stirring for about 1 hour; then the CNTs were thoroughly washed with distilled water until to pH 7 in the washing liquid was reached. Finally, they were washed by acetone and dried in vacuum at room temperature.

2.1.2 Catalyst synthesis and characterization

Being the catalyst patent pending [38], its composition cannot be revealed. The synthesis was performed by electron beam melting of a pellet containing the appropriate quantities of the constituent elements, followed by X-rays powder diffraction (see par. *2.1.3*) to ensure the completeness of the reaction (fig. 20). Then the catalyst was ball milled overnight and then a second XRD analysis was performed (fig. 21). The catalyst was characterized by BET surface area measurement (Micromeritics ASAP) SEM, EDS and ICP analysis.

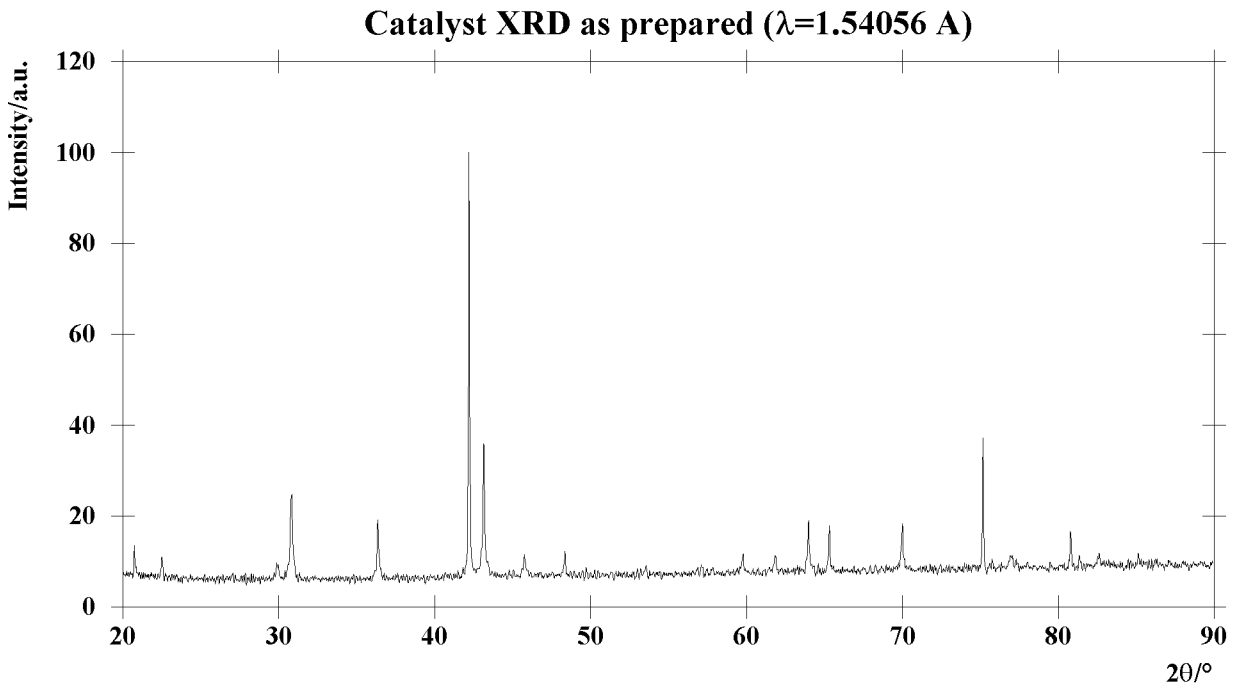

Fig. 20

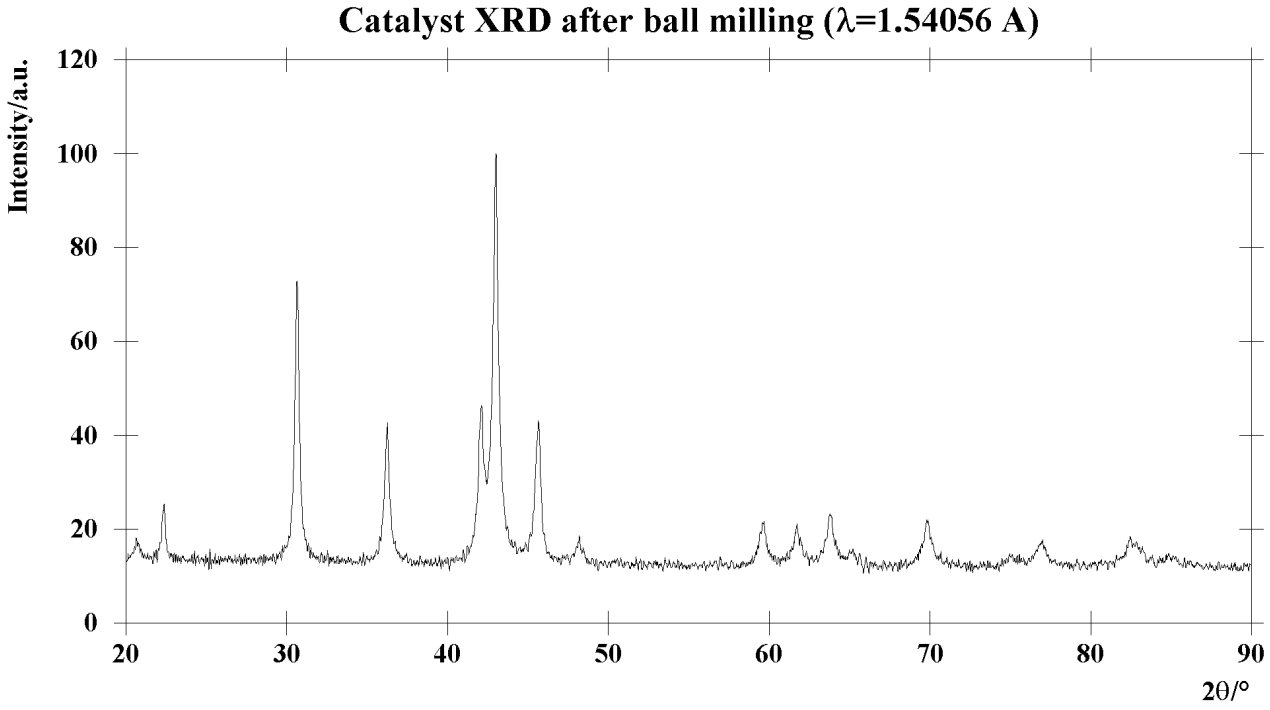

Fig. 21

2.1.3 CNTs characterization

CNTs, with or without catalyst, were characterized by X-rays powder diffraction with a Philips X'Pert Pro diffractometer using Cu Kα radiation. The Kβ radiation was filtered by a Ni filter, while the spectra obtained were subtracted of the $K\alpha_2$ component by the bundled software. Also transmission electron microscopy (TEM JEOL JEM 2010, 200 kV maximum accelerating voltage, point resolution 0.23 nm, microscope HR-TEM JEOL 3000F, 300 kV, point resolution 0.17 nm) and scanning electron microscopy (microscope LEO 1450 VP) were used. Chemical analysis of the samples was performed with EDS (Oxford Instruments INCA 3000), combustion and ICP analysis.

2.2 Cathodoluminescent films growth and characterization

2.2.1 Film growth

The apparatus for film growth consists of water cooled stainless steel a vacuum chamber evacuated by a turbo pump (Pfeiffer vacuum model TMU 521) supported by a rough pump by Edwards, and equipped by two water cooled electron beam guns (model EV1-8, Ferrotec). The accelerating voltage can be set between 3.05 and 10 kV, while the emission current between 0.5 and 500 mA. The shape and position of the beam is controlled by two digital joypads, and the film growth rate and thickness is monitored by two quartz microbalances. A scheme of the apparatus is given in fig. 22. The substances to be evaporated were positioned into the pockets of the guns (1 pocket for each

gun) using crucibles made of a TiB_2/BN composite (GE advanced materials), a material possessing outstanding thermal shock resistance and chemical inertness at very high temperatures. All the materials to be evaporated (Y_2O_3, Gd_2O_3, Eu_2O_3, Tb_4O_7 and Tm_2O_3 powders), made by Aldrich (purity >99%), were cold pressed into pellets (18 mm diameter) before use. In all the deposition processes an accelerating voltage of 3.5 kV was used, while the emission current was varied during the processes in order to ensure a constant deposition rate. One gun was used for evaporating the host material, while the other for the dopant. Their respective deposition rates were fixed in each experiment in order to roughly establish the dopant concentration. The film growth rate was from 15 to 20 Å s^{-1} in all the deposition processes. The substrates (optically polished SiO_2 slides, 50x20x1 mm) were positioned perpendicular to the vapour cones emitted by the EB-guns and they were radiatively heated up to 800 °C during the deposition processes by a high power halogen lamp (Sylvania). Such a high temperature was used in order to enhance the surface mobility of the deposited species during the deposition, a better adhesion of the film and better uniformity of the deposit. The film thickness was for all samples of about 1 μm. Three samples with different host/dopant ratio were deposited for each host-dopant couple.

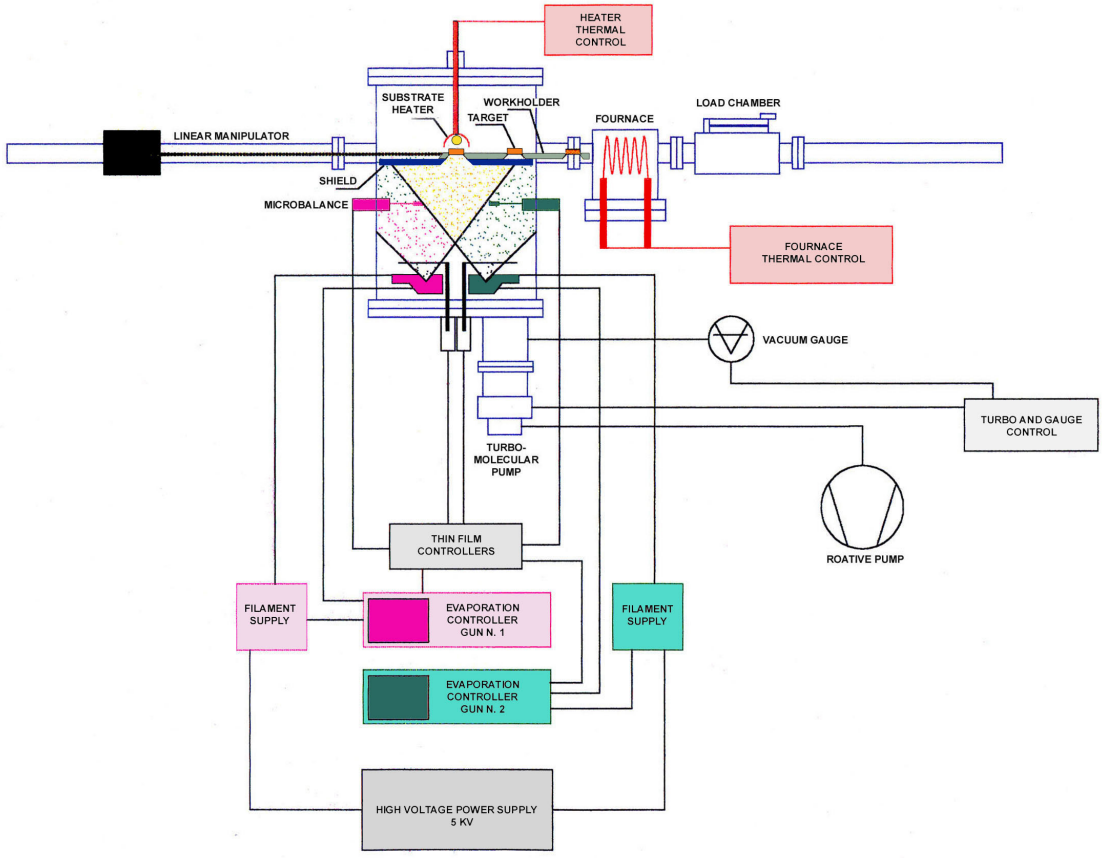

Fig. 22

2.2.2 Film characterization

All the films were characterized by thin film-XRD with the diffractometer Philips X'Pert Pro (see par. 2.1.3), that is equipped also by a thin film analysis apparatus. The measurements were performed using a fixed incident angle of 2° in order to ensure low X-ray penetration of the substrate, a 1/32° divergence slit and without the Ni filter. The scan step size was 0.02° (time per step 2.05 s). The $K\alpha_2$ and the Kβ components of the Cu radiation were cut by a graphite monochromator positioned just before the detector. The morphological characterization of the films was performed by SEM microscopy, and the chemical analysis by EDS spectroscopy (see par. 2.1.3). The EDS measurements on the samples were made in variable pressure condition (VP) because their insulator behaviour; the SEM images were taken after covering the samples with a thin layer of sputtered gold. The cathodoluminescence spectra were acquired by a Gatan MonoCL spectrophotometer attached to a Cambridge SEM microscope (measurement conditions: voltage 20 kV, emission current 3 nA, resolution 1 nm), after depositing on the films a 50 Å-thick layer of Au to make them conductive. The color co-ordinate measurements have been carried out at 8 kV and 1 μA and using a LMT colorimeter type C 2200. In this instrument, the functions $\bar{x}(\lambda)$, $\bar{y}(\lambda)$, $\bar{z}(\lambda)$ according to CIE 1931 are built by using light-sensitive detectors with optical filtering. Being a tristimulus colorimeter, it is possible to measure the tristimulus values *X*, *Y*, *Z* at a well-defined moment at the same time. The equations below define the above quantities:

$$X = K\int_{380}^{780} P(\lambda)\bar{x}(\lambda)d\lambda;\ Y = K\int_{380}^{780} P(\lambda)\bar{y}(\lambda)d\lambda;\ Z = K\int_{380}^{780} P(\lambda)\bar{z}(\lambda)d\lambda \qquad (2.2.2.1),$$

where, P(λ) is the spectral energy distribution of a test light source and $\bar{x}(\lambda)$, $\bar{y}(\lambda)$, $\bar{z}(\lambda)$ are the spectral stimulus values for a 2° solid angle in psychophysical experiments. λ stands for the wavelength. The color coordinates are given by:

$$x = \frac{X}{X+Y+Z};\ \mathrm{y} = \frac{\mathrm{Y}}{X+Y+Z} \qquad (2.2.2.2)$$

HR-TEM on one film was performed using a JEOL CX200 microscope.

3. Results and discussion

3.1 CNTs growth and H_2 production

3.1.1 Thermodynamics of CH_4 decomposition

As seen in par. 1.3, the ΔG^0_T of the reaction :

$$CH_4(g) \rightarrow C(s) + 2H_2(g)$$

becomes negative for T>546 °C, and so the reaction is thermodynamically favoured at high temperatures. The ΔH^0 is quite constant in the temperature range 500-1500 °C, varying from 86 to 90 kJ mol^{-1}, while the $T\Delta S^0$ contribution to the ΔG^0 varies much more, ranging from 81 to 193 kJ mol^{-1} in the same temperature range. The temperature dependence of ΔG^0 (negative) is so due practically only to the $T\Delta S^0$ term, and this is easy understandable, considering that 2 moles of gaseous product are obtained from 1 mole of gaseous reactant.

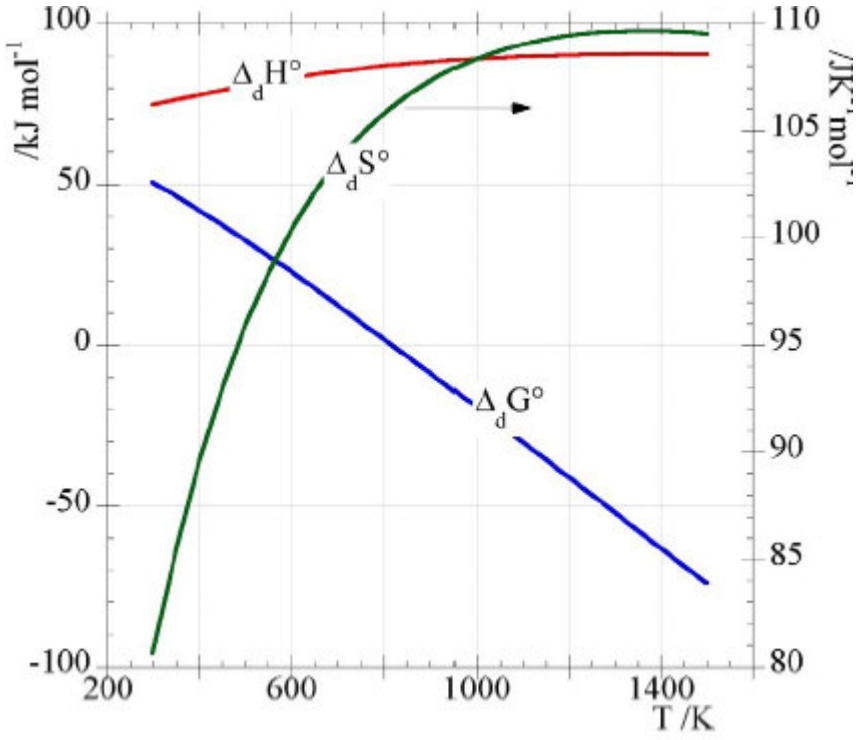

Fig. 23

For the CH_4 decomposition, the free energy variation is given by:

$$\Delta G = \Delta G^0 + RT \ln \frac{\left(\frac{x_{H2} p_{tot}}{p^0}\right)^2}{\left(\frac{x_{CH4} p_{tot}}{p^0}\right)} \qquad (3.1.1.1)$$

obviously considering a_C=1. The ΔG can be expressed also as a function of mole fractions:

$$\Delta G = \Delta G^0 + RT \ln \frac{p_{tot}}{p^o} + RT \ln \frac{x_{H2}^2}{x_{CH4}} \qquad (3.1.1.2)$$

In our reactor we can control the composition and the flow rate of the gas. So now, in order to write the ΔG expression as a function of gas composition and flow rate, considering the reaction:

$$\underset{n_{in}CH_4 - nH_2 + \frac{1}{2}n_{in}H_2}{CH_4}(g) \Leftrightarrow C(s) + \underset{n_{in}H_2 + 2nH_2}{2H_2}(g)$$

where:

$n_{in}CH_4$ is the number of inlet CH_4 moles;

$n_{in}H_2$ is the number of inlet H_2 moles;

nH_2 is half the number of produced H_2 moles;

and considering:

$n_{in}Ar$ the number of inlet Ar moles;

$n_{tot}=n_{in}CH_4+3/2n_{in}H_2+nH_2+n_{in}Ar$ the total moles number;

$n_{in}=n_{in}CH4+n_{in}H2+n_{in}Ar$ the number of inlet moles,

the half outlet moles of H_2 are $n_{out}H_2=1/2n_{in}H_2+nH_2$, thus giving $n_{tot}=n_{in}+n_{out}H_2$. By using these definitions, the ratio between $(x_{H2})^2$ and x_{CH4} becomes:

$$\frac{(x_{H2})^2}{x_{CH4}} = \frac{(n_{in}H_2 + 2nH_2)^2}{(n_{in}CH_4 + \frac{1}{2}n_{in}H_2 - nH_2)n_{tot}} = \frac{4(n_{out}H_2)^2}{(n_{in}CH_4 - n_{out}H_2 + n_{in}H_2)(n_{in} + n_{out}H_2)} \qquad (3.1.1.3)$$

the last formula is due to the relation: $2nH_2 = 2n_{out}H_2 - n_{in}H_2$.

If we consider the total inlet flow J_{in} and the outlet H_2 flow $J_{out}H_2$, defining $\gamma = \frac{J_{in}}{J_{out}H_2} = \frac{n_{in}}{n_{out}H_2}$

and $x^*=x_{CH4}+x_{H2}$, and substituting in (), we obtain:

$$\frac{(x_{H2})^2}{x_{CH4}} = \frac{4}{(\gamma+1)(x^*\gamma-1)} \qquad (3.1.1.4)$$

and then this expression in the ΔG expression:

$$\Delta G = \Delta G^0 + RT\ln\frac{p_{tot}}{p^0} + RT\ln\frac{4}{(\gamma+1)(x^*\gamma-1)} \qquad (3.1.1.5)$$

In the simplest case, when the inlet gas is only CH_4 ($x^*=x_{CH4}=1$), we have:

$$\Delta G = \Delta G^0 + RT\ln\frac{p_{tot}}{p^0} + RT\ln\frac{4}{\gamma^2-1} \qquad (3.1.1.6)$$

By using arbitrary J values compatible with our system, we are able to plot the ΔG trend and to extrapolate the inversion temperatures (figg. 24-25).

3.1.2 The initial experiments

The first stage of this work was mostly explorative as the behaviour of the catalyst towards CH_4 decomposition was unknown. Surprisingly, it showed a good activity at 500 °C and CH_4 flow rate of 5 sccm:

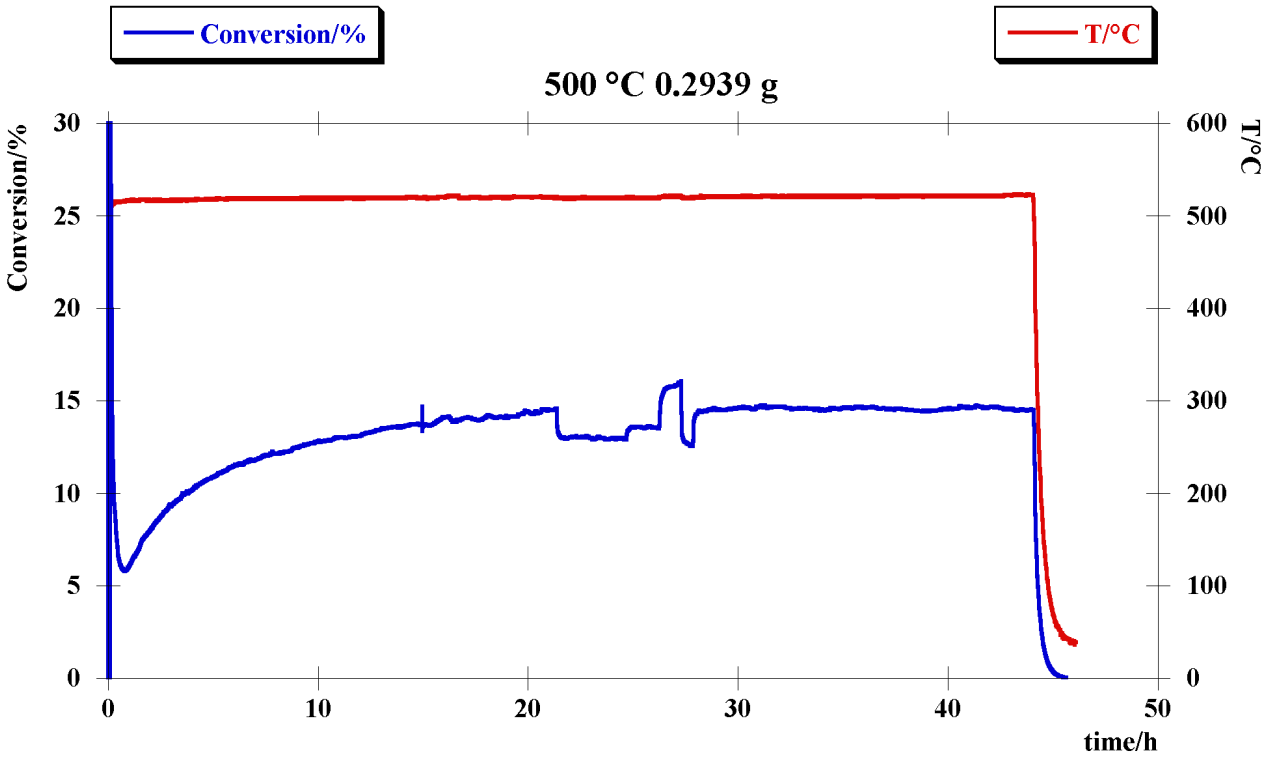

Fig. 26

The conversion is intended as :

$$\frac{CH_4^{\,0} - CH_4^{\,t}}{CH_4^{\,0}} \cdot 100 \qquad (3.1.2.1)$$

Where $CH_4^{\,0}$ is the methane concentration of the feeding gas and $CH_4^{\,t}$ is the methane concentration at the reactor outlet. The mass spectrum of the gas at outlet showed only the signal of CH_4 and its fragments and H_2. No hydrocarbon cracking products such as acetylene were observed. Being H_2 the only gaseous reaction product and considering the stoichiometry of the reaction:

$$CH_4(g) \rightarrow C(s) + 2H_2(g)$$

the conversion can be also calculated by the formula:

$$\frac{H_2^{\,t} - H_2^{\,0}}{2CH_4^{\,0}} \cdot 100 \qquad (3.1.2.2)$$

where $H_2^{\,t}$ is the hydrogen concentration at outlet and $H_2^{\,0}$ the hydrogen concentration of the feeding gas. The discontinuities in the conversion are due to flow rate changes; finally, the flow rate was set to the initial value. After the experiment, the catalyst was removed by chemical treatment and a carbon residue was recovered. SEM images (see figg. 27-28) of the carbon residue showed

agglomerates of CNTs without evidence of other forms of carbon (graphite and/or amorphous carbon):

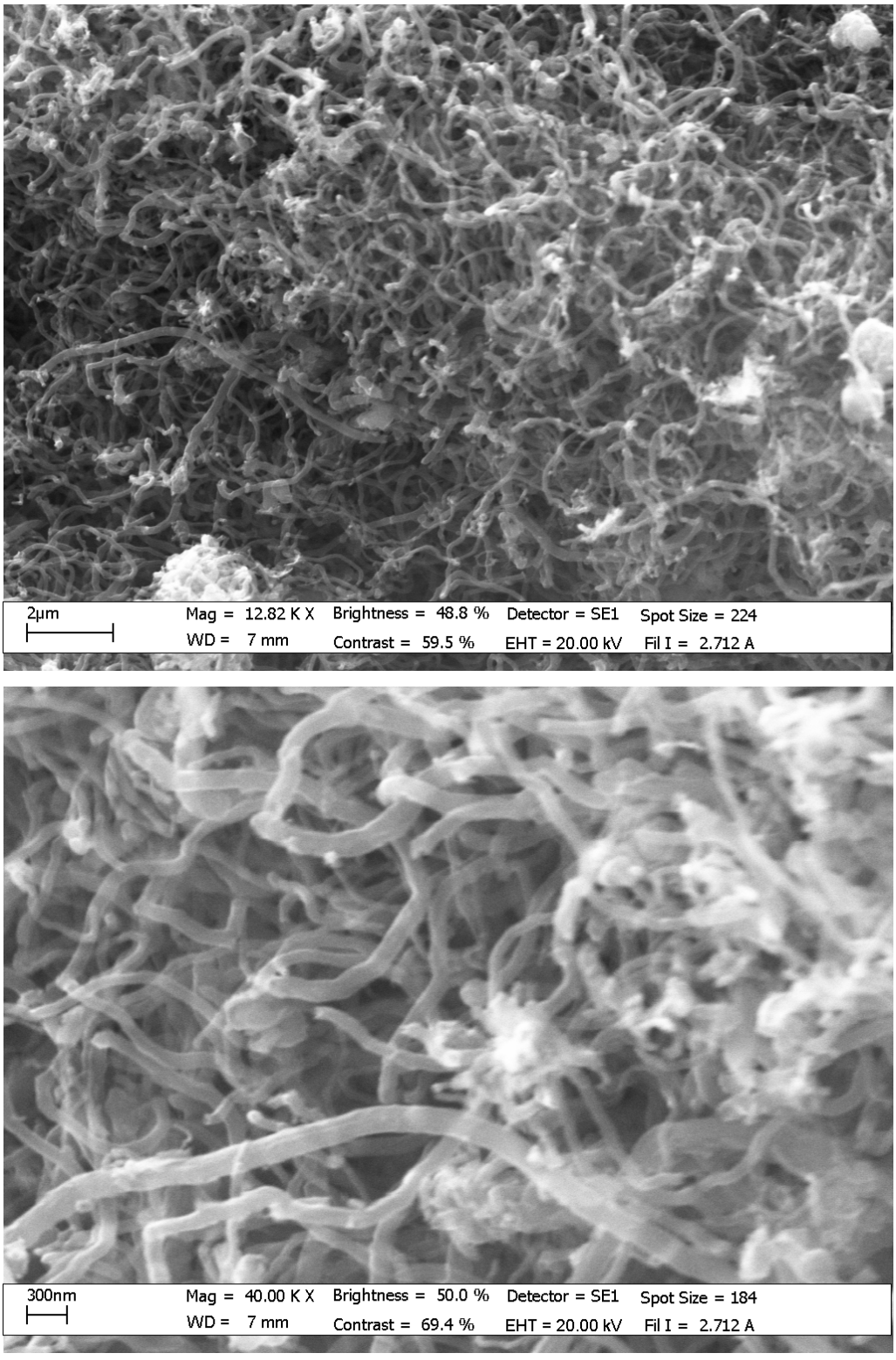

Figg. 27-28

A second experiment was performed in order to check the reproducibility of the reaction behaviour, and this experiment confirmed the first one:

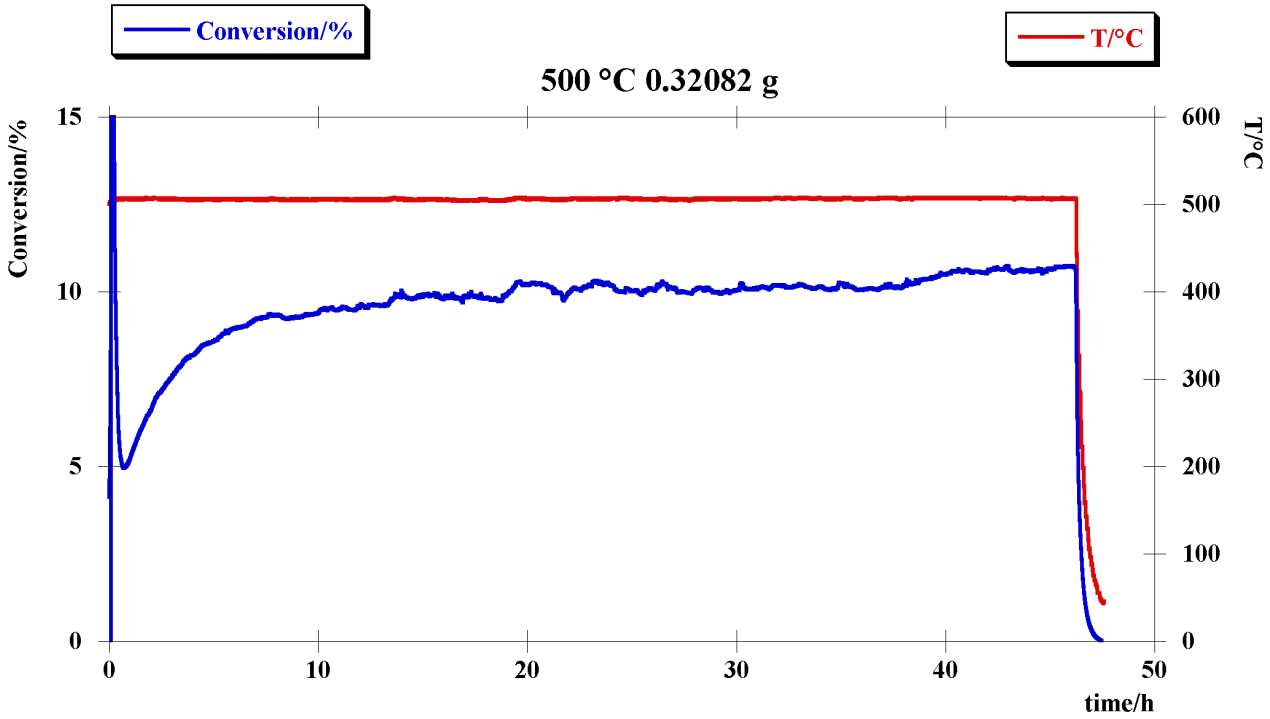

Fig. 29

In both the experiments no poisoning of the catalyst seemed to occur even for lengths lasting more than 40 hours. At the end of the second experiment, the crucible was found broken due to the load against its walls by the large carbon mass formed; the mass gain was 0.67413 g (more than twice the mass of catalyst used). In this case only a part of the carbon formed was treated chemically in order to remove the catalyst. In this case, beyond SEM analysis, also EDS mapping of the two parts of the carbonaceous product was performed:

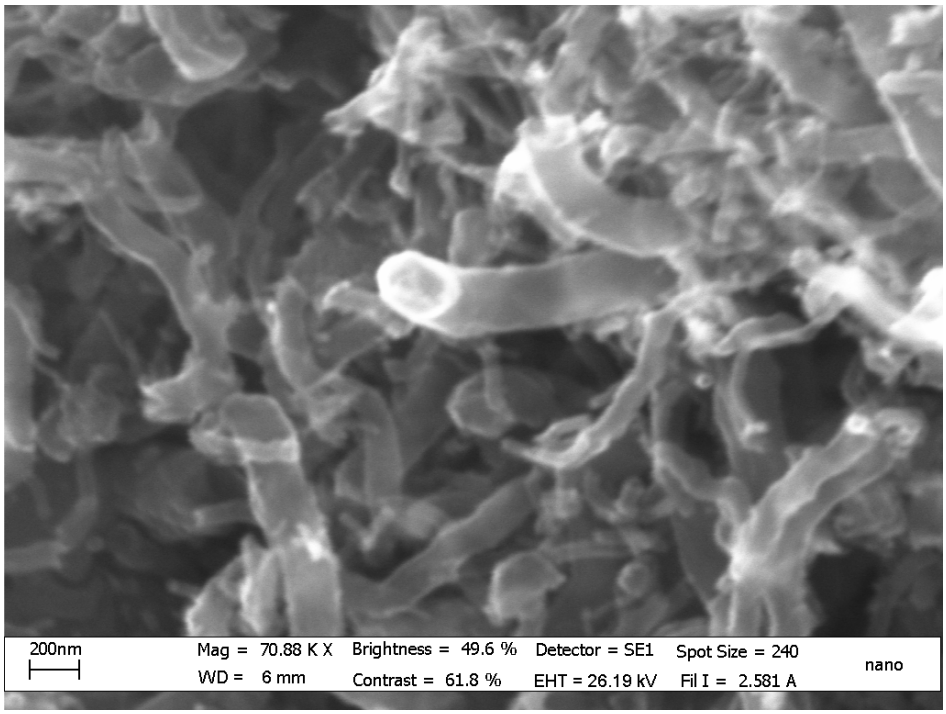

Fig. 30

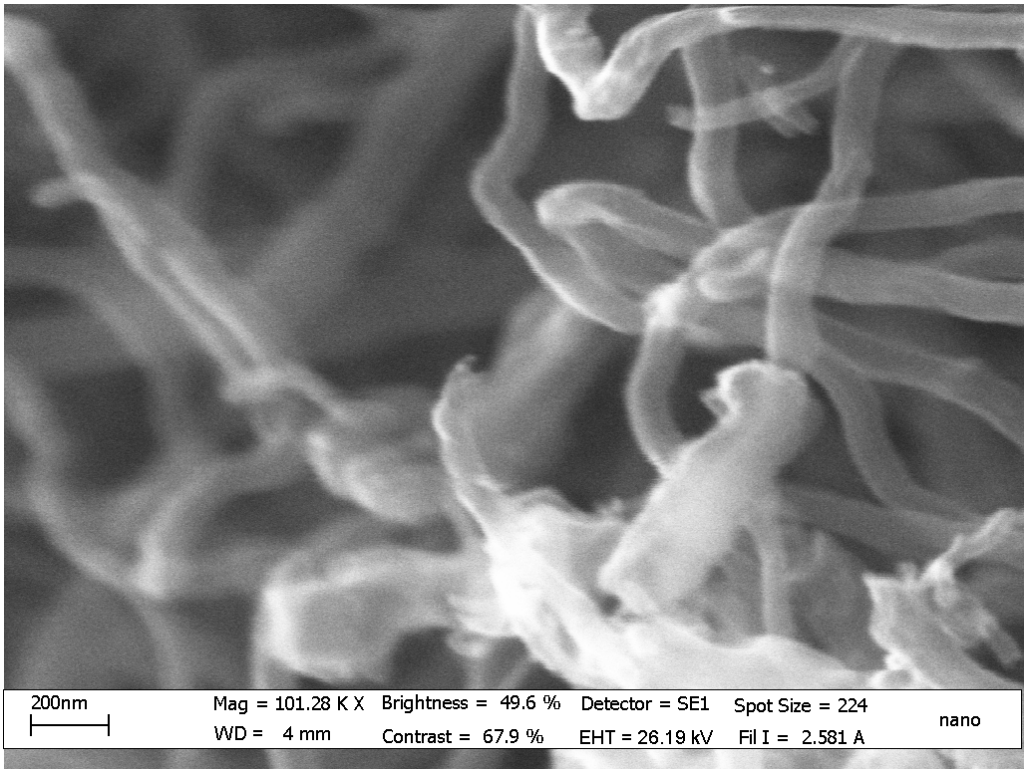

Fig. 31

Fig. 30 refers to a sample of CNTs (i.e. the solid product from CH_4 decomposition) containing the catalyst, and fig. 31 to a sample where the catalyst was separated from CNTs. At first glance, no particular difference appears between the two samples. If we have a look to the EDS maps of the samples:

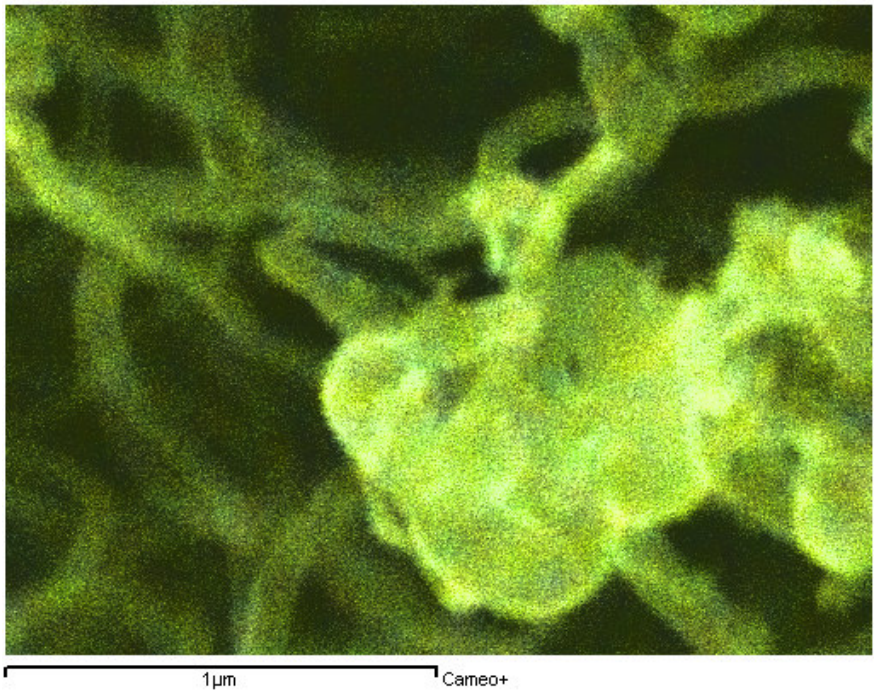

Fig. 32

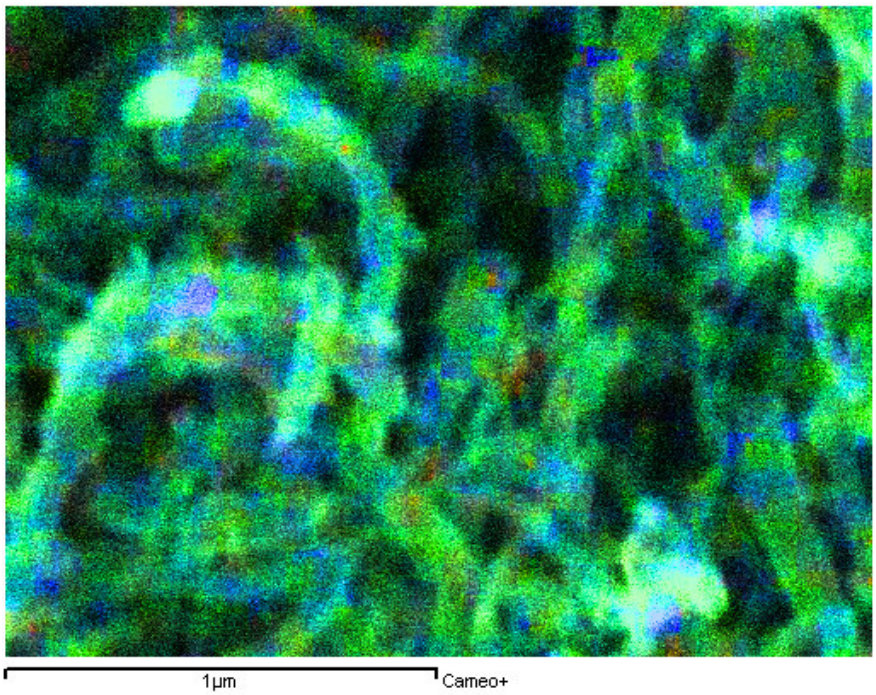

Fig. 33

we can observe: in fig. 32 an uniform colour distribution that refers to the emission of carbon; in fig. 33 two color distributions. The green one, that refers to carbon as before, and some blue localizations of several tens of nanometers, that refer to the emission of the catalyst. This last map was quite surprising because the size of the catalyst particles before the reaction are 2-3 orders of magnitude larger.

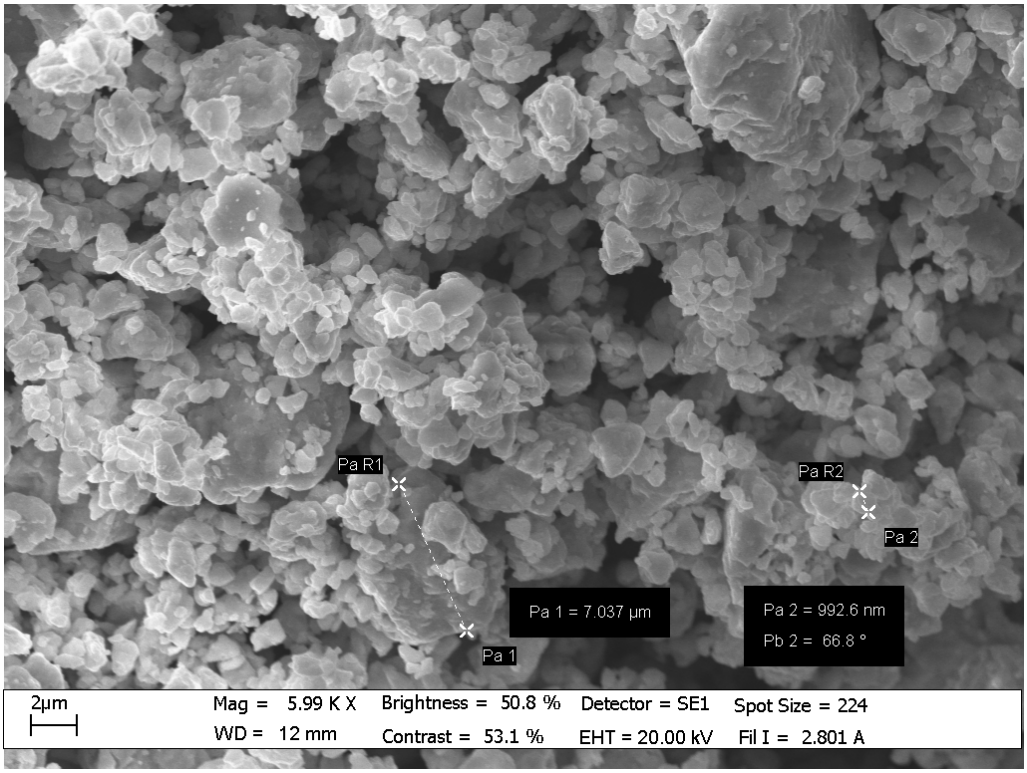

Fig. 34

The value of the BET surface area of the catalyst was found very low: only $0.683 \pm 0.007\ m^2g^{-1}$. So it is necessary to understand why the catalyst particles change from a micrometric to nanometric size, and why, though having a so small specific area, the catalyst shows good catalytic activity for prolonged periods without poisoning phenomena. The nanometric size of the catalyst particles attached to CNTs was afterwards confirmed by TEM observations, which also showed that the CNTs produced are multiwalled.

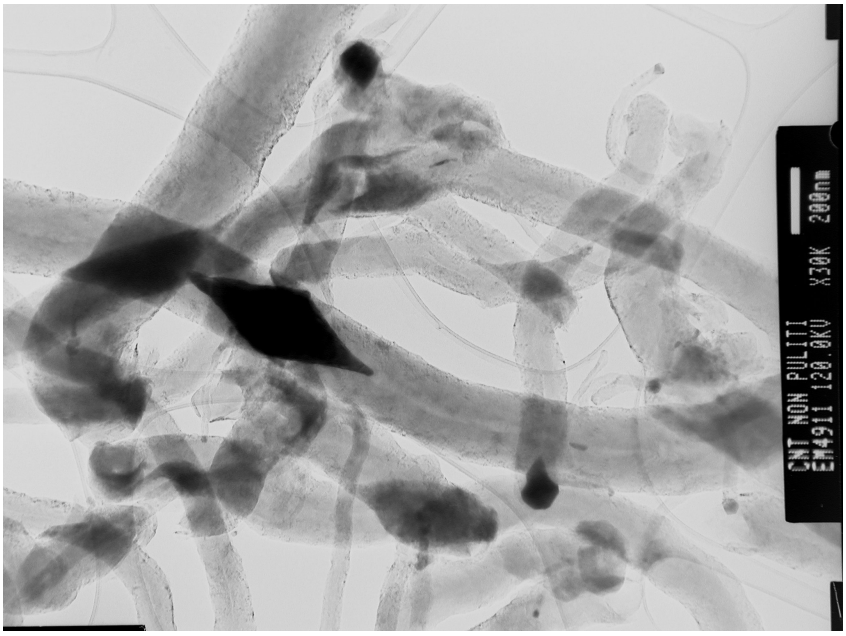

Fig. 35

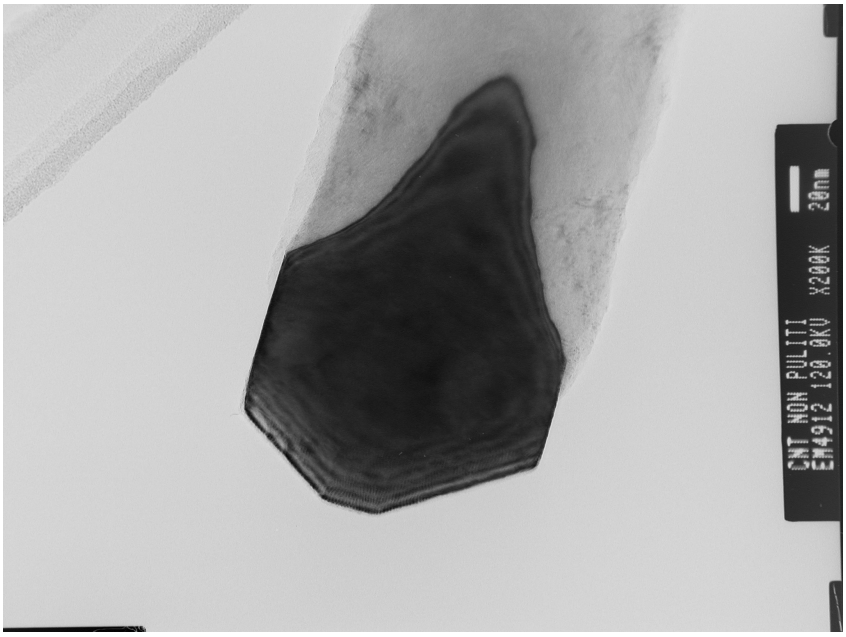

Fig. 36

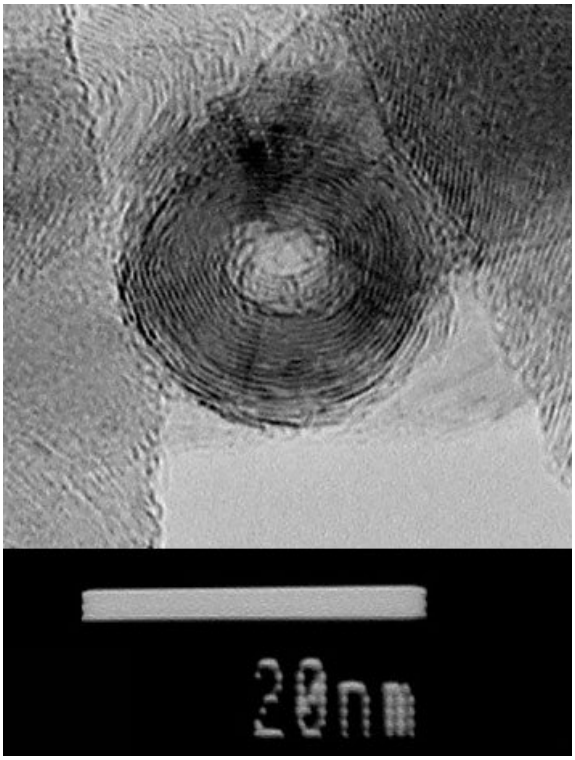

Fig. 37

The partly turbostratic arrangement of the walls, is shown by the XRD pattern (fig. 38), that gives a wall-wall distance of 3.409 Å, to be compared with the 3.354 Å spacing of graphite.

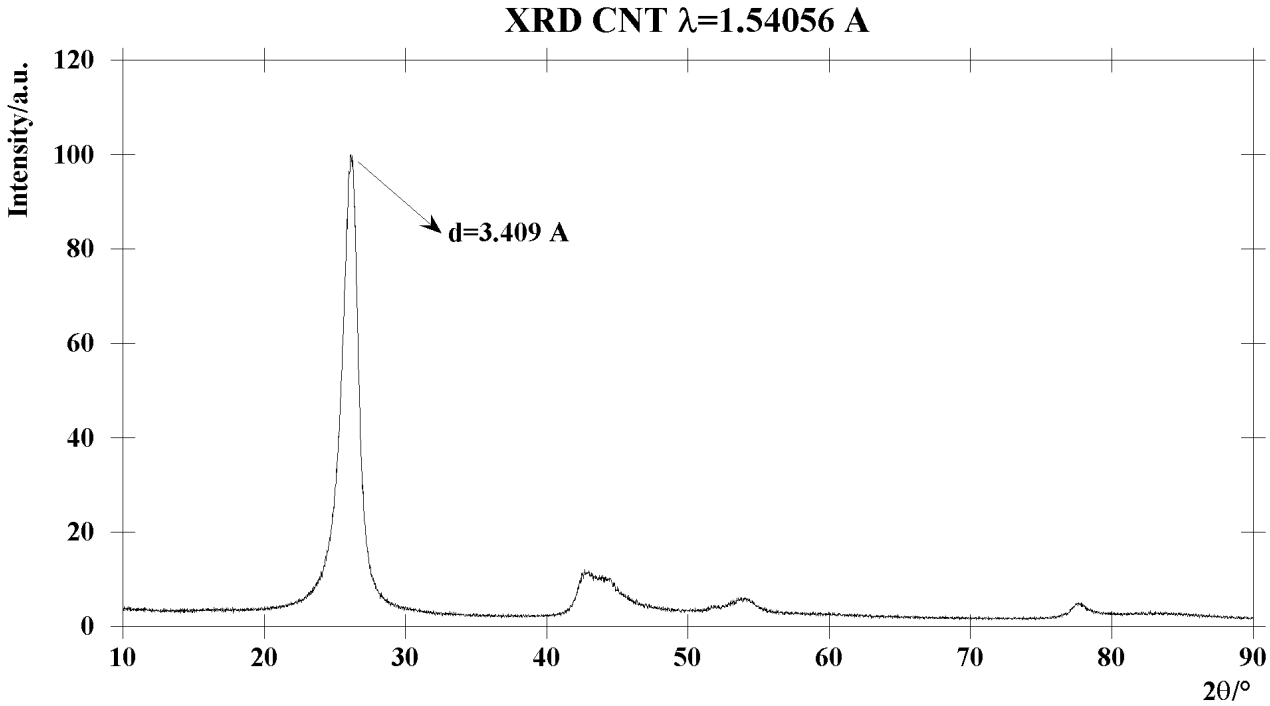

Fig. 38

3.1.3 Temperature dependence of CH_4 decomposition rate

In order to find the best temperature for the decomposition reaction maximizing the H_2 and CNTs production rate, at the same 5 sccm CH_4 flow rate, the temperature interval between 475 and 625 °C was explored. These experiments were also useful for acquiring information on the reaction mechanism. In figg. 39-45 the percent conversion and temperature versus time are reported:

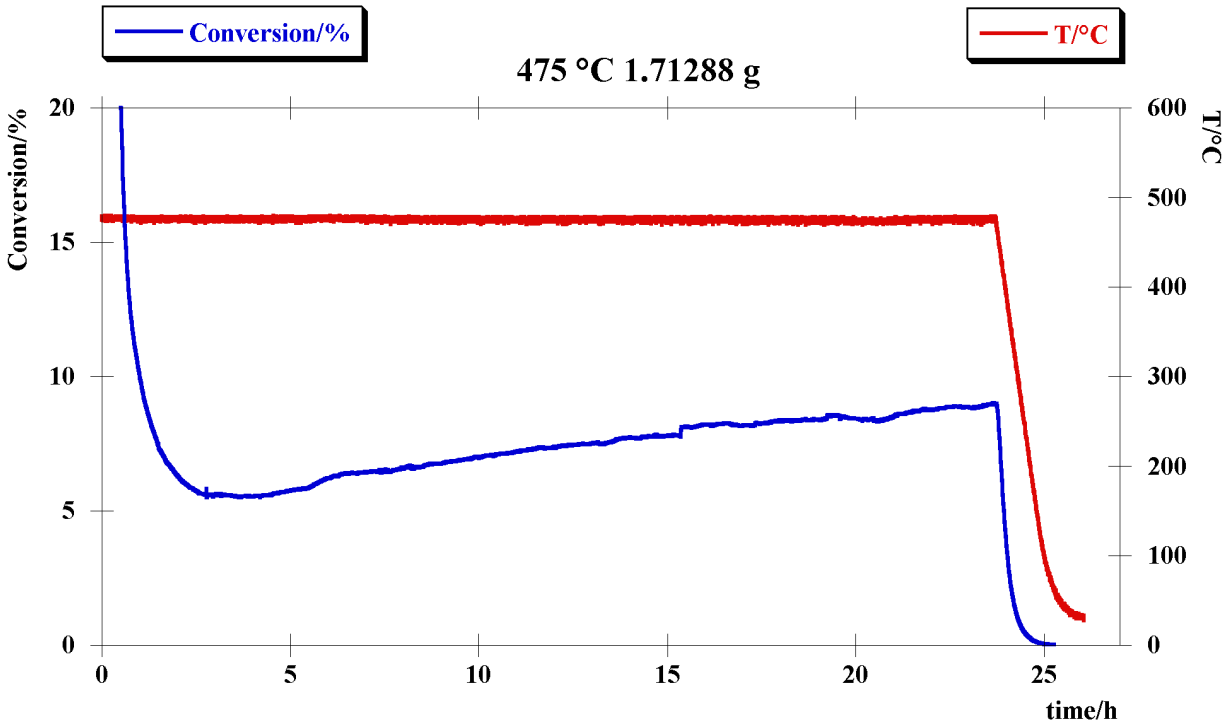

Fig. 39

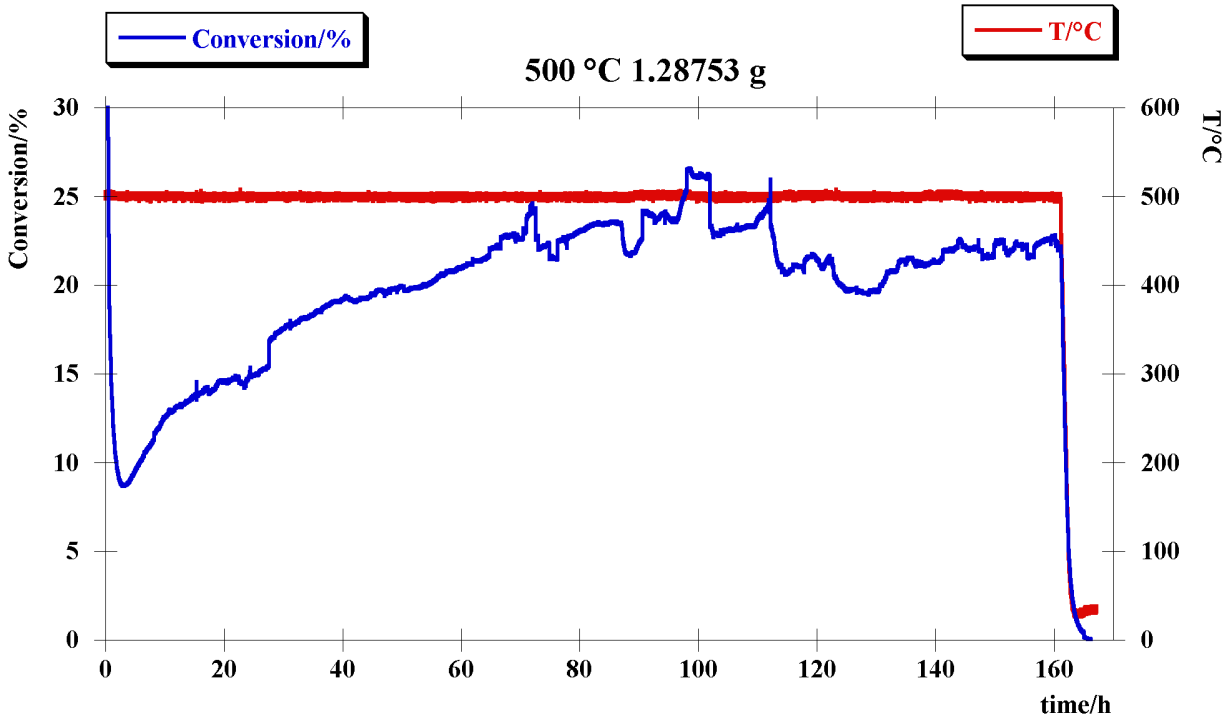

Fig. 40

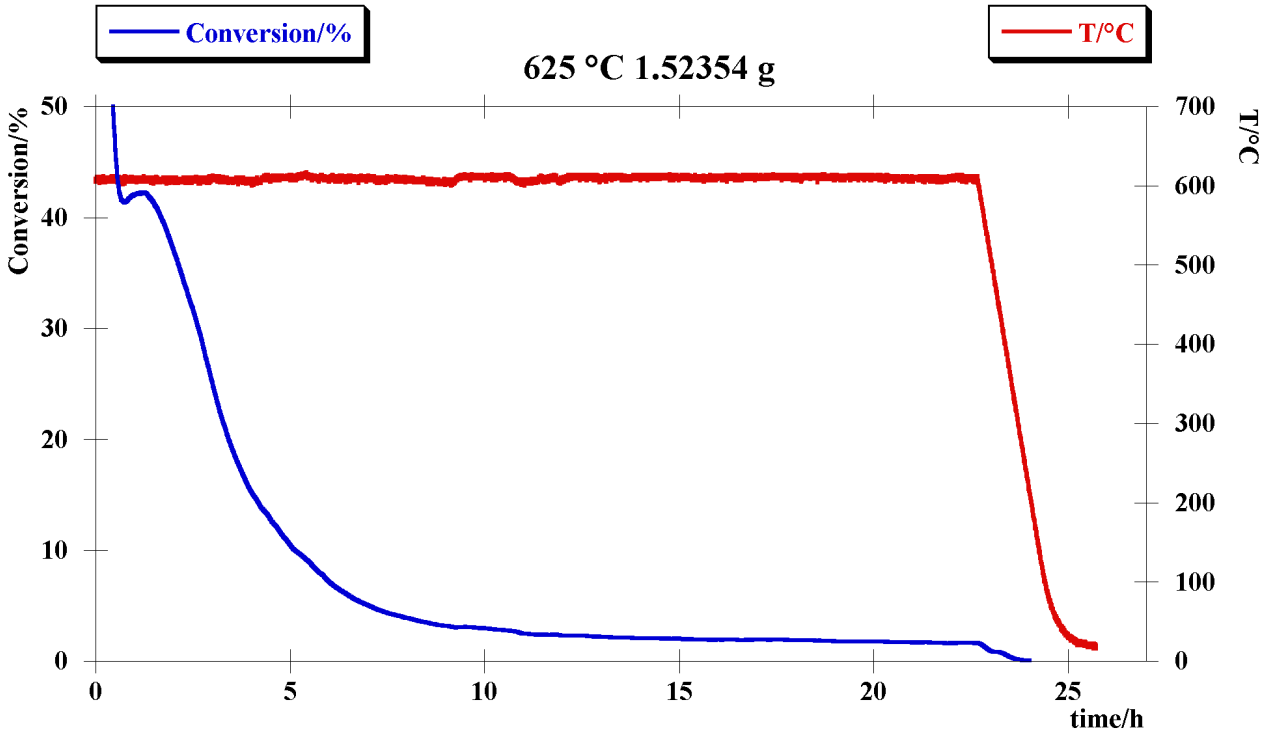

Fig. 45

A quite large amount of catalyst powder was used in each of the above experiments (1-3 g ca) in order to avoid preferential gas paths leading to a decrease in the conversion rates. The maximum conversion seem to increase by increasing temperature, with the apparent exceptions of the experiments carried out at 525 and 575 °C. It's reasonable to think that in these cases the flowing gas found preferential paths despite the precautions taken. Anyway, besides the increasing maximum conversion rate with temperature, a clear deactivation process emerges for temperatures ≥575 °C.

3.1.4 Some hypotheses on the reaction mechanism: experimental check

In order to understand the reaction mechanism, some hypotheses were taken into account, and each of them was experimentally verified.

- First hypothesis: normal heterogeneous catalytic process related to the surface active site concentration.

In order to verify this hypothesis, the catalyst was prepared in Raney form, so to have a high specific surface area, therefore a high number of active sites. For the catalyst synthesis, an Al excess was added to the reactant mixture and after melting by e-gun, the obtained ingot was leached in ~6M NaOH solution to remove Al. The measured BET surface area was 37.9±0.2 m^2g^{-1}, so

nearly two orders of magnitude higher than the “normal” catalyst. The catalytic test carried out in the same conditions used before, surprisingly, did not show better conversion value.

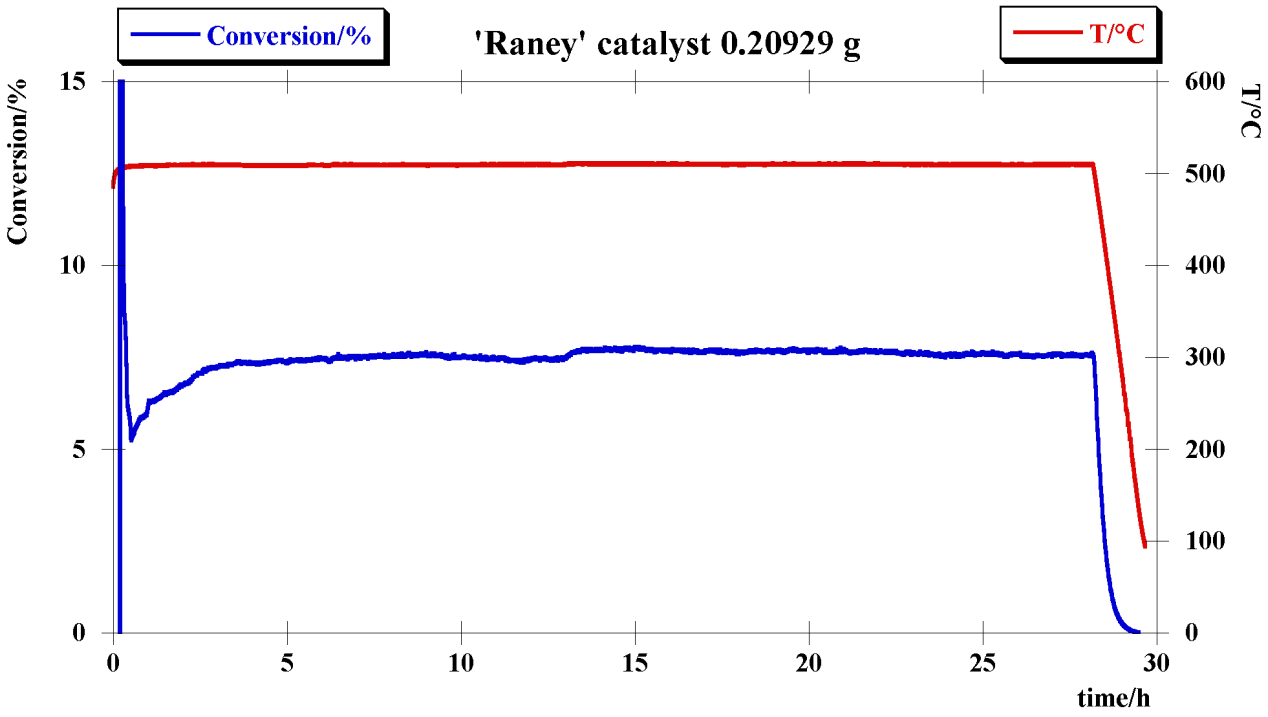

Fig. 46

Also in this case the carbon produced was found as CNTs, very similar to those ones produced by using the original catalyst:

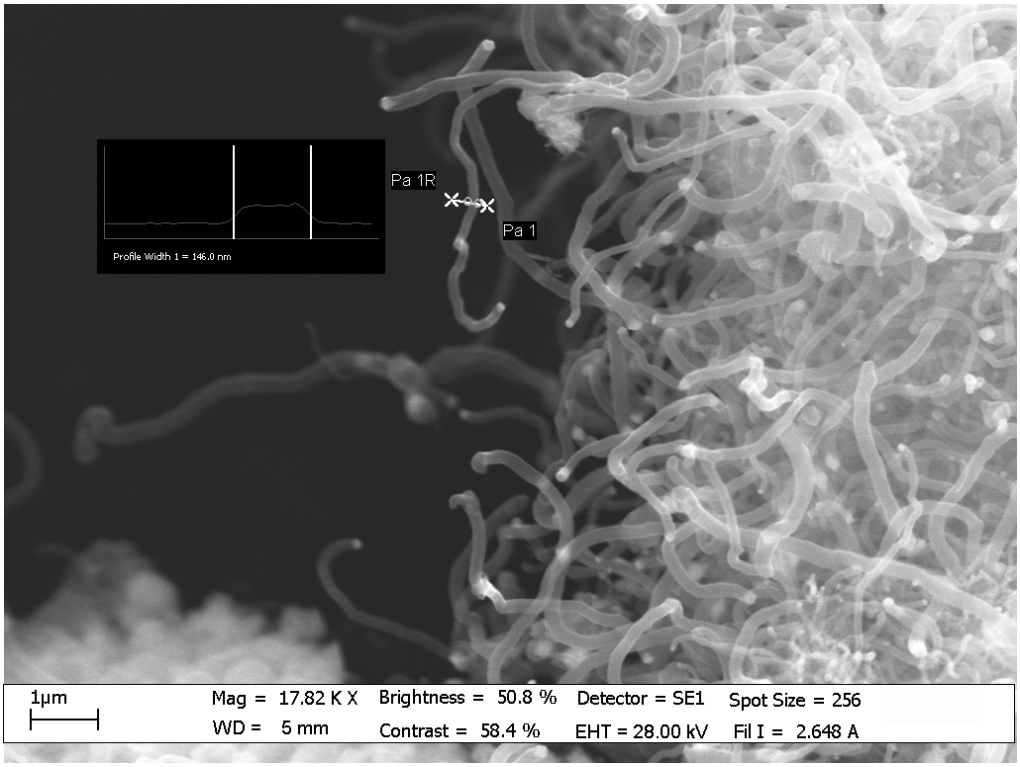

Fig. 47

- Second hypothesis: catalytic activity due to decomposition of the catalyst during the reaction

This hypothesis was immediately discarded after an ICP (Inductively Coupled Plasma) analysis performed on a sample of CNTs taken far from the catalytic bed (thus, not contaminated by the catalyst bed) and after the electron diffraction of a catalyst particle attached to a CNT. The former confirmed the catalyst stoichiometry, the latter its hexagonal structure and expected spacings.

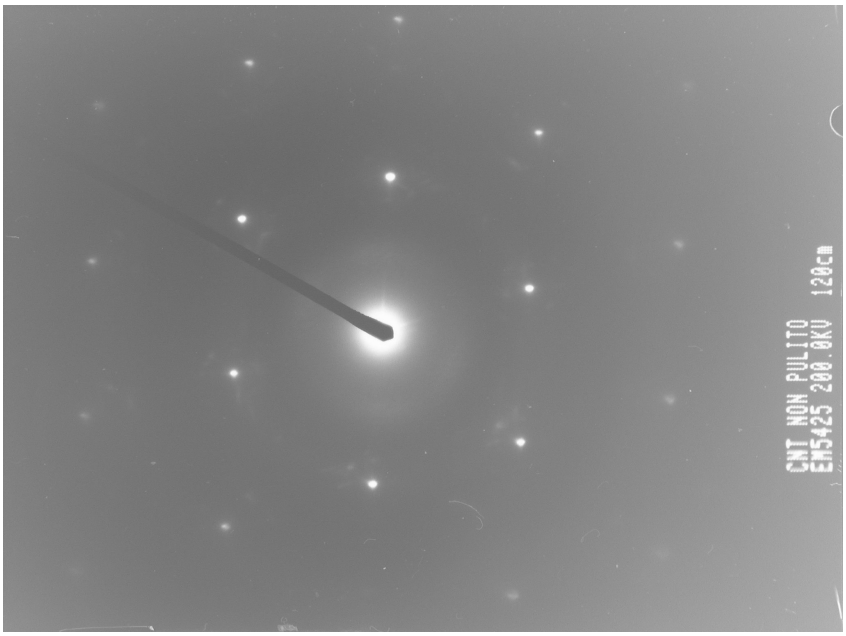

Fig. 48

- Third hypothesis: catalytic activity due to one of the components of the catalyst

Each component (two components) of the catalyst was separately used in catalytic tests in the same temperature and gas flow conditions of the catalyst. One component showed poor activity for a short time (fig. 49), while the other was substantially inactive (fig. 50).

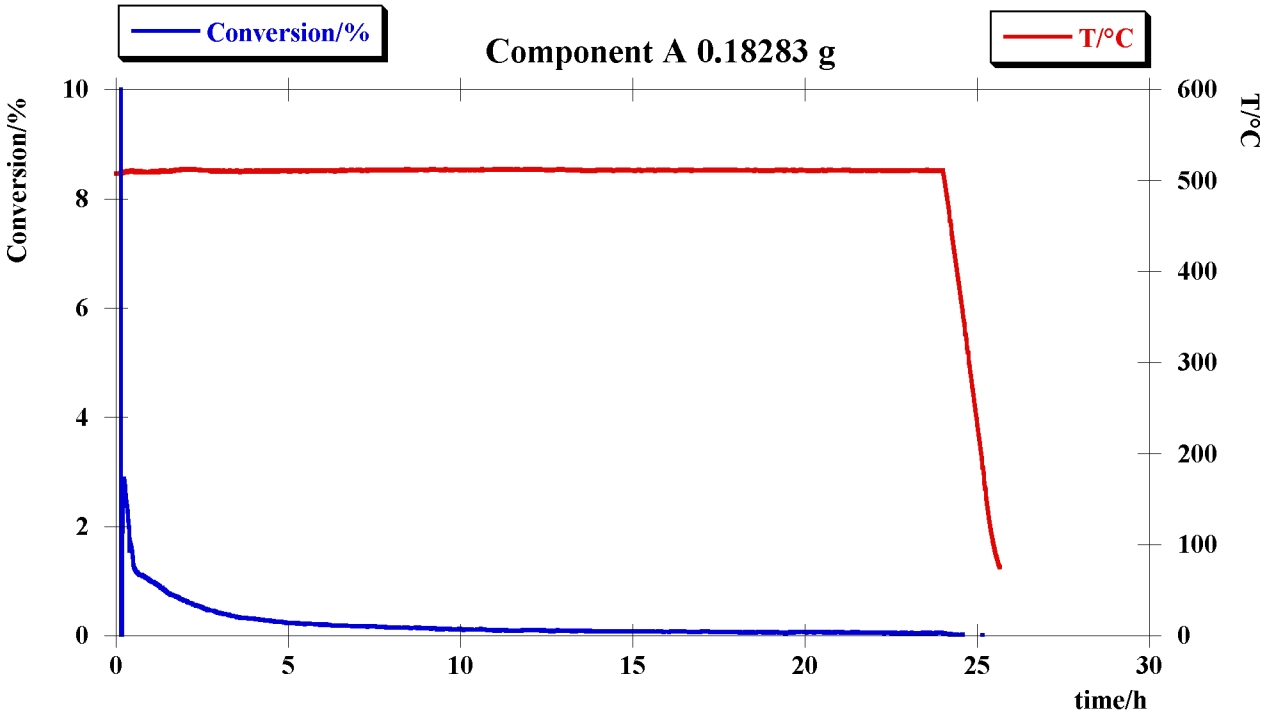

Fig. 49

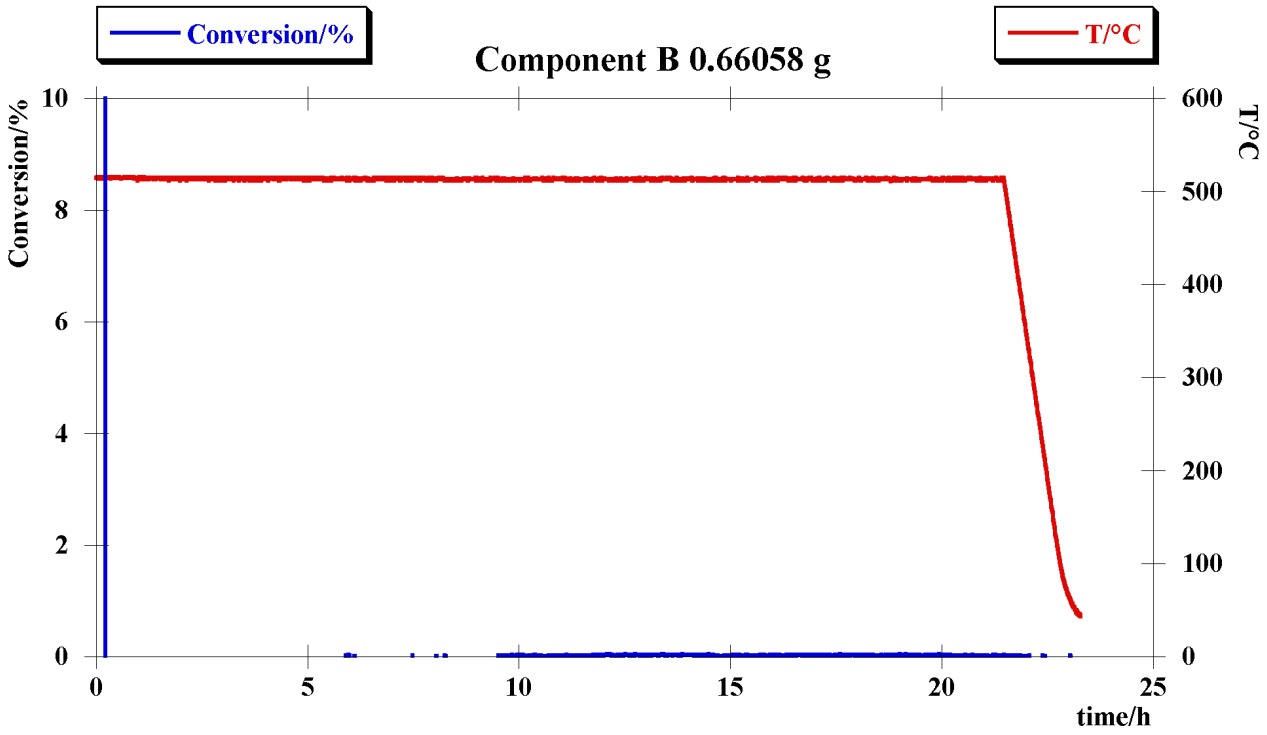

Fig. 50

The small quantities of carbonaceous deposits recovered in both cases were observed by scanning electron microscopy, and no CNTs were observed (fig. 51 for component A and fig. 52 for component B).

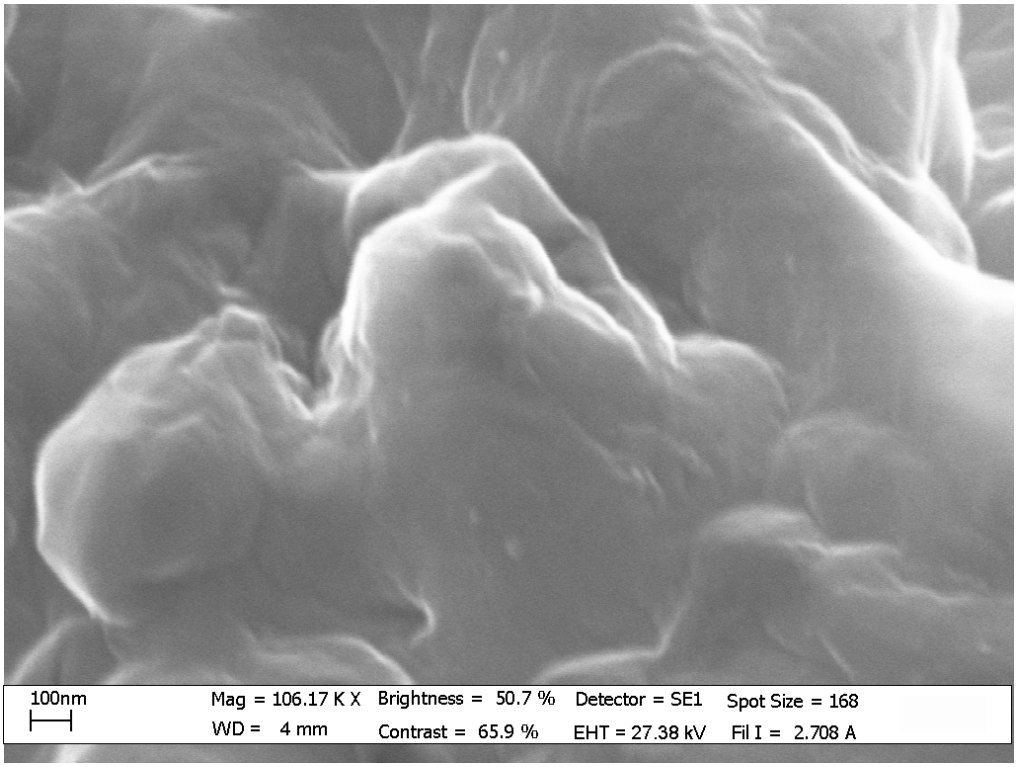

Fig. 51

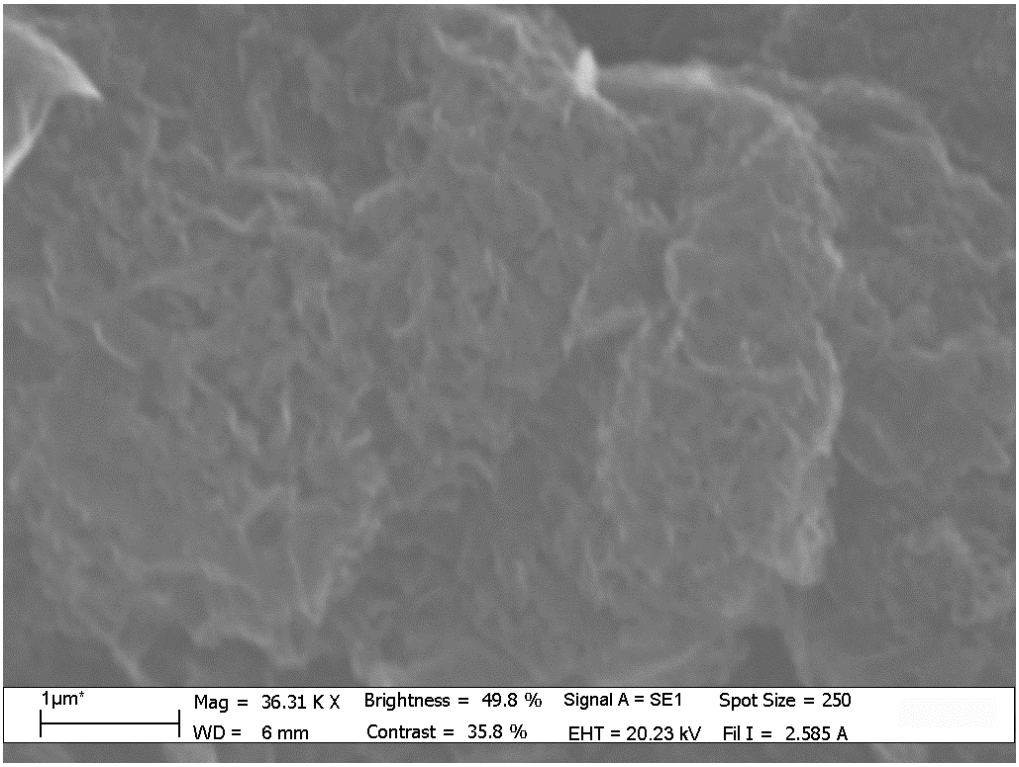

Fig. 52

- Fourth hypothesis: catalytic activity due to the CNTs initially formed (auto-catalysis)

CNTs deprived of the catalyst were subjected to the same catalytic test as above. No catalytic activity was observed:

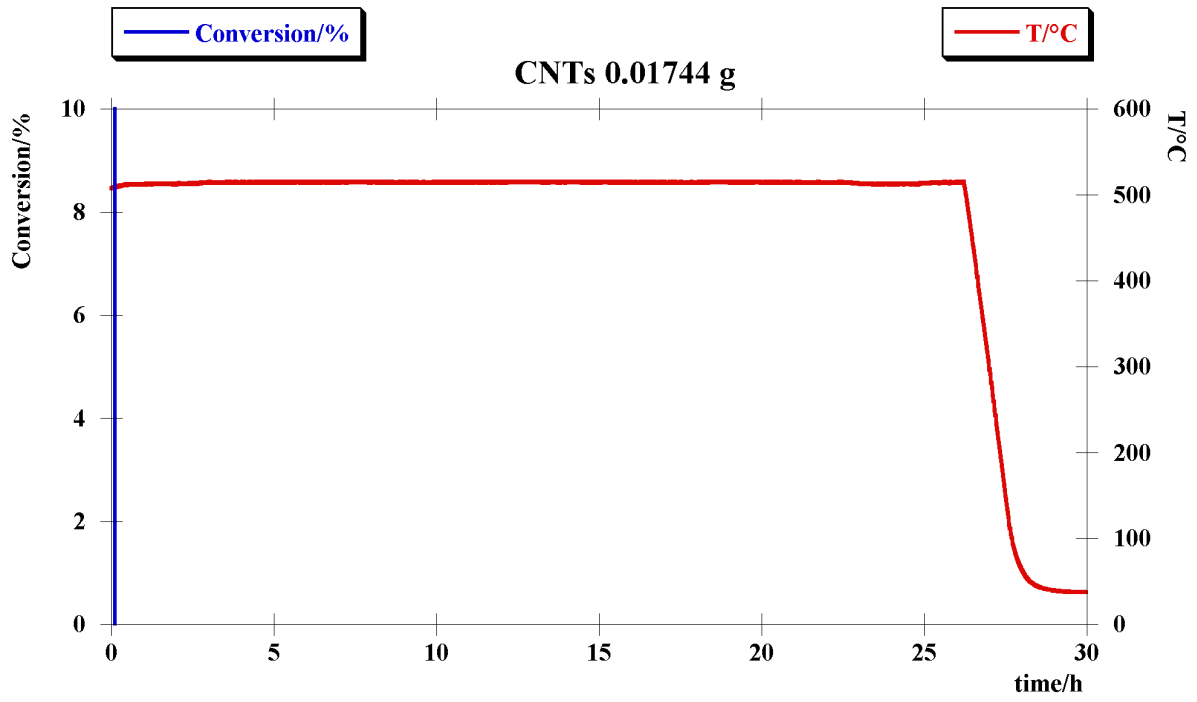

Fig. 53

On the other hand, CNTs containing catalyst nanoparticles showed an appreciable catalytic activity for about five hours:

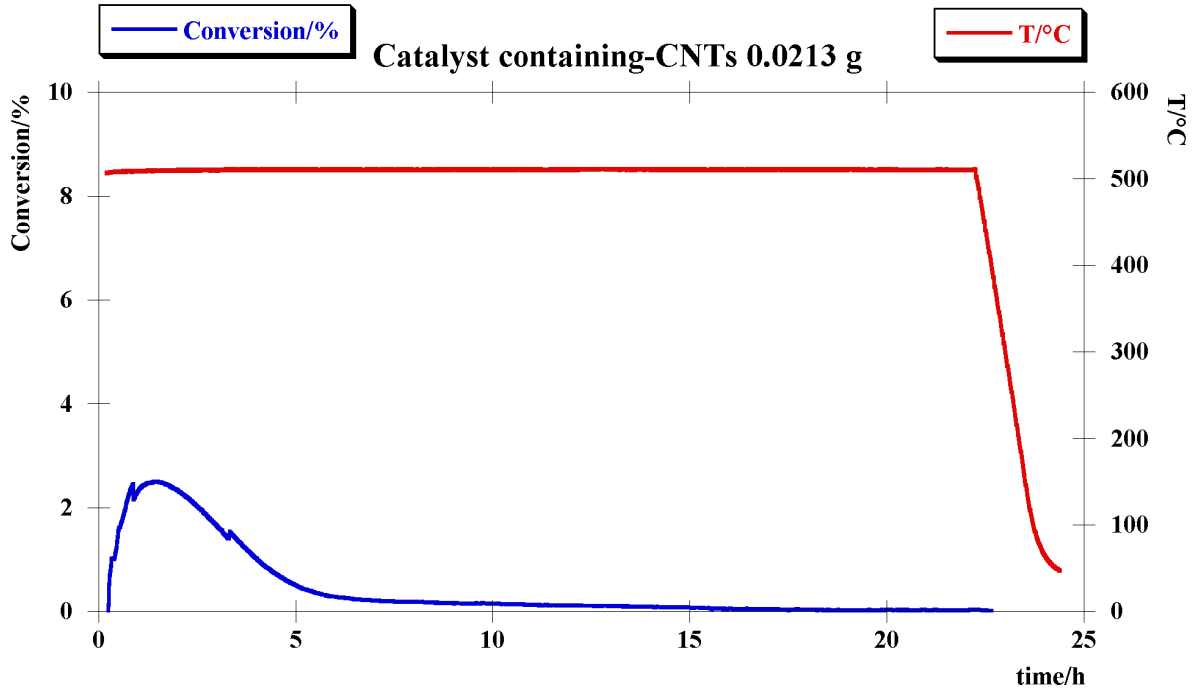

Fig. 54

Looking at the reaction product, we can see that at least two diameter distribution of CNTs are present:

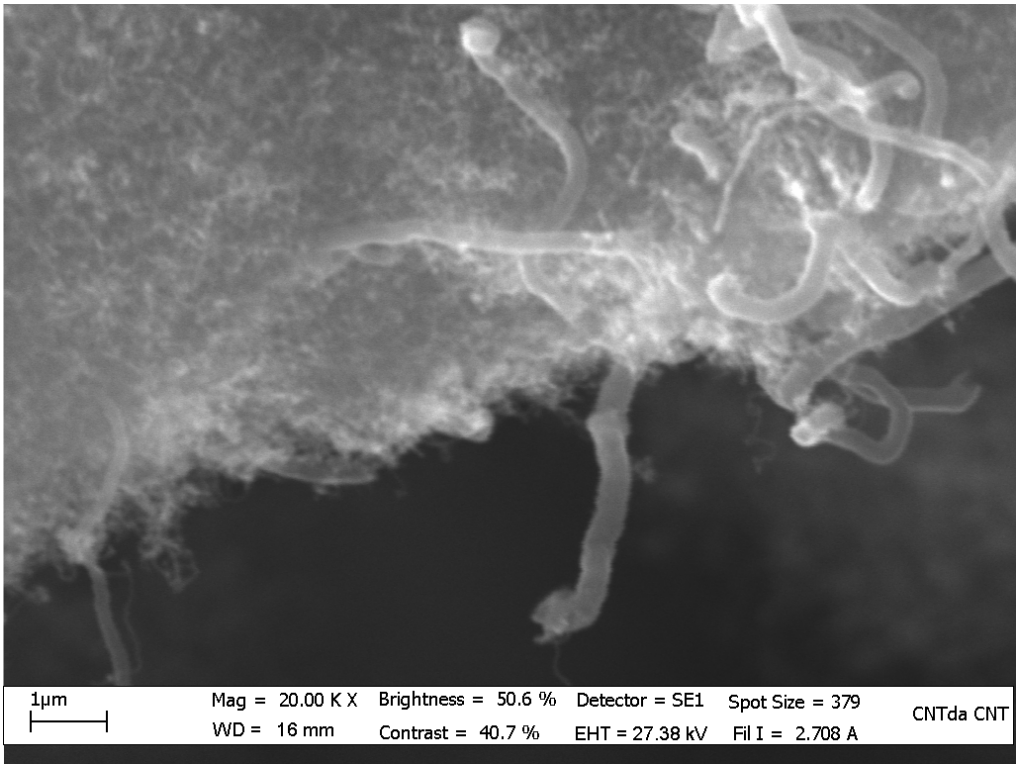

Fig. 55

From the image it is evident that large nanotubes, which were the ones used as catalyst, are surrounded by an entanglement of smaller CNTs which grew during the test.

-Fifth hypothesis: catalytic activity due to metal nanoparticles

By EDS mapping and TEM analysis of catalyst containing-CNTs, it is evident that metal nanoparticles are attached to CNT. It is possible that these nanoparticles are responsible for CNTs growth, acting as templates. In order to verify this hypothesis, we attempted to use directly metal nanoparticles as catalyst. And for simplicity, Ni nanoparticles (Ni was chosen because it is well known that Ni-based catalysts are efficient for CNTs growth) were synthesized according to the procedure of Hou and Gao [39]. This procedure consists in the reduction of $Ni(acac)_2$ (acac: acetylacetonate) with $NaBH_4$ under Ar in hexadecylamine at 100 °C:

$$Ni(acac)_2 \xrightarrow[HDA,NaBH_4]{\Delta} Ni(nano)$$

The nanoparticles obtained were characterized by ICP and combustion analysis, XRD and TEM. The combination of chemical analysis techniques gave the results:

C = 5.8±0.3; H =1.0±0.1; N = 0.4±0.1; Ni = 4.6±0.1, inorganic inert impurities up to 100 (all results in weight %).

The XRD spectrum (not reported) did not reveal peaks of crystalline Ni, and this is probably due to the low reaction temperature. TEM images of the reaction product revealed well formed nanometric Ni nanoparticles surrounded by a shell of hexadecylamine:

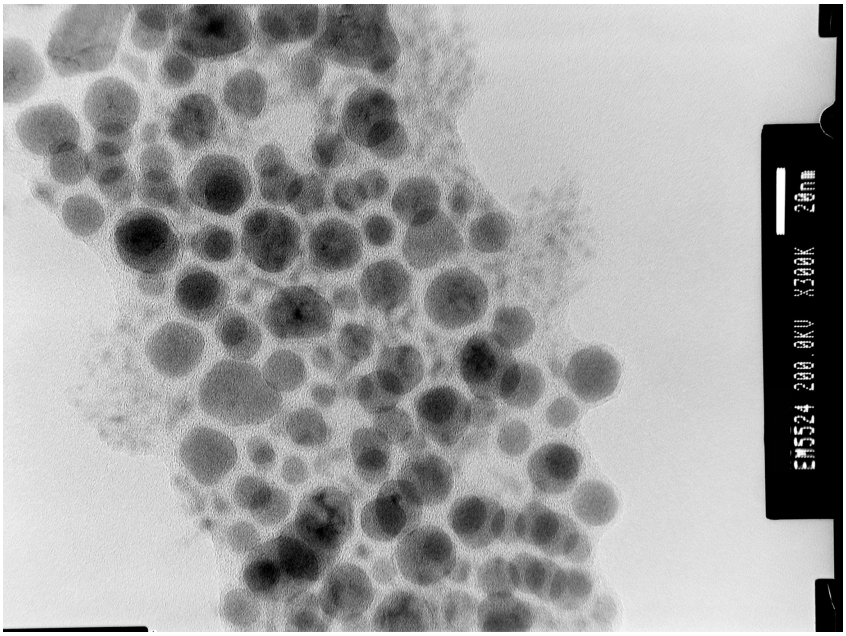

Fig. 56

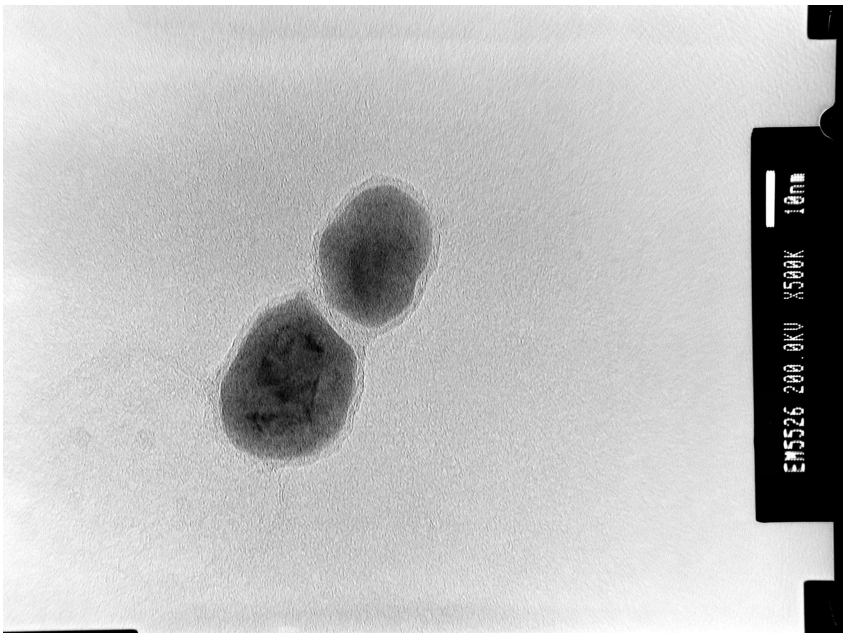

Fig. 57

The diameter distribution was also examined (fig. 58):

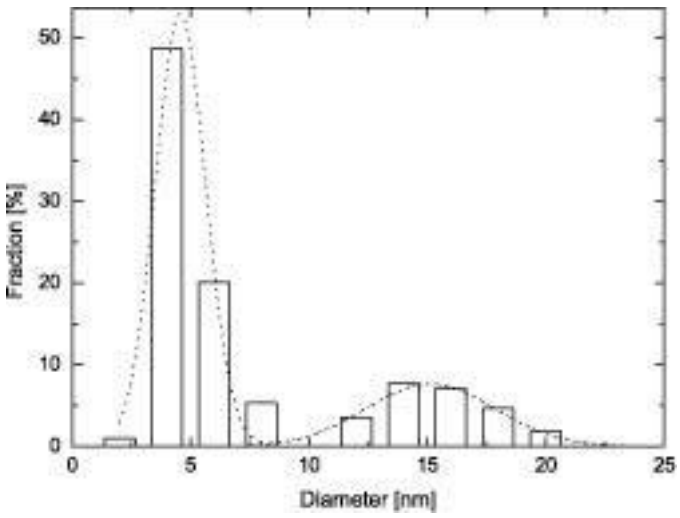

Fig. 58

The gaussian analysis of the distribution (dot line) gives two mean diameters of the particles, namely d_1 = 4.6 nm and d_2 = 15.4 nm. This is probably due to high concentration gradients during the addition of $NaBH_4$ to the $Ni(acac)_2$ solution. To avoid sintering of nanoparticles during the catalytic test, it was necessary to disperse them over a high surface area inert solid. For doing this, 0.18371 g of the synthesized material, *i.e.*, 0.0084±0.0002 g of Ni nanoparticles were suspended in 30 ml of n-hexane and 0.55098 g of MCM-41 silica (960±1 m^2g^{-1}) were soaked in the suspension under stirring at room temperature. The stirring was continued until to the surfactant liquid became transparent. Then, the temperature was gently raised up to about 70 °C and kept constant until to the solvent full evaporation. The solid catalyst was recovered and dried under vacuum. Then, 0.15548 g of this catalyst were used in the catalytic test. The conversion, though being very low, was appreciable:

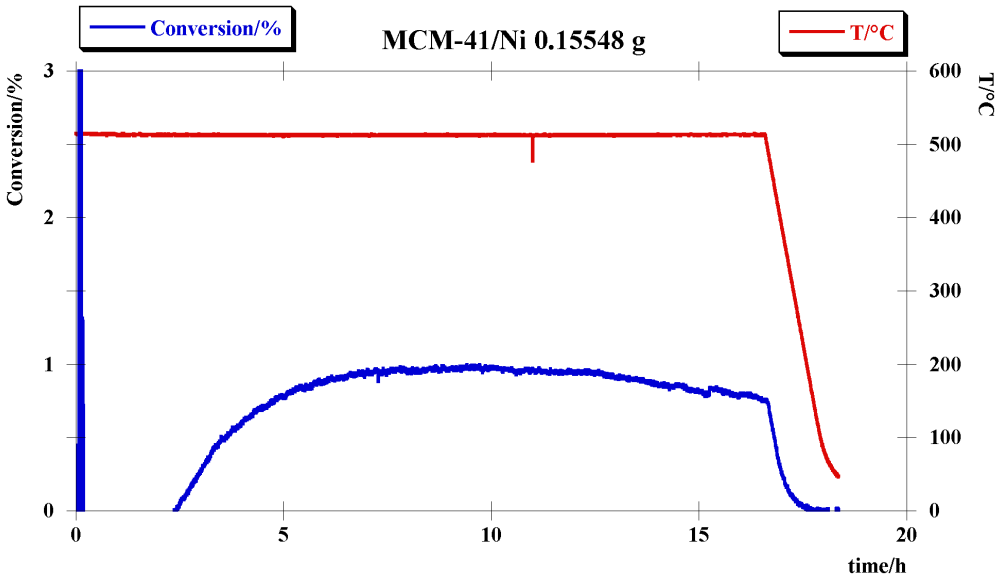

Fig. 59

The reaction product was recovered and washed with hot 6M NaOH to dissolve the MCM-41 silica. Then it was characterized by XRD, SEM and TEM. The XRD pattern (fig. 60) reveals in addition to the CNTs diffraction lines, also the main Ni line:

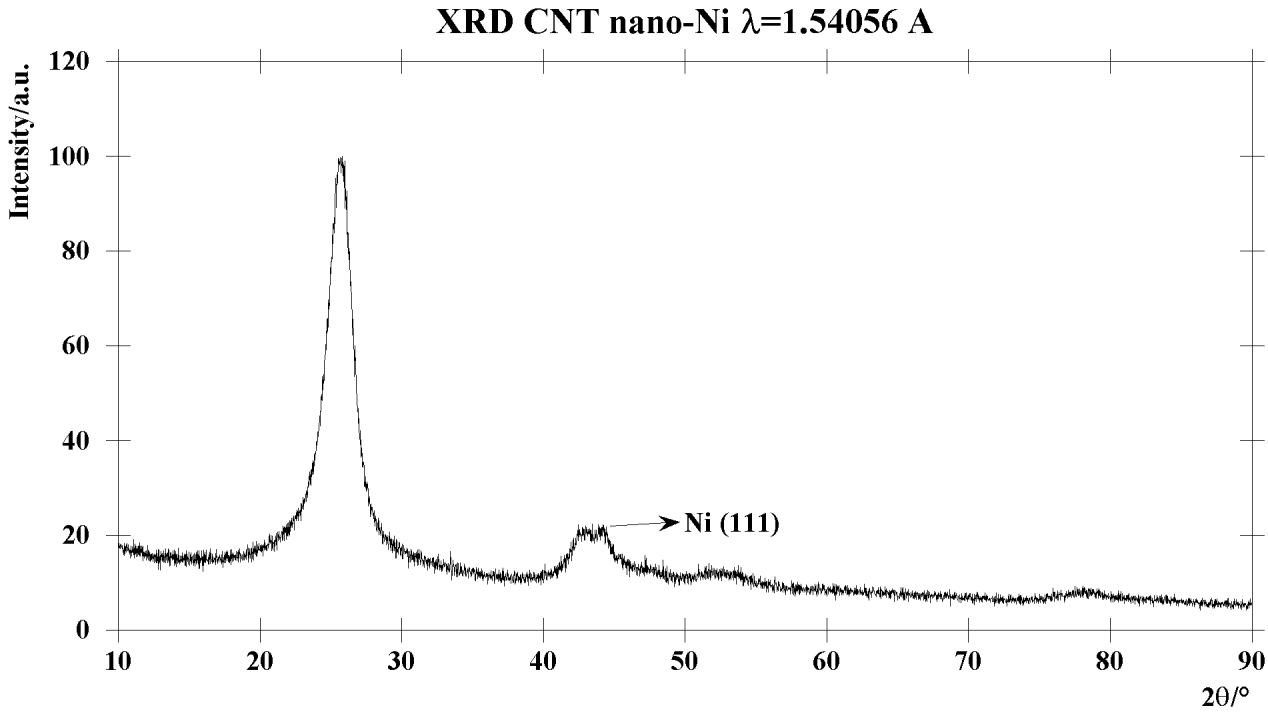

Fig. 60

During the catalytic process, the high temperature allowed the nanoparticles to crystallize. SEM analysis showed CNTs having very small diameters:

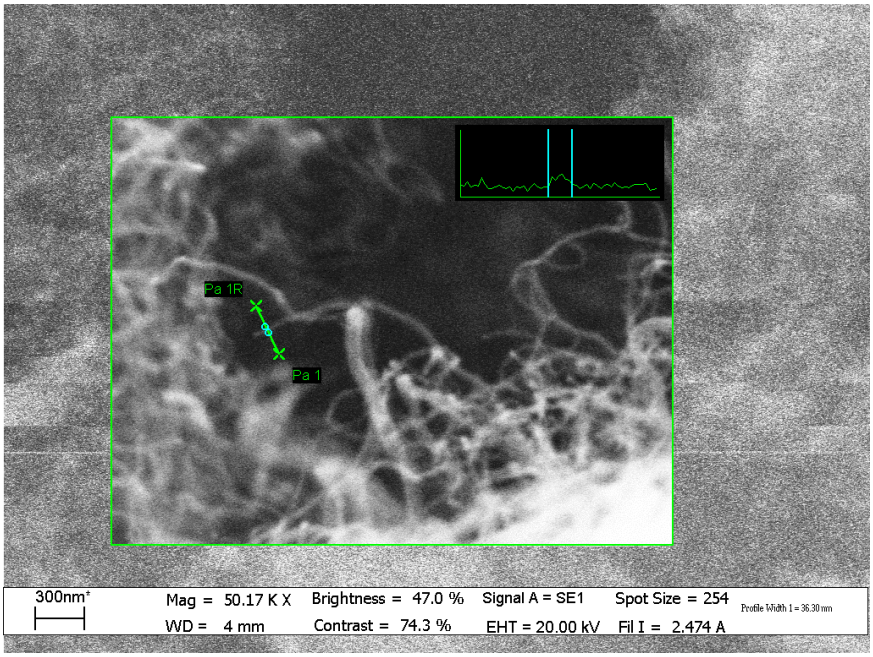

Fig. 61

This was also confirmed by TEM images:

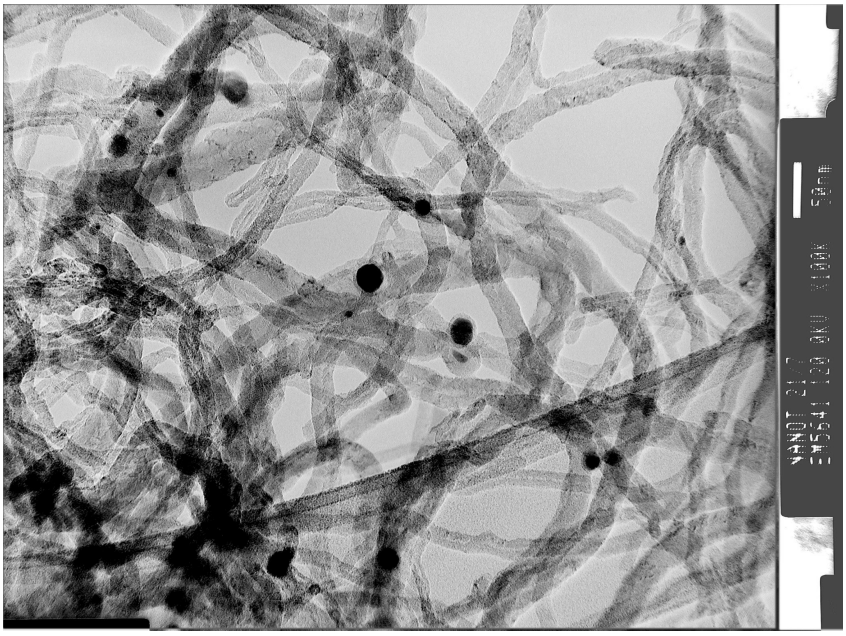

Fig. 62

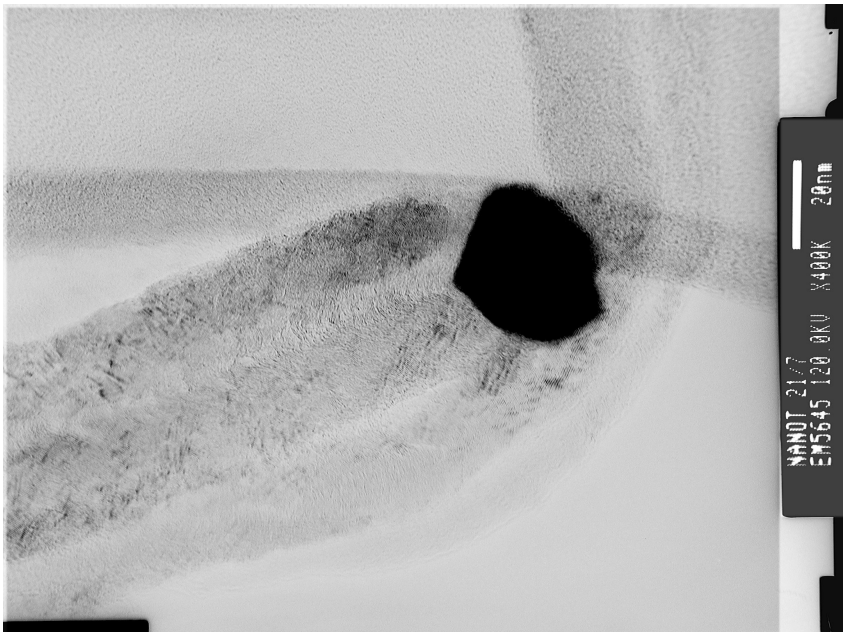

Fig. 63

It is evident the similarity of these TEM images and the images of the CNTs produced by the binary catalyst. In both cases, there is a nanoparticle attached to one of the ends of the CNTs, and the attached site is tip-shaped. This last hypothesis seems to be the most convincing one, because of the strict analogies between the CNTs and the attached metal nanoparticles present in both cases. But a fundamental question remains: how can micrometric size catalyst particles transform into nanometric size ones? In the following paragraph we will try to answer to this question.

3.1.5 The proposed mechanistic model

As seen in par. 3.1.2 and 3.1.4, each not chemically-treated CNT has a tip-shaped nanoparticle attached to one of his ends; so it would be reasonable to think that these tips are initially present on the surface of the catalyst, leading to nucleation and growth of CNTs. During CH_4 decomposition, the carbon atoms formed on these tips organize themselves as polyyne rings stabilized by interaction with the surface (nucleation process) [40] and adjacent rings condense together leading to the growth of a CNT wall. Only rings with similar diameter can condense and this because of bonding tension. This explains why MWCNTs are formed. Once a ring has condensed with other two rings, it detaches from the catalyst surface because all its bonds are saturated, and so the surface is free to continue the CH_4 decomposition. Due to the chemical nature of the catalyst, it is expected that it can absorb H_2 through an intermediate dissociative adsorption step. The hydrogen produced during the reaction is therefore in some extent absorbed by the catalyst thus producing lattice expansion and increasing the stress at the grain boundary interface (gbi) between the crystallites in each grain of the catalyst powder. Another source of stress is given by expected C insertion at the gbi. When the elastic energy ε produced by the stress is higher than the free surface energy change, Γ, the crystallites separate. A scheme is given in fig. 64, where σ and S are, respectively, the interfacial tension and interfacial surface area, while some explicative drawings are given in figg. 65-67.

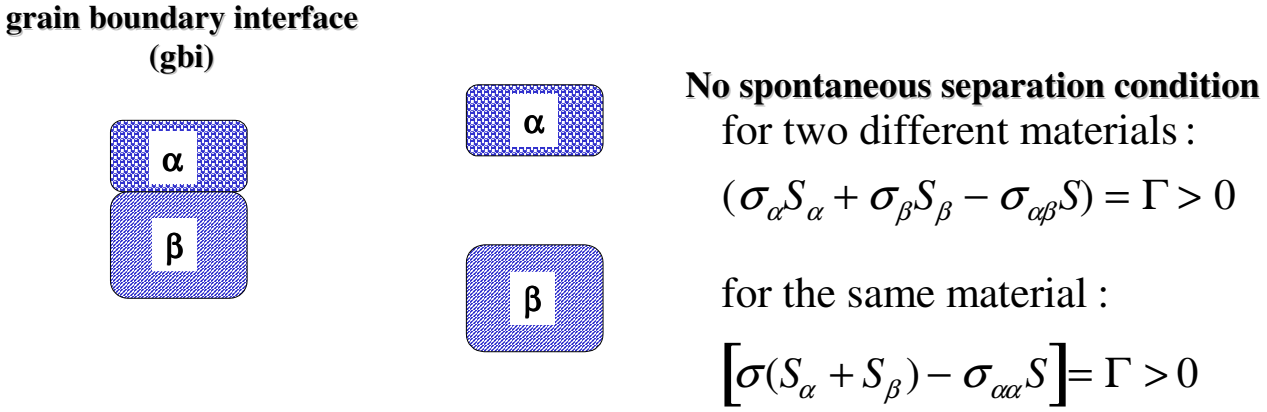

Fig. 64

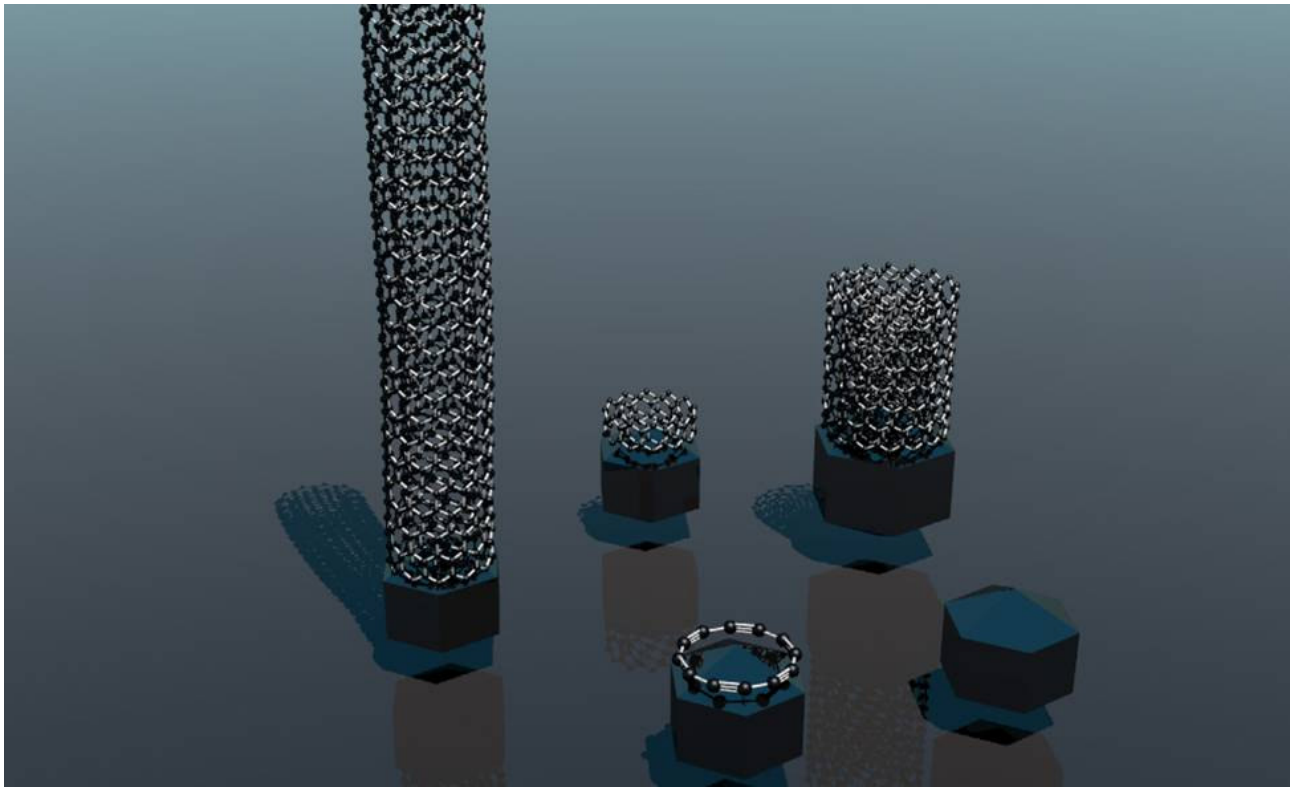

Fig. 67

When a nanoparticle detaches, it leaves a clean surface, generating other tips ready to decompose CH_4 and organize C atoms for the growth of more CNTs. As seen in par. 3.1.3, at T≤550 °C, a constant reaction rate was observed for long times without any appreciable deactivation (the reaction carried out at 500 °C lasted more than 160 hours!), while for T≥575 °C a deactivation process occurs, and this process becomes faster with temperature. This phenomenon may be attributed to a dynamic process between C atoms formation and their surface diffusion towards the CNT nucleation and growth site. When the temperature is below a certain threshold, the rate of formation of C atoms on the catalyst surface is lower or at most equal to the rate of C atoms removal by surface diffusion, the methane decomposition process proceeds without deactivation. Otherwise, if the rate of C atom formation on the catalyst surface becomes greater than the CNT growth rate, the catalyst surface is rapidly covered by C and thus poisoned. TEM and HR-TEM analysis seem to confirm these arguments; in the following the photos of samples grown from 475 to 625 °C are displayed.

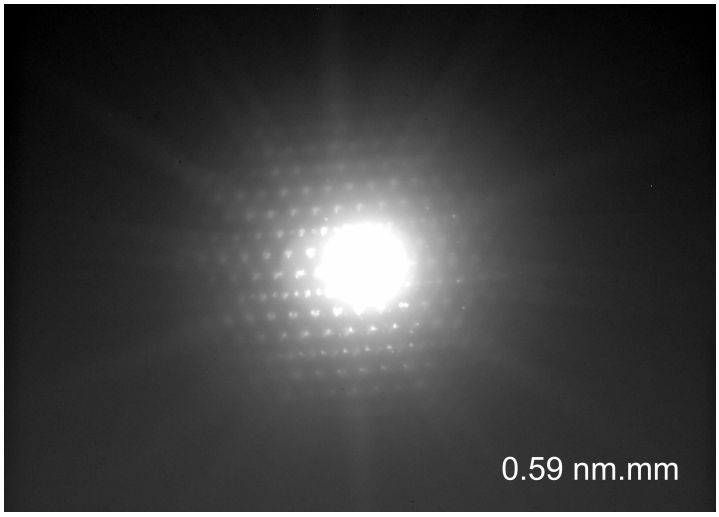

Fig. 101

Electron diffraction pattern of the metal nanoparticle shown in fig. 99.

From these images, it is evident that up to 575 °C a large amount of nanotubes is produced, whereas at 600 and 625 °C the amount of CNTs decreases drastically. In these two cases the metal nanoparticles formed are embedded in no-CNT type carbon (beautiful examples are shown in figg. 90 and 99) that prevents them to came into further contact with CH_4, leading to the quenching of the decomposition reaction. Anyway, in all the cases the nanoparticles are single crystals, as demonstrated by the electron diffraction patterns. This means that also in this case the reaction follows the same mechanism, but in order to avoid deactivation, the rate of methane decomposition must be at most equal to the rate of C atom surface diffusion as discussed before. It is also important to stress that the carbon layers (i.e. the CNT walls) grow parallel to the tip surface as shown in the HR-TEM photos referring to CNT-nanoparticle's tip interface (figg. 74, 78, 82, 86). This supports our hypothesis of C-ring condensation mechanism leading to the CNT growth.

3.1.6 Phenomenological model for CNTs nucleation and growth

It is clearly established [41] that the formation of CNTs occur by a process that involves both nucleation and growth stages. Now we define the critical cluster of size *n-1* as the smallest cluster for which, after the gain of a monomer (in this case a C atom), the probability of growth becomes higher than 0.5. So the smallest size cluster has size *n*. The aim is to develop analytically a model for the nucleation and growth of CNTs. We define the nucleation density *N(t)* as the number of stable clusters at time *t*, and the growth law of stable cluster that gives the dependence of the cluster size on both the actual time *t* and birth time $t'<t$. The phenomenological growth law can be written as:

$$m(t-t')=\rho l(t-t') \qquad (3.1.6.1)$$

where *m(t-t')* and *l(t-t')* are respectively the mass and the length at time *t* of the CNT that started growing at time *t'*, and ρ its linear density. The time dependence of the total mass of CNT can be written as:

$$M(t) = \rho \int_0^t I(t')l(t-t')dt' \qquad (3.1.6.2)$$

where *I(t)* is the nucleation rate $\frac{dN(t)}{dt}$. The mass formation rate is given by $\frac{dM(t)}{dt}$:

$$\frac{dM(t)}{dt} = \rho \int_0^t I(t') \frac{dl(t-t')}{dt} dt' \qquad (3.1.6.3)$$

Experimentally, it is evident that *I(0)=0* and $dI/dt\big|_{t=0} > 0$ and that after an induction period t_s, the nucleation rate reaches a steady state. In the case of a steady state nucleation for $t>\tau_n$, with τ_n the characteristic time of nucleation, the nucleation rate can be written as:

$$I(t) = I_s(1-e^{-t/\tau_n}) \qquad (3.1.6.4)$$

and the linear growth rate as:

$$l(t) = l_\infty(1-e^{-t/\tau_g}) \qquad (3.1.6.5)$$

where τ_g is the characteristic time of growth.

Using these formulas in the equation of the mass formation rate, we have:

$$\frac{dM(t)}{dt} = \rho I_s l_\infty \left[\left(1-e^{-t/\tau_n}\right) - \frac{\tau_g}{\tau_g-\tau_n}\left(e^{-t/\tau_g} - e^{-t/\tau_n}\right) \right] \qquad (3.1.6.5)$$

where the steady state value is given by $\rho I_s l_\infty$, which is independent of τ_n and τ_g. The steady state is reached when $t>max(\tau_n, \tau_g)$ By this equation it is possible to fit the experimental data with a two parameter plot in order to obtain τ_n and τ_g.

3.1.7 Physical model for the nucleation and growth of CNTs

As seen before, the experimental data indicate that catalyst nanoparticles act as nucleation centers and they provide catalytic sites for CH_4 decomposition. Now, considering that before starting the reaction we do not have nanoparticles, but only micrometric-size polycrystals, so at different times during the reaction the nanoparticles contained in a polycrystal are exposed to the gas. Defining $N_0(t)$ as the nanoparticles available for nucleation at time *t*, the nucleation rate is given by:

$$\frac{dN_0(t)}{dt} = G - \frac{N_0(t)}{\tau_n} \qquad (3.1.7.1)$$

where G is the nanoparticles exposure rate and τ_n is the time constant for the nucleation. If G and τ_n are constant, the integration of the nucleation rate give simply:

$$N_0(t) = G\tau_n(1-e^{-t/\tau_n}) \qquad (3.1.7.2)$$

and if the nucleation rate is given by $N_0(t)/\tau_n$, we have:

$$I(t) = G(1-e^{-t/\tau_n}) \qquad (3.1.7.3)$$

where G is equal to I_s, the steady-state nucleation rate, as seen in par. 3.1.6.
By integrating the former equation, we obtain:

$$N(t) = G\left[(t-\tau_n) + \tau_n e^{-t/\tau_n}\right] \qquad (3.1.7.4)$$

where a constant generation rate has been assumed, that implies a reservoir of nanoparticles during the reaction. Let's now consider CNTs' nucleation and growth. This is expected to be a complex process made up of several steps. The main stages should be: CH_4 chemisorption, bond activation and rupture and nucleus build-up by addition of C atoms, i.e. the polyine ring stabilized by interaction with the catalyst surface. We consider the ratio between nuclei and nanoparticles as 1:1. The rate of fractional coverage of catalyst particle surface by CH_4 and C atoms is given respectively by:

$$\frac{d\theta_{CH_4}}{dt} = J(1-\theta_C-\theta_{CH_4}-\theta_p) - K_R\theta_{CH_4} \qquad (3.1.7.5)$$

$$\frac{d\theta_C}{dt} = K_R\theta_{CH_4} - \left(\frac{d\theta_C}{dt}\right)_g \qquad (3.1.7.6)$$

where J is the effective methane flow on the particle and θ_{CH_4} is its fractional coverage, θ_C the carbon coverage, K_R the constant for methane decomposition, θ_p a term that takes into account the deactivation processes of the active sites due to poisoning and/or shield effects due to the growing CNT and/or decreasing of the nanoparticle surface sites due to progressive enlargement of CNT diameter with respect to the largest size of the nanoparticle tip. The term $-(d\theta_C/dt)_g$ considers the carbon removal by CNT growth. The θ_p term is assumed to be given by $N_p = \Omega\theta_p = \eta\left(N_{CH_4}\right)_{dec}$ where N_p is the number of active sites that have been inhibited, Ω is the number of active sites, $\left(N_{CH_4}\right)_{dec}$ is number of molecules decomposed at time t and η is a constant. η is less than one when we do not have strong poisoning conditions. The poisoning rate is:

$$\dot{\theta}_p = \eta\left(\dot{\theta}_{CH_4}\right)_{dec} = \eta K_R\theta_{CH_4} \qquad (3.1.7.7)$$

In the rate of the fractional coverage the nucleation process has not been considered and the CNT growth rate is considered linear with a relation like to $\left(\frac{d\theta_C}{dt}\right)_g = \Gamma_g \theta_C$, with Γ_g the rate constant.

Now we will try to solve the rate equations for the methane and carbon atoms coverage in two limit cases:

a) Slow methane decomposition;

b) Fast methane decomposition.

Case a)

In this case the CNT growth is fast, that implies at the steady state, $\dot{\theta}_C \cong 0$ and through eqn. *3.1.7.6*, the fractional methane coverage as:

$$\theta_{CH_4} = \Gamma_g \theta_C / K_R \qquad (3.1.7.8)$$

and the initial system of rate equations (see eqn. *3.1.7.5* and *3.1.7.6*) reduces to:

$$\ddot{\theta}_{CH_4} + (J + K_R)\dot{\theta}_{CH_4} + J\eta K_R \theta_{CH_4} = 0 \qquad (3.1.7.9)$$

the solution of which is:

$$\theta_{CH_4}(t) = \frac{J}{\alpha_1 - \alpha_2}\left(e^{\alpha_1 t} - e^{\alpha_2 t}\right) \qquad (3.1.7.10)$$

where $\alpha_1 + \alpha_2 = -(J + K_R)$ and $\alpha_1 \alpha_2 = J\eta K_R$ with α_1 and α_2 lower than zero. $\theta_C(t)$ can be derived directly by eqn. *3.1.7.8* and *3.1.7.10*.

Case b)

In this case the fast process considered is the CH_4 decomposition, so $\dot{\theta}_{CH_4} \cong 0$ and, through eqn. *3.1.7.5*:

$$\theta_{CH_4} = \frac{J(1 - \theta_C - \theta_p)}{J + K_R} \qquad (3.1.7.11)$$

The rate equation for C coverage is now (see eqn. *3.1.7.6*):

$$\dot{\theta}_C = \frac{K_R}{J + K_R}\left[J(1 - \theta_C - \theta_p)\right] - \Gamma_g \theta_C \qquad (3.1.7.12)$$

and its derivative is:

$$\ddot{\theta}_C = -\frac{K_R J(\dot{\theta}_C + \dot{\theta}_p)}{J + K_R} - \Gamma_g \dot{\theta}_C \qquad (3.1.7.13)$$

Using eqn. *3.1.7.6* and *3.1.7.7*, the poisoning rate is:

$$\dot{\theta}_p = \eta K_R \theta_{CH_4} = \eta\left(\dot{\theta}_C + \Gamma_g \theta_C\right) \qquad (3.1.7.14)$$

The substitution of the above equation into eqn. *3.1.7.13* and rearranging gives:

$$\ddot{\theta}_C + RJ\left[(1+\eta)+\Gamma_g\right]\dot{\theta}_C + J\eta\Gamma_g\theta_C = 0 \qquad (3.1.7.15)$$

where $R = K_R/(J+K_R)$. The solution is:

$$\theta_C(t) = \frac{J}{\alpha_1-\alpha_2}\left(e^{\alpha_1 t} - e^{\alpha_2 t}\right) \qquad (3.1.7.16)$$

In this case $\alpha_1+\alpha_2 = -\left[RJ(1+\eta)+\Gamma_g\right]$ and $\alpha_1\alpha_2 = J\eta\Gamma_g$. The fast decomposition implies $K_R >> \Gamma_g$ (see eqn. *3.1.7.5* and *3.1.7.6*) so $\alpha_1 = -J\eta\Gamma_g/\left(RJ(1+\eta)+\Gamma_g\right)$ and $\alpha_2 = -\left(RJ(1+\eta)+\Gamma_g\right)$. For both the cases a) and b), the growth rate of CNTs can be related to the carbon coverage by relation:

$$\dot{l} = \frac{\Omega}{\rho'}\left(\dot{\theta}_C\right)_g = \frac{\Omega}{\rho'}\Gamma_g\theta_C \qquad (3.1.7.17)$$

where Ω is the number of active sites per particle and ρ' the number of C atoms per length unit (linear density). In both cases $\theta_C \to 0$ and, consequently, $\left(\frac{d\theta_C}{dt}\right)_g \propto \frac{dl}{dt} \to 0$, and this is a physical explanation of the steady state reaction rate. Γ_g should be of the form $\Gamma_g \propto \frac{(R_n/a)}{\Omega}\frac{D}{a^2}$ where R_n is the radius of the CNT nucleus, D is the surface diffusion coefficient of C atoms and a^2 the area of the adsorption site. This model allows for the calculation of the production rate of carbon atoms considering the role of the nanoparticle generation. Because the CH_4 decomposition starts when the particle is exposed to the gas stream, the rate can be written as:

$$R_C = m_C\Omega G K_R\int_0^t \theta_{CH_4}(\xi)d\xi \qquad (3.1.7.18)$$

with m_C the mass of a C atom. Now, considering the cases a) and b), θ_{CH_4} is, respectively, given in eqn. *3.1.7.10*, and, according to eqn. *3.1.7.6*, $\theta_{CH_4} = \left(\dot{\theta}_C + \Gamma_g\theta_C\right)/K_R$. By inserting this relation in the expression of R_c, we have:

$$R_C = m_C\Omega G K_R\left[\theta_C(t) + \Gamma_g\int_0^t \theta_C(\xi)d\xi\right] \qquad (3.1.7.19).$$

For case a):

$$R_C = m_C \Omega G K_R \frac{J}{\alpha_1 \alpha_2}\left\{\frac{\alpha_2}{\alpha_1-\alpha_2}e^{\alpha_1 t} - \frac{\alpha_1}{\alpha_1-\alpha_2}e^{\alpha_2 t} + 1\right\} = \frac{m_C \Omega G}{\eta}\left\{\frac{\alpha_2}{\alpha_1-\alpha_2}e^{\alpha_1 t} - \frac{\alpha_1}{\alpha_1-\alpha_2}e^{\alpha_2 t} + 1\right\} \qquad (3.1.7.20)$$

with the steady state value $R_C(\infty) = m_C \Omega G / \eta$, and for case b):

$$R_C = m_C \Omega G\left\{\frac{J}{\alpha_1-\alpha_2}e^{\alpha_1 t}\left(1+\frac{\Gamma_g \alpha_2}{\alpha_1 \alpha_2}\right) - \frac{J}{\alpha_1-\alpha_2}e^{\alpha_2 t}\left(1+\frac{\Gamma_g \alpha_1}{\alpha_1 \alpha_2}\right) + \frac{\Gamma_g J}{\alpha_1 \alpha_2}\right\} \qquad (3.1.7.21).$$

The steady state value of case b) is the same as for case a).

For evaluating the CNT production rate and considering eqn. *3.1.6.3*, assuming also a constant nucleation rate *G*, we have that:

$$\dot{M} = \rho G l(t) \qquad (3.1.7.22)$$

with $\rho = \rho' m_C$. Using eqn. *3.1.7.17* in this last relation, the equation below is obtained:

$$\dot{M} = m_C G \Omega \int_0^t \theta_C(t')dt' \qquad (3.1.7.23)$$

For case a) $\dot{M}$ is equal to R_C and that is quite obvious because of the fast C atom removal by the growing CNT. Otherwise, for case b) $\dot{M}$ cannot be equal to R_C because of the delay between C atom production and its removal by the growing CNT. Anyway, in steady state conditions, $R_C = \dot{M}$, because $\dot{\theta}_C(\infty) = 0$ due to the nanoparticle poisoning. The α_1 and α_2 expressions reported above show that for the cases here considered, under reasonable assumptions, one of them should be always lower than the other. In fact in case a) $K_R << \Gamma_g$ and assuming $J > K_R$ we get $\alpha_1 \cong -\eta K_R$, $\alpha_1 >> \alpha_2 \cong -J$ ($\eta < 1$). As a consequence,

$$R_C \cong \frac{m_C \Omega G}{\eta}(1 - e^{\alpha_1 t}) \qquad (3.1.7.24).$$

In case b) ($K_R >> \Gamma_g$) one assumes that also $J > \Gamma_g$ and $K_R > J$ (i.e. $R \approx 1$) which implies $\alpha_1 \cong -\eta\Gamma_g$, $\alpha_1 >> \alpha_2 \cong -J$. Under these circumstances eqn. *3.1.7.21* gives:

$$R_C = \frac{m_C \Omega G}{\eta}\left[1 - (1-\eta)e^{\alpha_1 t}\right] \qquad (3.1.7.25)$$

that becomes eqn. *3.1.7.24* in the limit $\eta << 1$. If we now consider the rate of CNTs production for case b), it is, under the same approximations made for eqn. *3.1.7.25*:

$$\dot{M} = m_C G\Omega\Gamma_g \frac{J}{\alpha_1\alpha_2}\left(1+\frac{\alpha_2}{\alpha_1-\alpha_2}e^{\alpha_1 t}-\frac{\alpha_1}{\alpha_1-\alpha_2}e^{\alpha_2 t}\right) \cong \frac{m_C G\Omega}{\eta}\left(1-e^{\alpha_1 t}\right) \qquad (3.1.7.26)$$

These two last eqn. are equal only at the steady state condition. Looking now at the growth kinetics $l(t)$, from eqn. *3.1.7.17*, we have for case a) and b) respectively:

$$l(t) = \frac{\Omega K_R J}{\rho'\alpha_1\alpha_2}\left(1+\frac{\alpha_2}{\alpha_1-\alpha_2}e^{\alpha_1 t}-\frac{\alpha_1}{\alpha_1-\alpha_2}e^{\alpha_2 t}\right) \qquad (3.1.7.27)$$

$$l(t) = \frac{\Omega\Gamma_g J}{\rho'\alpha_1\alpha_2}\left(1+\frac{\alpha_2}{\alpha_1-\alpha_2}e^{\alpha_1 t}-\frac{\alpha_1}{\alpha_1-\alpha_2}e^{\alpha_2 t}\right) \qquad (3.1.7.28)$$

and considering the approximations for α_1 and α_2, the result is:

$$l(t) = \frac{\Omega}{\rho'\eta}\left(1-e^{\alpha_1 t}\right) \qquad (3.1.7.29)$$

in which, for case a) $\alpha_1 = -\eta K_R$, and for case b) $\alpha_1 = -\eta\Gamma_g$. The comparison of eqn. *3.1.6.5* with eqn. *3.1.7.29* leads to $\tau \equiv \tau_g = \alpha_1^{-1}$ and $l_\infty = \Omega/\rho'\eta$. All this implies that the maximum length of a CNT depends by the nanoparticle dimension, by its linear density and by η. In summary, we have shown that the time constant for the conversion rate, R_C, is given by $\tau = \eta K_R$ if the CH_4 decomposition is rate determining and $\tau = \eta\Gamma_g$ if the CNT growth is rate determining. In both cases $l_\infty = \Omega/\rho'\eta$ and $\dot{M}_\infty = \rho' m_C G$.

3.1.8 Comparison with literature data

The topic related to the simultaneous CNTs and H_2 production has become of interest quite recently and for this reason the literature on the subject is quite limited works are quite few. Qian et al. [42] used a Ni/Cu bimetallic catalyst supported on Al_2O_3 for a maximum of 15 h:

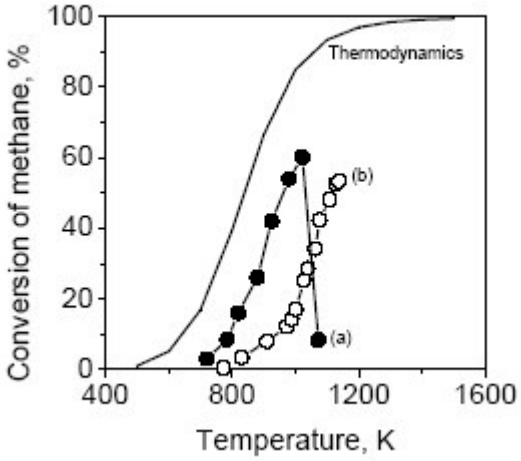

Fig. 102

Two different type of reactors were used in this work: a single stage (black dots) and a two-stage (white dots). Wang and Baker [43] also used a Ni/Cu bimetallic catalyst, but supported on MgO:

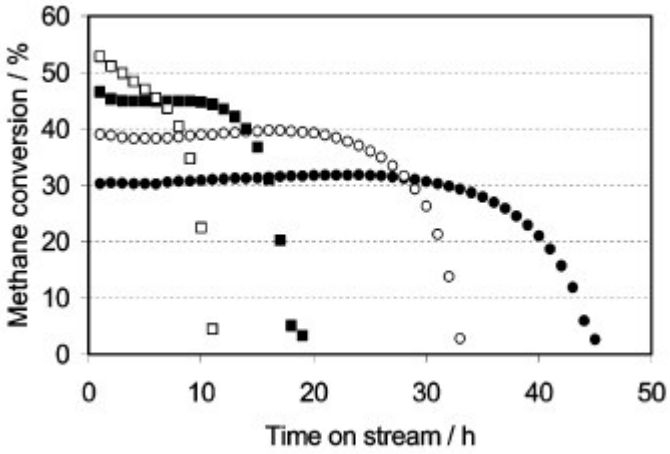

Fig. 103

The different curves refer to different temperatures:

- white squares 665 °C;
- black squares 700 °C;
- white dots 725 °C;
- black dots 750 °C.

Takenaka and al. [44] used SiO_2 supported Ni catalyst also with the addition of a second metal, and a bimetallic Ni/Pd catalyst supported on different materials; all the experiments were performed at 500 °C:

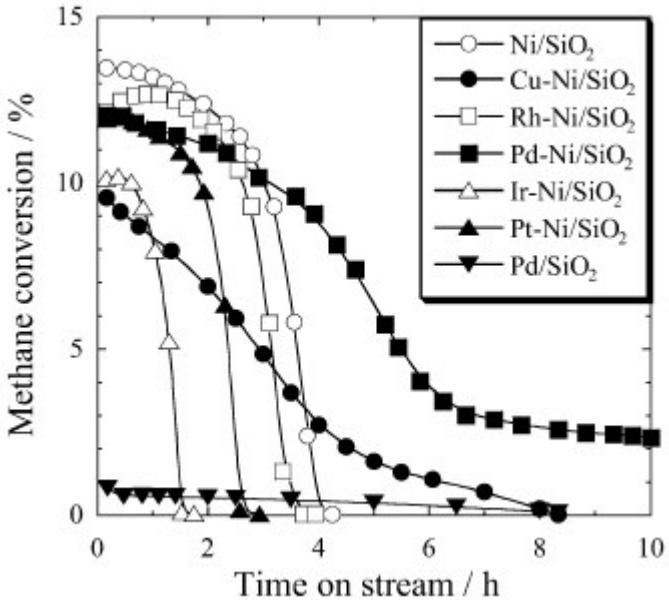

Fig. 104

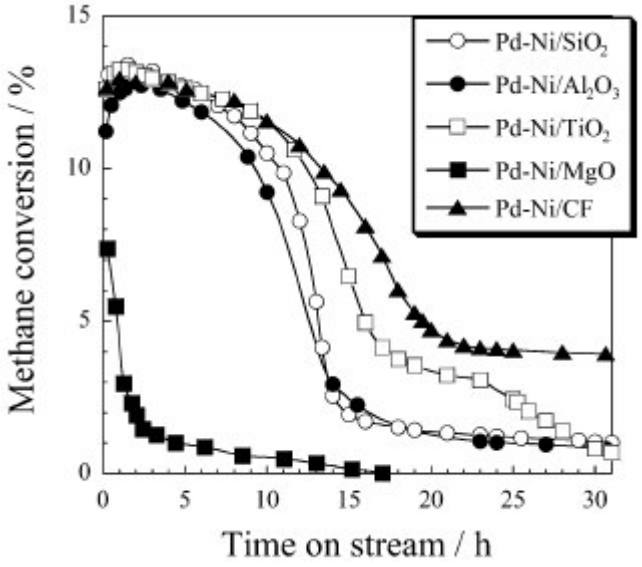

Fig. 105

CF refers to carbon fibers. The quick poisoning of all the catalysts is evident.

Li et al. [45] performed their experiments by using Nb_2O_5 supported Ni catalysts at 500 °C:

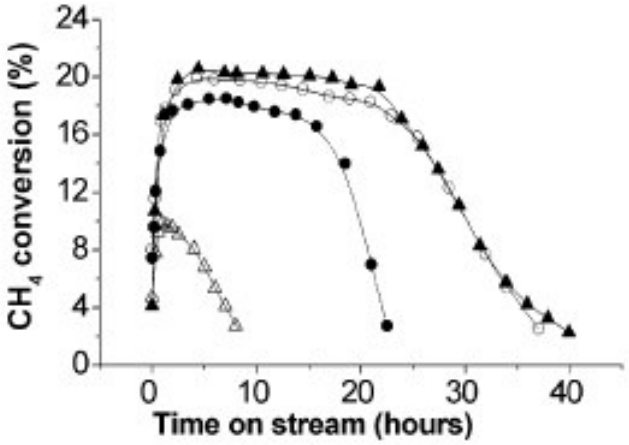

Fig. 106

In this case, each curve refers to a catalyst with different Ni content:

- black triangles 5% Ni;
- black dots 12% Ni;
- white dots 19% Ni;
- white triangles 32% Ni.

In all the cases the conversion does not exceed 20% and the poisoning time 40 h.

They also tested Nb_2O_5 supported bimetallic Ni/Cu at various temperatures with the results reported in fig. 107:

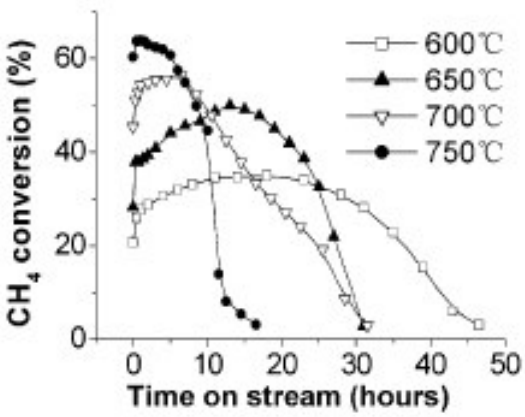

Fig. 107

Also in this case, though the authors obtained higher conversion values than before, the catalyst lifetime is quite limited.

Finally, Reshetenko et al. [46] tested Al_2O_3 supported Fe and bimetallic Fe/Co and Fe/Ni at 625 °C obtaining the results given in fig. 108:

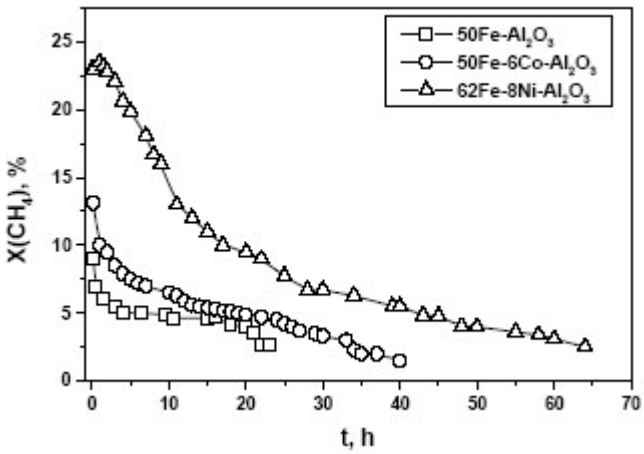

Fig. 108

In all the cases, carbon was formed as MWCNTs. A direct comparison between the results presented in this work and the results in literature cannot be exhaustive especially concerning the conversion data. This, due to the different experimental conditions used (temperature, flow rate, type of reactor, etc.). Anyway, one point has to be remarked: in all the literature works, the catalyst has a limited life, while in our case, for T<575 °C, no poisoning of the catalyst has been detected.

3.2 Growth of the ceramic phosphor thin films

3.2.1 Choice of the oxide hosts

In order to choice the best oxide host, it is necessary to take into consideration various properties, both chemical and physical ones. From a chemical point of view, high thermodynamic stability and lack of reactivity should be the essential requirements; from a physical point of view, the requisites should be low vapour pressures, high melting points, no luminescent transitions in the visible range and low phonon energy (see expression *1.8.1*). By considering all these factors, the choice possibility is not wide because only oxides of Sc, Y, Gd, Lu, Zr and Hf satisfy all the requisites shown above (tab. 4).

Formula	ΔG^0_f(298 K) kJ/mol O_2	Vapour pressure at 298 K Pa	Melting point K
Sc_2O_3	-1212.7	-	2762
Y_2O_3	-1210.8	-	2712
Gd_2O_3	-1168.4	-	2698
Lu_2O_3	-1192.7	-	2763
ZrO_2	-1042.5	10^{-121}	2983
HfO_2	-1059.2	10^{-142}	3073

Tab. 4

Actually also Th oxide could be considered but its natural radioactivity requires several precautions which make the use troublesome. For its exceedingly high cost, also Lu oxide was discarded. Considering that from a chemical point of view there is no particular reason to prefer one candidate instead of another one in the above list, the only discriminating factor is the maximum phonon energy. So they were examined by diffuse reflectance IR spectroscopy in order to establish their phononic behaviour:

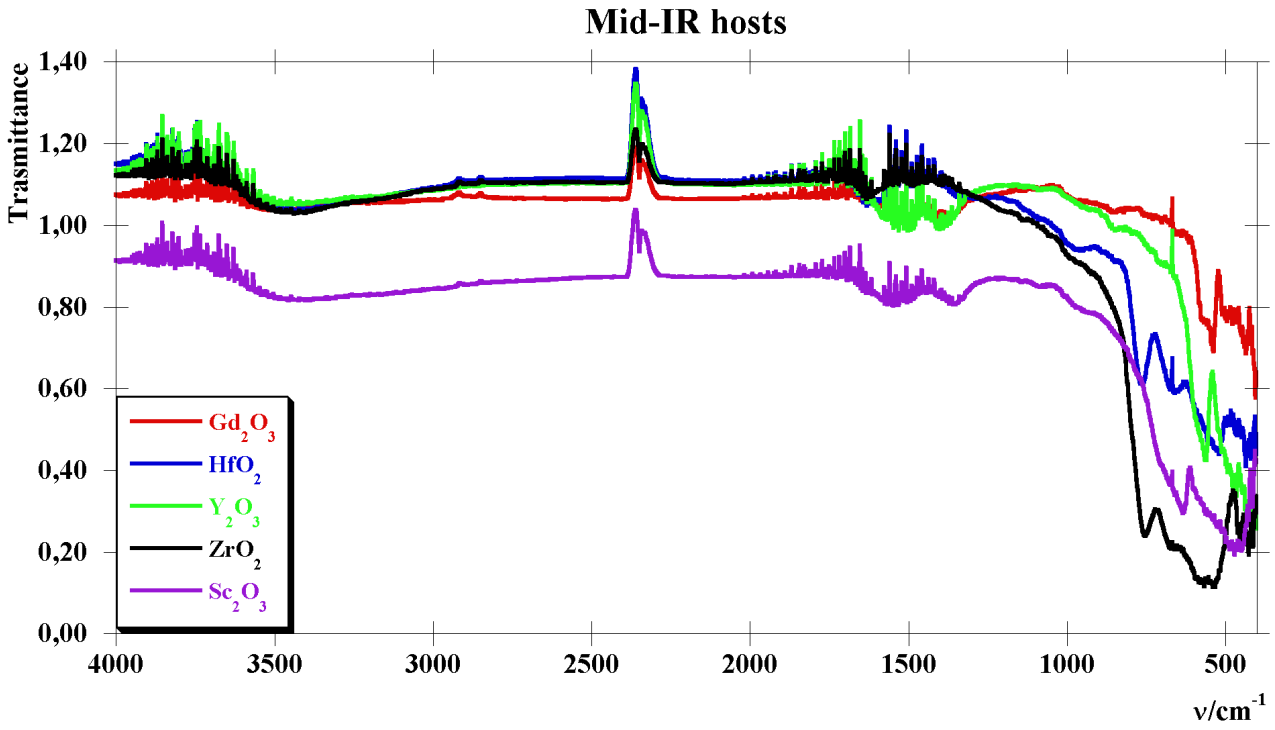

Fig. 109

From the spectra it is evident that Y_2O_3 and Gd_2O_3 are the best candidates, having their highest phonon energy at ~560 and ~540 cm^{-1} respectively (see par. 1.8). So our research was focused on doped thin films of these two oxides.

3.2.2 Comparison between Y_2O_3 and Gd_2O_3 films: results and discussion

In tab. 5 the EDS results for each host-dopant couple (dopant/host atomic % ratio) and thickness of the films are reported:

H	D	Eu_2O_3 *Red*	thickness /µm	Tb_2O_3 *Green*	thickness /µm	Tm_2O_3 *Blue*	thickness /µm
Y_2O_3		0.9	1.01	2.7	1.01	1.9	1.01
		3.2	1.00	4.1	1.01	2.7	1.00
		8.4	0.99	8.4	1.00	9.8	0.99
Gd_2O_3		4.2	0.97	2.6	1.01	1.6	1.01
		5.0	1.01	5.7	1.00	3.4	1.01
		9.4	0.99	8.2	1.00	7.6	0.99

Tab. 5

while in figg. 110-112 the CL spectra are shown:

By looking at these spectra it is clearly evident that yttria-based films are always more efficient than gadolinia-based ones. Obviously, this consideration is done considering films having similar host to dopant ratios. In Eu-doped samples, for example, the most intense CL peak ($^5D_0 \rightarrow ^7F_2$) is always more intense for Y_2O_3 than Gd_2O_3. For the sample with Eu/Y ratio equal to 3.2% the photomultiplier underwent to saturation, so the real intensity of the peak was much higher than that shown in fig. 110. These findings agree with the literature results [33] for PLAD deposited Eu-doped Gd_2O_3 films on fused silica substrates, the same used in the present work. XRD spectra for Gd_2O_3 and Y_2O_3 films (fig. 114-116) belong as expected, respectively to the monoclinic phase and to the cubic system. Gd_2O_3 and Y_2O_3 possess the same crystal structures, i.e. cubic and monoclinic. The monoclinic phase for Gd_2O_3 is reported to be stable at high temperature (650 °C) and low oxygen partial pressure ($2x10^{-5}$ mbar) [33]. Looking at the growth conditions used in our experiments (substrate temperature 800 °C, total pressure in the deposition chamber ~10^{-5} mbar), these results are not surprising. A more exhaustive discussion on XRD spectra will be given later on; anyway, this first observation is very important as it shades light why the lower luminance of gadolinia films. It is well known that monoclinic structure has considerably lower luminescence efficiency than the cubic one [47]. Furthermore, the intensity ratio $\frac{^5D_0 \rightarrow ^7F_2}{^5D_0 \rightarrow ^7F_1}$ between the two Eu^{3+} transitions (see tab. 6) is always higher for samples with Y_2O_3. Higher this ratio, higher is the quality of the phosphor as red emitter.

Dopant: Host	Radiative transitions							Band intensity ratio
	Eu^{3+}		Tb^{3+}				Tm^{3+}	
	$^5D_0 \rightarrow {}^7F_1$ nm	$^5D_0 \rightarrow {}^7F_2$ nm	$^5D_4 \rightarrow {}^7F_6$ nm	$^5D_4 \rightarrow {}^7F_5$ nm	$^5D_4 \rightarrow {}^7F_4$ nm	$^5D_4 \rightarrow {}^7F_3$ nm	$^1G_4 \rightarrow {}^3H_6$ nm	
$Eu:Y_2O_3$	579-604	605-635						$\frac{^5D_0 \rightarrow {}^7F_2}{^5D_0 \rightarrow {}^7F_1} > 2.8^*$
$Tb:Y_2O_3$			476-518	525-575	575-605	612-636		$\frac{^5D_4 \rightarrow {}^7F_5}{^5D_4 \rightarrow {}^7F_6} = 2.6$ $\frac{^5D_4 \rightarrow {}^7F_5}{^5D_4 \rightarrow {}^7F_4} = 5.8$ $\frac{^5D_4 \rightarrow {}^7F_5}{^5D_4 \rightarrow {}^7F_3} = 14$
$Tm:Y_2O_3$							443-500	
$Eu:Gd_2O_3$	575-605	605-644						$\frac{^5D_0 \rightarrow {}^7F_2}{^5D_0 \rightarrow {}^7F_1} = 4.1$
$Tb:Gd_2O_3$			480-512	533-564	576-604	614-634		$\frac{^5D_4 \rightarrow {}^7F_5}{^5D_4 \rightarrow {}^7F_6} = 4.0$ $\frac{^5D_4 \rightarrow {}^7F_5}{^5D_4 \rightarrow {}^7F_4} = 5.9$ $\frac{^5D_4 \rightarrow {}^7F_5}{^5D_4 \rightarrow {}^7F_3} = 7.3$
$Tm:Gd_2O_3$	-	-	-	-	-	-	-	-

*Photomultiplier saturation

Tab. 6

In the monoclinic structure, the cations can be positioned in three different sites of symmetry C_s. In this structure the low energy side of the $^5D_0 \rightarrow {}^7F_2$ transition (>620 nm) becomes more important [33], up to reach an intensity comparable with the high energy side, decreasing the color purity of the phosphor. On the contrary, the cubic structure has two different cationic sites with symmetries S_6 and C_2. The former is not important for the emission properties because of the strict inversion symmetry whereas the latter gives (Y_2O_3 case) a sharp predominant emission peak at about 611 nm. The CL spectra were carried also on pure hosts' films in order to check eventual presence of luminescent-active impurities: the spectrum of the Y_2O_3 undoped film shows that no CL active species are present in whereas Tb^{3+} emission lines can be seen in the Gd_2O_3 film. Considering now the Tm^{3+}-doped gadolinia films, it is immediately evident that no Tm^{3+} emission lines are present,

but only those belonging to the Tb^{3+} impurities; magnifications of the Tb^{3+} emission lines are given in the inserts in fig. . This behavior can be explained considering the structure of the energy levels of the Tm^{3+} ion (see Dieke's diagram, fig. 17): the emitting level $^1G_4$ has a very near lower level ($^3F_2$, ~7000 cm^{-1}) that intrinsically enhances nonradiative relaxation; this is coupled with the low crystallinity of the films, that stimulates nonradiative transitions by trapping energy in crystal defects. This structural disorder is probably produced by insertion of a cubic order (Tm_2O_3) into the monoclinic structure of Gd_2O_3, as discussed later on. A concentration quenching phenomenon could also be considered, but this does not agree with observations made on Tm^{3+}:Y_2O_3 films, that clearly exhibit the characteristic $^1G_4 \rightarrow {}^3H_6$ emission of the Tm^{3+} ion at similar dopant concentration. Literature data regarding spray pyrolysis deposited Tm^{3+}:Y_2O_3 films [34] demonstrated that the blue emission intensity reaches its maximum with a Tm^{3+}concentration of 0.5 at. % and that the emission intensity decreases very rapidly with increasing Tm^{3+} concentration. This phenomenon is confirmed for our Tm^{3+}:Y_2O_3 films, as the $^1G_4 \rightarrow {}^3H_6$ emission intensity decreases with increasing Tm^{3+} content. Considering now the CL spectra of Tb^{3+}-doped films, the situation is similar to the Eu^{3+}-doped ones with yttria based films. Contrarily to the Eu^{3+}-doped film, it is possible to observe an enhancement of the low energy side of the most intense Tb^{3+} transition ($^5D_4 \rightarrow {}^7F_5$). Let's now consider the chromaticity measurements on both Y_2O_3 and Gd_2O_3 films. The color coordinate diagram is shown in fig. 113:

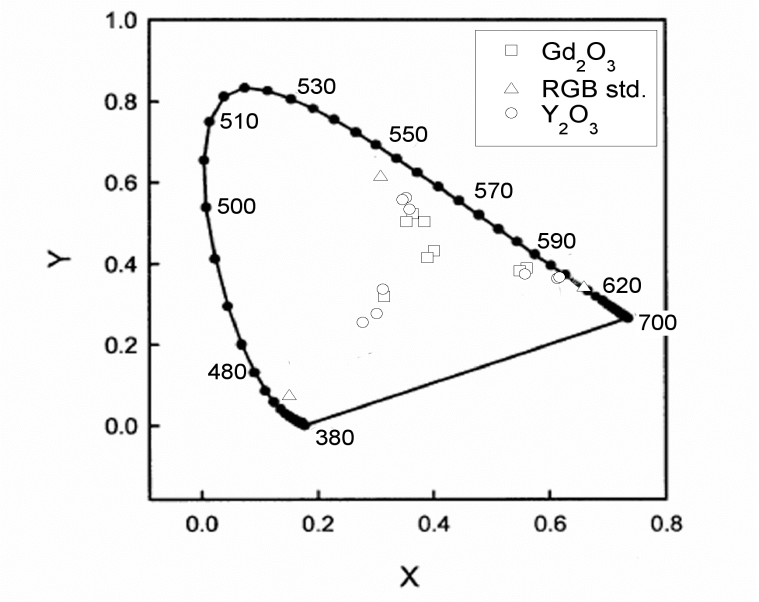

Fig. 113

This is a CIE (International Commission on Illumination) plot in which the RGB standard colors (Red=Eu^{3+}:Y_2O_2S, λ=700nm, x=0.659:y=0.331; Green=Cu^{2+}:ZnS, λ=546.1nm, x=0.304:y=0.608; Blue=Ag^{+}:ZnS; λ=453.8, x=0.145:y=0.059) are also reported together to our samples. It is immediately evident that yttria possess color coordinates closer to those of the standard samples. According to the CIE plot [48], the average value of the red film coordinates falls within the area of orange, the average value of the green film coordinates falls within the area of yellowish green and the average value of the blue film coordinates falls within the area of purplish pink. Gd_2O_3-based films have color coordinates that deviate more evidently from the standards' ones. This deviation can be attributed to the structure disorder increase in Gd_2O_3 monoclinic structure due to the cubic doping as discussed later on. The enhancement of the nonradiative transitions that are related to the decrease of the ratio between the most intense transitions and the secondary ones thus causing a loss of color quality. The XRD analysis of all the samples studied is reported in figg. 114-116.

	HOST				DOPANT					
	Gd_2O_3		**Y_2O_3**		**Eu_2O_3**		**Tb_2O_3**		**Tm_2O_3**	
JCPDS no.	43-1015		82-2415		34-0392		23-1418		41-1090	
system: lattice: space group: cell (a;b;c) /pm:	Monoclinic End-centered C2/m(12) 14.06;3.57;8.76		Cubic Body-centered Ia$\underline{3}$(206) 10.60;0;0		Cubic Body-centered Ia$\underline{3}$(206) 10.86;0;0		Cubic Body-centered Ia3(206) 10.73;0;0		Cubic Body-centered Ia3(206) 10.48;0;0	
intensity	2θ /°	h k l	2θ /°	h k l	2θ /°	h k l	2θ /°	h k l	2θ /°	h k l
1st	32.472[I]	$\underline{1}$ 1 2	29.155[I]	2 2 2	28.421	2 2 2	28.803	2 2 2	29.474	2 2 2
2nd	*30.115*	*$\underline{4}$ 0 2*	48.536[IV]	4 4 0	47.266	4 4 0	47.925	4 4 0	49.098	4 4 0
3rd	31.680[III]	3 1 0	33.790	4 0 0	32.926	4 0 0	56.866	6 2 2	34.155	4 0 0
4th	28.235[II]	1 1 1	57.625[II]	6 2 2	56.077	6 2 2	33.381	4 0 0	58.311	6 2 2
5th	*29.425*	*4 0 1*	20.503	2 1 1	76.312	6 6 2	77.480	6 6 2	20.712	2 1 1
6th	*31.081*	*0 0 3*	43.490[V]	1 3 4	42.362	4 3 1				
7th	47.470[VII]	3 1 3	78.602	6 6 2	78.678	8 4 0				
8th	42.380[IV]	$\underline{3}$ 1 3	39.849[VII]	3 3 2	51.809	6 1 1				
9th	53.969	$\underline{7}$ 1 2	59.046[VI]	1 3 6	57.453	6 3 1				
10th	55.743	*	35.908	4 1 1	61.473	6 4 0				
11th	51.191[V]	0 2 0	53.215	6 1 1						
12th	60.580	7 1 2	60.447	4 4 4						
13th	61.088	**	56.181[III]	1 4 5						
14th	60.149[VI]	4 2 1	81.061[III]	0 4 8						

Superscript roman numbers refer to the intensity order found in the spectra of the pure host films reported in Figs. 114-116.

Features lacking in the experimental spectra are reported in italic.

*Multiple features: 0 2 2;7 1 1

**Multiple features: 1 1 5; 8 0 2;0 2 3;$\underline{6}$ 0 5

Tab. 7

These spectra contain several interesting features:

a. Spectrum of pure Gd_2O_3 film. The spectrum of this film doesn't match exactly with reference spectrum, as shown in tab.. The reflections belonging to the planes ($\underline{4}02$), (401) and (003) are not present (reported in italic on tab. 7) and the intensity order doesn't fit very well the reference pattern (superscript roman numbers in tab. 7). This is probably due to a certain degree of preferential orientation of the film. Furthermore, no cubic phase can be detected from the XRD pattern. Even if the film diffraction pattern does not exactly coincide to the ICDD table, the literature data mentioned before [33] support the monoclinic structure, considering the experimental conditions in which the film was grown.

b. In Eu^{3+}-doped Gd_2O_3 films (fig. 114), the only changes in the diffraction patterns occur only to the relative intensities of the reflections. In the diffractogram referring to the film with the highest Eu^{3+} concentration , i.e. Eu/Gd 9.4%, the reflection of the plane ($\underline{4}02$) appears, but the whole spectrum indicates that the sample is less crystalline than the pure Gd_2O_3 sample. A reasonable explanation of this can be found considering that the high concentration of Eu^{3+} tends to destroy the monoclinic structure (Eu_2O_3 is cubic) even if no trace of features of a cubic structure appears, neither from cubic Gd_2O_3 nor Eu_2O_3.

c. The XRD spectra of Gd_2O_3 films doped with Tb^{3+} and Tm^{3+} are similar to those of the Eu^{3+} doped films. Gd_2O_3 based films show all the same behavior with increasing dopant concentration, i.e., variation of the relative intensities of the diffraction lines; Similarly to Eu^{3+} doped films, at the highest dopant concentration the films show a substantial decrease of crystallinity, but for Tb^{3+} and Tm^{3+} doped films this feature is more pronounced than in the Eu^{3+} doped one.

d. In the pure Y_2O_3 film diffraction pattern, the reflections were found in the expected positions, but not the intensity order, with the exception of the (222) line, that is the most intense as expected. The paper of Zhang et al. [49] deals with PLAD deposited Y_2O_3 films found on fused silica substrate at 10^{-5} mbar and 650 °C and these films showed only the (222) reflection. They observed also that by increasing the pO_2 values during the film growth, more lines other than (222) appeared. This behavior was attributed to a decrease of the oxygen vacancy concentration as pO_2 was increased. The structure of cubic Y_2O_3 (bixbyte-type) tend to accommodate oxygen vacancies ordered along the (222) direction because of the favorable surface energy, thus leading to a preferred growth in the (222) orientation.

e. A situation similar to that of pure Y_2O_3 film occurs in the case of Eu^{3+} and Tb^{3+} doped yttria films, with the same substrate temperature and chamber pressure. This is not true for the Tm^{3+} doped film. This behavior can be explained considering the different ionic sizes of the dopant ions in comparison with yttrium ion, and so the possibility of accommodating oxygen vacancies. The substitution of Y^{3+} with another trivalent ion can lead to expansion or shrinkage of yttria structure, depending from the dopant ion size with respect to the size of Y^{3+}. The ionic radius sequence, given in Å is: Eu^{3+} 0.947 > Tb^{3+} 0.923 > Y^{3+} 0.900 > Tm^{3+} 0.880. So only Eu^{3+} and Tb^{3+} can cause the expansion of Y_2O_3 lattice. Considering that oxygen vacancies cause a lattice expansion, the doping of Y_2O_3 with Tb^{3+} or Eu^{3+} can allow to accommodate more oxygen vacancies in the crystal lattice in the same film growth conditions. But the situation changes in the case of Tm^{3+}: this ion is smaller than Y^{3+}, and so the insertion of the Tm^{3+} ion in the yttria structure leads to its shrinkage. In this way, the increase of the oxygen vacancies is no more allowed, but probably their concentration should decrease.

f. The diffractogram referring to the Eu^{3+}:Y_2O_3 film with highest Eu^{3+} concentration seem to support the arguments above. In fact the second most intense reflection at $2\theta = 52.08°$ belongs clearly to cubic Eu_2O_3, crystallographic plane (611), but it is shifted towards higher 2θ values, because the actual value for pure Eu_2O_3 is 51.809°. On the contrary, looking at the main reflection of Y_2O_3, that is magnified in the insert, it is shifted of 0.1° toward lower 2θ values. So two phenomena occur at the same time: Y_2O_3 lattice is detectably expanded, while Eu_2O_3 lattice is shrunk. This process could be better represented if the reaction below is considered:

$$Y_2O_3 + Eu_2O_3 = Y_{2-x}Eu_xO_{3-x} + Eu_{2-x}Y_xO_3 + x/2\ O_2(g)$$

that is favored at low pO_2.

In figg. 117-119 the SEM photos of the samples are displayed.

The SEM images show clearly that in all the cases very compact, non-porous films have been grown. Nanostructures are not present in all the Gd_2O_3 films, while in Y_2O_3 films polygonal nanocrystals are evident in all the Tb^{3+} doped samples and in the 3.2 and 0.9% Eu^{3+} doped ones. These features strongly support the evidence of a preferential growth direction in the case of Y_2O_3 films for Tb^{3+} doped samples and also for two of the Eu^{3+} doped samples (Eu/Y=3.2 and 0.9%). The octahedral shape of the nanocrystals suggest the exposition of the (222) faces, as the XRD patterns. Also HR-TEM analysis of the Eu/Y=3.2% sample shows a strong (222) preferential orientation of the film:

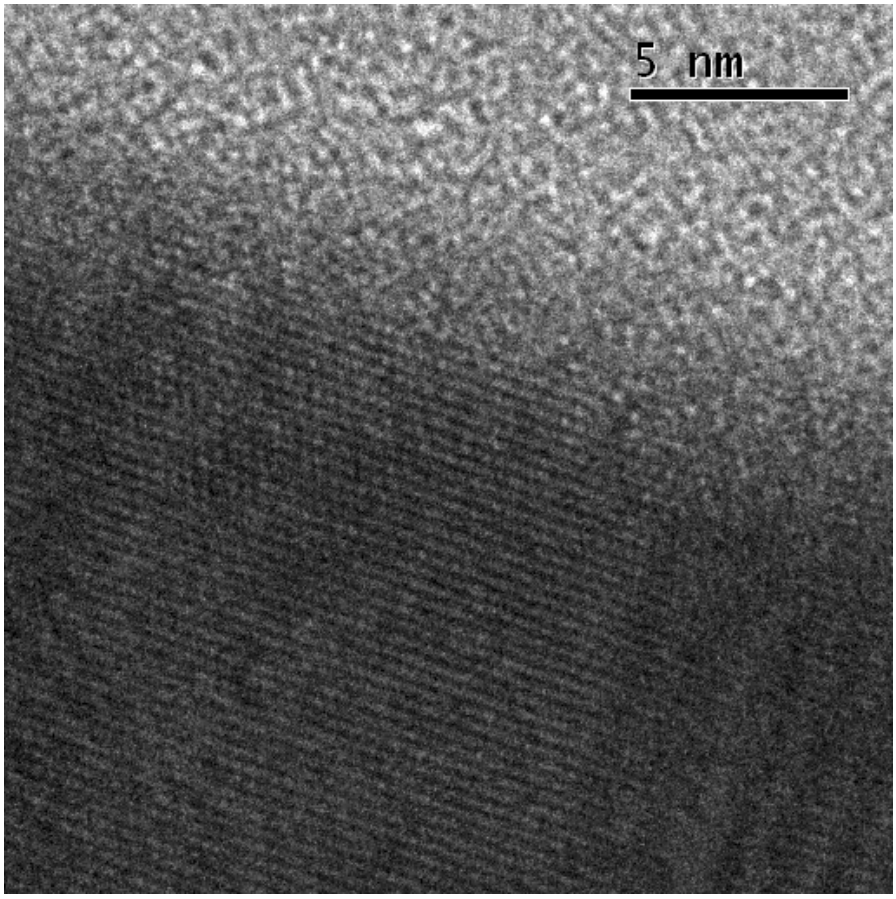

Fig. 120

By making the Fourier transform (FFT) of this image we obtain the following image:

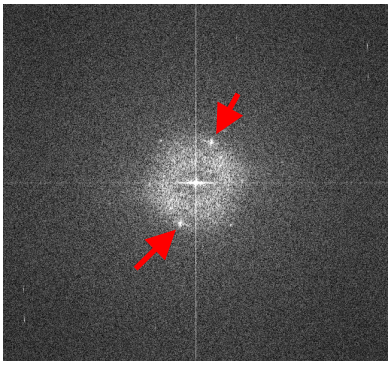

Fig. 121

Using the most intense spots indicated by the red arrows for filtering the previous HR-TEM image, we have:

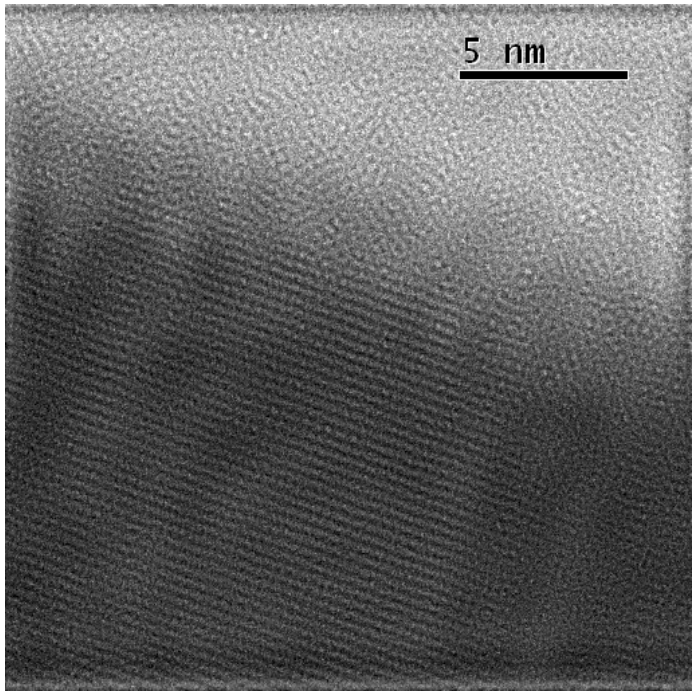

Fig. 122

The darker zone in both non-filtered and filtered HR-TEM images correspond to the film, while the brighter zone to the substrate. By checking the interplanar distances in the filtered zone in which only the families of crystallographic planes corresponding to the two spots selected in FFT image, a distance of 3.01±0.05 Å is obtained, that corresponds exactly to the (222) planes spacing. This feature is more evident in the following filtered picture taken near the surface of the film:

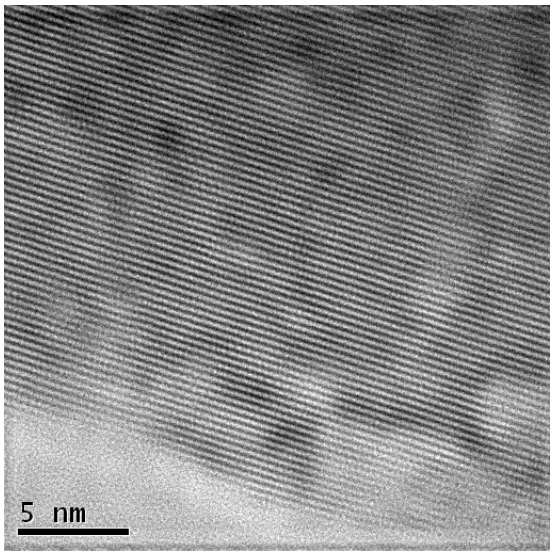

Fig. 123

A final consideration should be done for the SEM image of the Eu/Y=8.4% film: the disordered morphological structure of the film agrees well with the expectations from the XRD pattern, in which two phases emerge together to the absence of any preferential orientation of the film growth.
Up to now, a direct comparison of our results with literature data is not possible, considering that measurements of absolute luminous efficiency have to be performed.

4. Conclusions

At first glance, both the fields treated in the present work could appear not reciprocally related though they have an intrinsic common point: the nanostructures. In fact, the EB-PVD films should be considered nanostructured materials especially at the beginning of their growth and, depending on the experimental conditions, they can maintain their nanosizes or evolve to larger sizes, i.e., microsizes. The MWCNTs, of course, grow at once at nanosize scale and they maintain it at least in one direction without loosing the nanostructure features, even under different experimental conditions. Under this point of view, the present work deals with the synthesis and characterization of two classes of nanostructured materials.

Therefore, concerning the CNTs growth and H_2 production we can say that:

- a new and environmentally friendly method for producing H_2 has been presented;
- the catalyst used is unique in its behaviour and its process of self-nanostructuring during the methane decomposition is interesting also from a fundamental point of view;
- carbon produced in the reaction is a valuable by-product, as it is 100% CNTs in the temperature range in which the catalyst does not poison;
- a complete characterization of the reaction products has been performed by using the most powerful techniques available today;
- an hypothesis of reaction mechanism together with both a phenomenological and a physical model have been presented.

Further research is needed for the following topics:

- the mechanism of formation of catalyst nanoparticles from micrometric particles, but this is particularly difficult, considering that the only technique suitable to study directly at nanometric scale solid-gas reactions is environmental TEM (few units worldwide);
- the rate limiting step of the reaction is not clear;
- a lot of TEM measurements are still needed to test the validity of the theoretical reaction models developed.

For the topic regarding the cathodoluminescent ceramic films, the considerations are:

- efficient hosts and dopant ions for obtaining high luminescence efficiency have been found;
- an effective simple and cost-effective way to have films with a controllable amount of dopant has been developed;
- a deep structural, morphological and spectroscopic characterization of the samples has been performed;
- the best host between the two chosen has been pointed out.

Necessary improvements for this research are:

- a more detailed study of the effect of dopant concentration on luminescence efficiency;
- measurements of absolute luminous efficiency are needed;
- XANES measurements on the samples in order to know the amount of active dopant ions (i.e. located in non-centrosymmetric sites) present.

5. References

[1] Buffat, P.; Borel, J. P., *Phys. Rev. A* (1976), **13**(6), 2287-98.

[2] Haruta, M.; Kobayashi, T.; Sano, H.; Yamada, N., *Chem. Lett.* (1987), **2**, 405-8.

[3] Chiesa, P.; Consonni, S.; Kreutz, T.; Williams, R., *Int. J. Hydrog. Energy* (2005), **30**(7), 747-767.

[4] Iijima, S., *Nature* (1991), **354**(6348), 56-8.

[5] Davis, W. R.; Slawson, R. J.; Rigby, G. R., *Nature* (1953), **171**, 756.

[6] Yu, Z.; Chen, D.; Totdal, B.; Holmen, A., *Catal. Today* (2005), **100**(3-4), 261-267.

[7] Guo, T.; Nikolaev, P.; Thess, A.; Colbert, D. T.; Smalley, R. E., *Chem. Phys. Lett.* (1995), **243**(1,2), 49-54.

[8] Reshetenko, T. V.; Avdeeva, L. B.; Ushakov, V. A.; Moroz, E. M.; Shmakov, A. N.; Kriventsov, V. V.; Kochubey, D. I.; Pavlyukhin, Yu. T.; Chuvilin, A. L.; Ismagilov, Z. R., *Appl. Catal. A-Gen.* (2004), **270**(1-2), 87-99.

[9] Hernadi, K.; Fonseca, A.; Nagy, J. B.; Siska, A.; Kiricsi, I., *Appl. Catal. A-Gen.* (2000), **199**(2), 245-255.

[10] Dresselhaus, M. S.; Dresselhaus, G.; Saito, R., *Carbon* (1995), **33**(7), 883-91.

[11] Iijima, S., *Mater. Sci. Eng. B-Solid State Mater. Adv. Technol.* (1993), **B19**(1-2), 172-80.

[12] Javey, A.; Guo, J.; Wang, Q.; Lundstrom, M.; Dai, H., *Nature* (2003), **424**(6949), 654-657.

[13] Krupke, R.; Hennrich, F.; Loehneysen, H. V.; Kappes, M. M., *Science* (2003), **301**(5631), 344-347.

[14] Kim, K.; Song, Y.; Hwang, C.; Chung, C.; Lee, J.; Choi, I.; Park, J., *J. Vac. Sci. Technol. B* (2004), **22**(3), 1331-1334.

[15] Zhang, Y. B.; Lau, S. P.; Huang, L.; Tanemura, M., *Appl. Phys. Lett.* (2005), **86**(12), 123115/1-123115/3.

[16] Gangloff, L.; Minoux, E.; Teo, K. B. K.; Vincent, P.; Semet, V. T.; Binh, V. T.; Yang, M. H.; Bu, I. Y. Y.; Lacerda, R. G.; Pirio, G.; Schnell, J. P.; Pribat, D.; Hasko, D. G.; Amaratunga, G. A. J.; Milne, W. I.; Legagneux, P., *Nano Lett.* (2004), **4**(9), 1575-1579.

[17] Jang, Y.; Choi, C.; Ju, B.; Ahn, J.; Lee, Y., *Thin Solid Films* (2003), **436**(2), 298-302.

[18] Kim, Y. C.; Sohn, K. H.; Cho, Y. M.; Yoo, E. H., *Appl. Phys. Lett.* (2004), **84**(26), 5350-5352.

[19] Manchado, M. A.; Lopez; Valentini, L.; Biagiotti, J.; Kenny, J. M., *Carbon* (2005), **43**(7), 1499-1505.

[20] Cantalini, C.; Valentini, L.; Armentano, I.; Kenny, J. M.; Lozzi, L.; Santucci, S., *J. European Ceram. Soc.* (2004), **24**(6), 1405-1408.

[21] Li, C.; Yu, Z.; Yao, K.; Ji, S.; Liang, J., *J. Mol. Catal. A-Chem.* (2005), **226**(1), 101-105.

[22] Xu, S.; Li, F.; Wei, R., *Carbon* (2005), **43**(4), 861-864.

[23] Rajalakshmi, N.; Ryu, Hojin; Shaijumon, M. M.; Ramaprabhu, S., *J. Power Sources* (2005), **140**(2), 250-257.

[24] Cai Y.; Cai Y.; Mou S.; Lu Y., *J. Chromatogr. A* (2005 Jul 22), **1081**(2), 245-7.

[25] Ye, Q.; Cassell, A. M.; Liu, H.; Chao, K.; Han, J.; Meyyappan, M., *Nano Lett.* (2004), **4**(7), 1301-1308.

[26] Shingaya, Y.; Nakayama, T.; Aono, M., *Physica B* (2002), **323**(1-4), 153-155.

[27] Dillon, A. C.; Jones, K. M.; Bekkedahl, T. A.; Kiang, C. H.; Bethune, D. S.; Heben, M. J., *Nature* (1997), **386**(6623), 377-379.

[28] Chambers, A.; Park, C.; Baker, R. Terry K.; Rodriguez, N. M., *J. Phys. Chem. B* (1998), **102**(22), 4253-4256.

[29] Hirscher, M.; Becher, M.; Haluska, M.; Von Zeppelin, F.; Chen, X.; Dettlaff-Weglikowska, U.; Roth, S., *J. Alloy. Compd.* (2003), **356-357**, 433-437.

[30] Otvos, Z.; Onyestyak, G.; Valyon, J.; Kiricsi, I.; Konya, Z.; Rees, L. V. C., *Appl. Surf. Sci.* (2004), **238**(1-4), 73-76.

[31] Kim, H.; Lee, Ho; Han, K.; Kim, J.; Song, M.; Park, M.; Lee, J.; Kang, J., *J. Phys. Chem. B* (2005), **109**(18), 8983-8986.

[32] Shionoya, S.; Yen, W. M., *Phosphor Handbook* (1999), 921 pp., CRC Press LLC, U.S.A..

[33] Seo, S. Y.; Lee, S.; Park, H. D.; Shin, N.; Sohn, K., *J. Appl. Phys.* (2002), **92**(9), 5248-5251.

[34] Hao, J.; Studenikin, S. A.; Cocivera, M., *J. Lumines.* (2001), **93**(4), 313-319.

[35] De Vicente, F. S.; De Castro, A. C.; De Souza, M. F.; Siu Li, M., *Thin Solid Films* (2002), **418**(2), 222-227.

[36] Judd, B. R., *Phys. Rev.* (1962), **127**, 750-61.

[37] Ofelt, G. S., *J. Chem. Phys.* (1962), **37**, 511-20.

[38] Gozzi, D.; Latini, A., patent pending *RM2004A000502* - October 13, 2004.

[39] Hou, Y.; Gao, S., *J. Mater. Chem.* (2003), **13**(7), 1510-1512.

[40] Kiang, C.; Goddard, W. A., *Phys. Rev. Lett.* (1996), **76**(14), 2515-18.

[41] Little, R. B., *J. Clust. Sci.* (2003), **14**(2), 135-185.

[42] Qian, W.; Liu, T.; Wang, Z.; Wei, F.; Li, Z.; Luo, G.; Li, Y., *Appl. Catal. A-Gen.* (2004), **260**(2), 223-228.

[43] Wang, H.; Baker, R. T. K., *J. Phys. Chem. B* (2004), **108**(52), 20273-20277.

[44] Takenaka, S.; Shigeta, Y.; Tanabe, E.; Otsuka, K., *J. Catal.* (2003), **220**(2), 468-477.

[45] Li, J.; Lu, G.; Li, K.; Wang, W., *J. Mol. Catal. A-Chem.* (2004), **221**(1-2), 105-112.

[46] Reshetenko, T. V.; Avdeeva, L. B.; Ushakov, V. A.; Moroz, E. M.; Shmakov, A. N.; Kriventsov, V. V.; Kochubey, D. I.; Pavlyukhin, Y. T.; Chuvilin, A. L.; Ismagilov, Z. R., *Appl. Catal. A-Gen.* (2004), **270**(1-2), 87-99.

[47] Seo, S. Y.; Sohn, K.; Park, H. D.; Lee, S., *J. Electrochem. Soc.* (2002), **149**(1), H12-H18.

[48] Kelly, K.L., *J. Opt. Soc. Am.* (1943), **33**, 627.

[49] Zhang, S.; Xiao, R., *J. Appl. Phys.* (1998), **83**(7), 3842-3848.

6. Acknowledgements

I wish to acknowledge the following people and institutes/organizations:

- Prof. Daniele Gozzi (University of Rome "La Sapienza"), for his patient supervision and direction of my work;

- The staff of Prof. Gozzi's Laboratory (RIMLab, Reactivity of Inorganic Materials Laboratory, Department of Chemistry, University of Rome "La Sapienza") , i.e., Dr. Pier Luigi Cignini, Dr. Francesco Di Pascasio, Dr. Massimiliano Iervolino and Dr. Alessandra Bellucci for their scientific and logistic support;

- Prof. Giuliano Moretti (University of Rome "La Sapienza"), an expert scientist in heterogeneous catalysis, for his precious suggestions;

- Prof. Massimo Tomellini (University of Rome "Tor Vergata"), for the development of the phenomenological and physical models for CNTs nucleation and growth;

- NIMS (National Institute for Materials Science, Japan), and particularly:

Dr. Masahiro Tosa and Dr. Hiroshi Suzuki (Materials Engineering Laboratory, Micro-Nano Component Materials Group) for the organization of HR-TEM measurements on CNT samples;

Prof. Jiancun Rao and Dr. Akira Hasegawa (NIMS High Voltage Microscopy Station) for performing HR-TEM measurements on CNT samples;

- The User Support Program for Nanotechnology with In-situ, High-resolution and Analytical Electron Microscopy conducted by Japan Ministry of Education, Culture, Sport, Science and Technology (MEXT) for the financial support to the HR-TEM measurements;

- JISTEC (Japan International Science and Technology Exchange Center) for the support given for my permanence in Japan through the REES (Research Experience for European Graduate Students in Science and Technology) Programme, and particularly Ms. Tomoko Inagaki for her kind assistance during all the period;

- Prof. Gustavo Capannelli and Mr. Claudio Uliana (University of Genova), for TEM measurements on CNT samples;

- Dr. Giancarlo Salviati and Dr. Nicola Armani (Italian National Research Council, Parma), for cathodoluminescence measurements on ceramic phosphor films;

- Dr. Daniela Ferro (Italian National Research Council, Rome) and Dr. Giuseppe Caruso (University of Rome "La Sapienza"), for SEM and EDS measurements;

- Prof. Anna Corrias (University of Cagliari), for HR-TEM measurements on ceramic phosphor films;

- Dr. Stella Nunziante Cesaro (Italian National Research Council, Rome) for IR measurements on phosphor host oxides;

- Prof. Marcello Colapietro (University of Rome “La Sapienza”) for the interpretation of electron diffraction patterns;
- Dr. Silvano Del Gobbo, Ms. Piera Moro and Ms. Lucia Carassiti for their collaboration in the experimental work;
- Dr. Giovanni Ferraris (Italian National Research Council, Rome), for BET measurements on catalyst samples;
- Mr. Giuliano Gervasoni (University of Rome “La Sapienza”) for his precious assistance in the realization of many experimental setups;
- Mr. Silvano Ghighi (University of Rome “La Sapienza”) for ICP analyses;
- Dr. Paola Galli (University of Rome “La Sapienza”) for combustion analyses.

This thesis is dedicated to the memory of my Grandmother, Rosa.